PHASE SEPARATION IN TWO-PHASE MICROFLUIDIC HEAT EXCHANGERS

A DISSERTATION
SUBMITTED TO THE DEPARTMENT OF MECHANICAL ENGINEERING
AND THE COMMITTEE ON GRADUATE STUDIES
OF STANFORD UNIVERSITY
IN PARTIAL FULFILLMENT OF THE REQUIREMENTS
FOR THE DEGREE OF
DOCTOR OF PHILOSOPHY

Milnes P. David
March 2011

© 2011 by Milnes Paul David. All Rights Reserved.

Re-distributed by Stanford University under license with the author.

This work is licensed under a Creative Commons Attribution-Noncommercial 3.0 United States License.
http://creativecommons.org/licenses/by-nc/3.0/us/

This dissertation is online at: http://purl.stanford.edu/ns144db9649

I certify that I have read this dissertation and that, in my opinion, it is fully adequate in scope and quality as a dissertation for the degree of Doctor of Philosophy.

Kenneth Goodson, Primary Adviser

I certify that I have read this dissertation and that, in my opinion, it is fully adequate in scope and quality as a dissertation for the degree of Doctor of Philosophy.

Juan Santiago

I certify that I have read this dissertation and that, in my opinion, it is fully adequate in scope and quality as a dissertation for the degree of Doctor of Philosophy.

Maxat Touzelbaev

Approved for the Stanford University Committee on Graduate Studies.

Patricia J. Gumport, Vice Provost Graduate Education

This signature page was generated electronically upon submission of this dissertation in electronic format. An original signed hard copy of the signature page is on file in University Archives.

ABSTRACT

Two-phase microfluidic heat exchangers have the potential to meet the large heat dissipation demands of high power electronics and computing systems. Two-phase cooling systems face practical challenges brought on by the growth and advection of the vapor phase in the confined geometries, which lead to large pressure drops, increased thermal resistance and the formation of detrimental flow instabilities. One proposed solution to these issues is phase separation, whereby the vapor is locally separated from the two-phase flow through a porous hydrophobic membrane.

This dissertation describes a series of studies conducted to develop an understanding of the factors that influence vapor separation and its impact on the hydraulic and thermal characteristics of two-phase heat exchangers. Flow phenomena are a critical component in developing this understanding of phase separation. High speed visualization of adiabatic and diabatic vaporizing flows was carried out in a single 124μm by 98μm copper microchannel with a 65μm thick, 220nm pore diameter hydrophobic PTFE membrane wall. During adiabatic air-water flow, wavy-stratified and stratified flow dominated lower liquid velocities, while plug and annular type flows dominated at the higher velocities. Analysis found that air removal could be improved by increasing the venting area, increasing the trans-membrane pressure or using thinner, high permeability membranes. Diabatic water-vapor experiments with mass flux velocities of 140 and 340 kg/s-m^2 and exit qualities up to 20% found that stratified type flows dominate at lower mass fluxes while cyclical churn-annular flow became more prevalent at the higher mass-flux and quality. The observed flow regimes are hypothesized to play a significant role in determining the pressure drop and heat transfer coefficient during flow boiling.

To study the impact of various geometric and membrane factors on the performance of a phase separating microchannel heat exchanger dissipating 100W of heat, a numerical model incorporating vapor separation and transport during two-phase flow boiling in a microchannel was developed. The impact of substrate thermal conductivity and thickness, membrane permeability and thickness, liquid channel density, liquid and vent channel diameter and vent-to-liquid channel diameter ratio was studied and compared for a standard non-venting heat exchanger, a vapor venting heat exchanger and a non-venting heat exchanger occupying the same increased volume as the venting heat exchanger. The numerical study found that the venting heat exchanger had improved pressure drop and device temperatures for all tested conditions when compared against a standard heat exchanger but only under very limited conditions when compared against the volumetrically equivalent non-venting heat exchanger. The study indicates that the best venting heat exchanger performance is achieved when the membrane conductance is of the same order or higher than that of the microchannel; this can be achieved through the use of thin high permeability membranes coupled with small hydraulic diameter microchannels.

Finally, a study was conducted to explore the fabrication methods to build a vapor separating heat exchanger and to quantify the operating performance of multichannel silicon and copper phase separating devices. A copper parallel microchannel heat exchanger with nineteen 130μm square microchannels was built and tested at heat fluxes of up to 820 kW/m^2 and water mass fluxes of between 102 and 420 kg/s-m^2. Normalized pressure drop was improved by as much as 60% and average substrate temperature by a maximum of 4.4°C between the non-venting control and vapor venting device under similar operating conditions. Comparison between the experimental results and simulation predictions found higher than expected pressure drop improvements at higher mass fluxes and poorer heat transfer coefficients at the lowest mass flux. Based on the flow phenomena study these discrepancies are believed to be due to the mass flux and vapor quality dependent two-phase flow structures.

The encouraging experimental and numerical results motivate further study into phase separation methods, materials and flow physics. The development of a high performance phase separating heat exchanger, with the thermal benefits of two-phase boiling flow and the hydraulic benefits of single-phase liquid flow, would strongly enable the adoption and application of two-phase heat exchangers to provide effective and efficient cooling for next generation high power computing systems.

To my parents
with love

ACKNOWLEDGEMENTS

I'm very grateful to have had the opportunity to pursue my graduate studies at Stanford and to have spent my time in the company of many wonderful people. First and foremost, I thank my parents, whose countless sacrifices and unwavering love, support, strength and prayers have meant everything to me. Though I doubt I will ever fully understand how they provided me with opportunity upon opportunity such that I now have the distinct honor of being able to present this dissertation, I can say with all my heart "Thanks for everything mama and dada. I love you both very much."

I'm also grateful for having had the opportunity to study under Prof. Ken Goodson and for being a part of his lab for almost six years. Prof. Goodson has been a great advisor and I thank him for encouraging me to pursue a doctorate and for helping me overcome many obstacles and become a better engineer and scientist. I also thank Prof. Juan Santiago for giving me the first taste of research when I started out in his lab in the fall of 2004, and for always being ready to discuss any research problem I had. Thanks to Dr. Maxat Touzelbaev for his advice, for his help with my research and for providing me with tools that greatly enhanced my work. Thanks also to Prof. Tom Kenny with whom I interviewed when considering Stanford for graduate school. His recommendations helped me obtain the Stanford Graduate Fellowship which meant an enormous deal, both as an honor and as a means to enable me to pursue the doctoral path. Prof. Mehdi Asheghi has been an amazing resource during my last few years at Stanford and I really appreciate his encouragement, experience and technical advice and for helping me find my first job.

One the biggest advantage of being in a lab at Stanford is all the wonderful and brilliant people you get to work with. I'd like to give special thanks to Julie Steinbrenner and Josef Miler whose friendship, help and advice were invaluable in my work and my time at Stanford. I would also like to thank my lab-mates and friends Amy Marconnet, Saniya Leblanc, Anita Rogacs, John Reifenberg, Roger Flynn, Fumin Wang, Chen Fang, Tricia Gharagozloo, Matt Panzer, Jeremy Rowlette, Shilpi Roy, Betai Koffi and Lewis Hom from the Goodson Lab, Andrew Graham and Kuan-

Lin Chen from the Kenny Lab, Tarun Khurana, Cullen Buie, Moran Bercovici, Alexander Persat, Dan Strickland and Elia Junco from the Santiago Lab, and Vikram Mukundan and Alvin Barlian from the Pruitt Lab. Thanks to Lakhbir Johal at the Thermosciences Machine Shop for fabricating many of the samples used in my work and thanks also to Dr. Sung-Ki Kim and his family, Dr. Chiriac, Dr. Iyengar and Dr. Chu for their help and friendship.

I also want to thank Stanford University and William R. and Sara Hart Kimball for the Stanford Graduate Fellowship that funded my study for the first three years at Stanford. I also acknowledge the support of the MARCO Interconnect Focus Center, one of five research centers funded under the Focus Center Research Program, a Semiconductor Research Corporation (SRC) program. Thanks also to Intel and AMD for both their financial and technical support during various stages of my study.

Thanks to everyone from the Church in Palo Alto and Stanford Christian Students who provided me with exceptional support, friendship and fellowship. I'd like to thank George and Luna Dai who took me under their wing as soon as I arrived and made sure I was always welcome in their home. I'd also like to thank Benjamin and Elaine Dai, Jeff and Phoebe Chang, Brian and Jean Chan, John and Alice Chang and Benjamin Lee for all their help and friendship over the years. Thanks also to David White, James Lin, Thomas Lo, Bill Bathurst, Henry and Karen Yang, Paul and Conwen Lee, San Wong, Ivan Wong, Boaz Chai, Joshua Lin, Bonnie Chan, Michelle and James Kao, Camilo Ordonez, Alex Chen, Alex Shaw, Manuel Manzanares, Ben Olson, Ty Chau, Stanley Yip and family, Samuel Hsiung, Flora Yang, Peggy Chung, Grace Ho and Ming Yi.

My faith has played a role that can't adequately be put into words but I'm thankful beyond expression for my Lord Jesus Christ and what He means to me and for helping me realize that my life and my heart will always be hidden in Him.

"For I am persuaded that neither death nor life nor angels nor principalities nor things present nor things to come nor powers nor height nor depth nor any other creature will be able to separate us from the love of God, which is in Christ Jesus our Lord."

Romans 8:38-39

TABLE OF CONTENTS

ABSTRACT IV

ACKNOWLEDGEMENTS VII

LIST OF FIGURES XI

LIST OF TABLES XX

CHAPTER 1 - INTRODUCTION 1

1.1 Motivation and Overview of Current Strategies 1

1.2 Two-Phase Cooling 3

1.3 Gas-Liquid Phase Separation 5

1.3.1 Description of the Proposed Solution 5
1.3.2 Phase Separation at the Macroscale 6
1.3.3 Phase Separation at the Microscale 7

1.4 Objectives and Approaches 10

CHAPTER 2 - ADIABATIC AND DIABATIC TWO-PHASE VENTING FLOW PHENOMENA IN A MICROCHANNEL 13

2.2 Experimental Method 14

2.2.1 Device design and fabrication 14
2.2.2 Experimental Setup 16

2.3 Results and Discussion 19

2.3.1 Adiabatic Air-Water Flow 19
2.3.1.1 Visualization of Flow-Regime 19
2.3.1.2 Air-Venting Analysis 24
2.3.2 Diabatic Vapor-Liquid Flow 30
2.3.2.1 Visualization of Flow-Regime 30
2.3.2.2 Impact of flow-regime on pressure drop and heat transfer 35

2.4 Summary and Conclusion 36

CHAPTER 3 - MODELING AND PARAMETRIC ANALYSIS OF TWO-PHASE VAPOR VENTING FLOW IN HEAT EXCHANGERS 38

3.1 Motivation and Overview 38

3.2 Description of the Computational Domain and Solution Techniques 39

3.3 Pressure Drop Models 42

3.4 Convective Heat Transfer Models 47

3.5 Description of the Simulated Heat Sink 50

3.6 Simulation Results and Discussion 52

3.6.1 Impact of Substrate Spreading during Single Phase Flow 52
3.6.2 Impact of Substrate Spreading during Two-Phase Flow 55
3.6.3 Impact of Membrane Conductance 57
3.6.4 Impact of Channel Density 61

3.6.5 Impact of Channel Hydraulic Diameter 64
3.6.6 Impact of Liquid-Vent Channel Diameter Ratio 66
3.7 Limitations of the Current Approach and Future Developments 69
3.8 Summary of Findings and Conclusions 70
CHAPTER 4 - DESIGN, FABRICATION AND EXPERIMENTAL CHARACTERIZATION OF AIR AND VAPOR VENTING MULTICHANNEL DEVICES 73
4.1 Motivation and Overview 73
4.2 Design of the Vapor Separating Microchannel Devices 74
4.2.1 Venting Membrane 74
4.2.2 Silicon Heat Exchanger 75
4.2.3 Copper Heat Exchanger 77
4.3 Experimental Method 80
4.3.1 Silicon: Adiabatic Experimental Setup and Procedure 80
4.3.2 Copper: Diabatic Experimental Setup and Procedure 82
4.3.3 Data Reduction and Error Analysis 83
4.3.3.1 Input and Effective Heating Power 83
4.3.3.2 Pressure Drop 84
4.3.3.3 Temperature, Heat Transfer Coefficient and Thermal Resistance 85
4.3.3.4 Flow Rate and Velocity 86
4.3.3.5 Summary of Uncertainties 87
4.4 Modeling 87
4.5 Results and Discussion 88
4.5.1 Hydraulic Characteristics 88
4.5.1.1 Steady State Pressure Drop 88
4.5.1.2 Impact of trans-membrane pressure on pressure drop improvement ... 91
4.5.1.3. Single channel and Static Ledinegg instability 93
4.5.2 Thermal Characteristics 96
4.5.2.1 Temperature 96
4.5.2.2 Heat Transfer Coefficient 98
4.5.2.3 Thermal Resistance 101
4.5.3 Adiabatic and Diabatic Venting Characteristics 102
4.5.3.1 Adiabatic Venting of Air from Silicon Device 102
4.5.3.2 Diabatic Venting of Vapor from Copper Device 103
4.5.4 Condensation and Membrane Wear/Fouling 106
4.5.4.1 Condensation 106
4.5.4.1 Membrane Wear and Fouling 108
4.6 Summary of Findings and Conclusion 110
CHAPTER 5 - CONCLUSION 113
5.1 Summary of Results and Contributions to the Field 113
5.2 Challenges and Directions for Future Work 116
5.3 Concluding Remarks 119
REFERENCES 121

LIST OF FIGURES

Figure 1.1 ITRS Roadmap showing A) the rise in power dissipation and reduction of junction temperature and B) the reduction in thermal resistance for high performance and cost performance IC's.. 2

Figure 1.2 Schematic of a vapor venting heat exchanger showing the three main components: the two-phase microchannels, the vapor vent channels and the porous hydrophobic membrane. The membrane separates the vapor phase from the two-phase mixture and transports it to the vent channel. 6

Figure 1.3 Schematic view of the A) rotating phase separator described in Ref. [39] to separate out the liquid from a liquid droplet dispersed two-phase flow using centrifugal forces and B) T-junction based flow separator as described in Ref. [40] where a series of oriented junctions can be used to separate out the phases.. 8

Figure 2.1 Cross-sectional side and top views of the copper microchannel device (figures are not to scale). 15

Figure 2.2 Experimental setup showing key equipment and close up of channel. T represents a thermocouple, P, a pressure sensor and Q, a flow meter. Liquid is pumped using the peristaltic pump and air is delivered by the syringe pump. The vent side of the channel is left open to the atmosphere. Non-vented air flow rate in the outlet tubing is measured using the pair of IR slot sensors that measure air slug velocities and residence times. 17

Figure 2.3 Sequence of images showing an example of bubbly air venting at a liquid velocity of 0.36m/s and an air injection velocity of 0.32m/s. As air is injected into the liquid stream, small bubbles break off the injection port (0ms) and attach to the membrane (0.15ms) through which the air can now escape causing the bubble to collapse (0.15ms-0.6ms) until it eventually disappears (0.75ms). As air flow rate is increased the bubbles get larger and move along the membrane surface once attached. 19

Figure 2.4 Examples of steady state flow structures that were observed at different air and water velocities. A) Wavy flow, B) Stratified flow, C) Corner-wedge flow, where the flow structure forms on the plastic-copper corner, D) Slug-annular flow and E) Annular flow. The latter two flow regimes are observed at the highest tested Weber number of 0.6. 20

Figure 2.5 Superficial velocity flow regime map for adiabatic air-water two-phase flow in a microchannel with one porous hydrophobic wall. 21

Figure 2.6 Air venting rate vs. pressure as measured at the air injection port. The type of flow-regime experienced influences the rate of air removal through the membrane. At the two lower Weber number flows, most of the air injected is removed but this is not the case at the higher Weber number flow, where differing flow regimes and partial venting result in higher pressure drops...... 25

Figure 2.7 Air venting rate per unit injection point pressure (venting effectiveness) vs. Mass quality. The poor effectiveness of the highest Weber number flow is clearly seen with a roll-off of around $2x10^{-12}$ kg/s-Pa as compared to $6x10^{-12}$ kg/s-Pa for the lower Weber number flows. High Weber number flows can result in less desirable corner-wedge (#1) and annular type flows that delay venting and reduce the maximum venting effectiveness................................. 25

Figure 2.8 Normalized venting area vs. Mass quality. Contact area between air and membrane increases linearly with quality until all area has been utilized. At this point, the venting effectiveness is maximized and further venting occurs only if pressure is increased. At increased trans-membrane pressures (*), upstream venting rate increases, freeing more space for venting.................... 26

Figure 2.9 The venting rate per unit area per unit pressure (permeance) generally matches the theoretically calculated value of $4.1x10^{-6} \pm 1.1x10^{-6}$ m/s-Pa (– · – and – – respectively). The theoretical value is determined from the membrane thickness and intrinsic permeability measurements [67]................................ 28

Figure 2.10 Examples of the dominant flow regimes observed during diabatic operation with the black arrow indicating direction of liquid flow. A) Bubbly flow is typically observed at very low mass qualities <1%. B) Slug type flows are also only observed at low qualities and have a distinctive asymmetric shape due to the hydrophobicity of the membrane. C) Stratified flows are dominant at intermediate qualities up to 10% with cyclical wetting-stratified-dryout behavior observed at G = 140 kg/s-m^2 and qualities > 4%. D) At the higher mass flux of 340 kg/s-m^2 and at low qualities larger bubbles are observed forming on the membrane, then coalescing to form stratified and slug flows. 31

Figure 2.11 Sequence of images at various times during cyclical churn-annular flow that is observed only at the higher mass flux of 340 kg/s-m^2 and at qualities > 10%. Schematics are drawn directly from the images and are included for clarity. Initial wetting by liquid rivulets occurs on the various surfaces (A) followed by several churning annular slugs (B). These churning annular structures appear to breakup on the membrane surface leaving behind large droplets (C) most of which coalesce and are pushed out leaving behind smaller drops during the dry-out phase when the thin liquid films on the wetting surfaces evaporate (D). The entire cycle then repeats and found to vary from 0.02s to 0.1s (f ~ 10 to 50 Hz).. 33

Figure 2.12 Diabatic flow regime map with mass flux plotted against the quality for the vapor separation microchannel at the two tested mass fluxes. At G = 140 kg/s-m^2 stratified and then cyclical stratified flows are observed and at G = 340 kg/s-m^2, stratified type flows give way to a cyclical mixed stratified and churning-annular type flow which then leads to cyclical churn-annular type flows at higher qualities. In general the flows at the higher mass flux were more chaotic. 34

Figure 2.13 Flow map and transition criteria as proposed by Harirchian and Garimella [74]. The y-axis is the product of the Boiling number (Boi) and the Reynold's number (Re) and the x-axis the product of the square root of the Bond number (Bo) and Re. Harirchian and Garimella's reported flow regimes is included (*) for comparison. The curve indicates when slug type flows become churn/annular in nature. The transition criteria developed predicts the churn type flows seen in our device, but the predicted slug type flows are manifested as stratified flow in our device due to the hydrophobicity of the membrane... 35

Figure 3.1 Schematic of computational element used in simulations presented in this study. External boundary conditions are presented. Region A: 1D two-phase flow in the microchannels with heat flux provided by solution of Region C. Also considers single-phase flow in the membrane based on pressure profile in liquid and vent channels, the latter obtained from the solution to Region B. Region B: 1D single-phase vapor flow in vent channel with vapor injection provided from solution to Region A. Region C: 2D solid conduction in substrate with convective boundary condition on top surface provided by solution of Region A. 39

Figure 3.2 Comparison of experimental liquid-only (lo) normalized two-phase pressure drop versus vapor quality data against four available correlations: Lockhart and Martinelli (LM) separated flow correlation with C = 5, homogenous equilibrium model (HEM), separated flow correlation by Mishima and Hibiki [86], separated flow correlation by HJ Lee *et al.* [83]. Exp. data falls mostly between LM and HEM models but agrees better in trend with the correlation by HJ Lee *et al.* Correlation developed in this study is given by Eq. (3.12)... 46

Figure 3.3 Comparison of experimental data against two widely used heat transfer coefficient correlations proposed by Kandlikar and Balasubramanian [89] and Lee and Mudawar [90]. Data at all flow-rates was found to be well correlated by Eq. (3.17)... 50

Figure 3.4 Schematics of the three different types of device configurations that were simulated. The NVEV device is designed to occupy the same total volume as the venting device with a comparatively larger liquid channel while the non-venting device has the same liquid channel hydraulic diameter as the venting device. 51

Figure 3.5 Simulated input power normalized channel wall heat flux (top left), pressure drop (top right), fluid temperature (bottom left) and mean substrate temperature (bottom right) along the length of a 1cm long, 100μm x 100μm channel, dissipating 50 W/cm^2 heat flux, and experiencing single phase liquid flow. Several substrate thickness and conductivities were simulated, combined as R_{th}, the axial thermal resistance. The highest R_{th}, indicative of low thermal conductivity thin substrates, leads to a constant wall heat flux like boundary condition while low R_{th} leads to constant wall temperature like boundary condition. Pressure drop reduces with R_{th} due to increased fluid preheating. Simulations were carried out using conjugate conduction-convection finite difference model with laminar friction factor pressure drop and developing Nusselt number relations for the heat transfer. 54

Figure 3.6 Mean device temperature as a function of the Biot number, where Bi = $h*d_{sub}/k_{sub}$. For low Biot numbers the device temperature is sensitive to the fluid temperature and at high Biot numbers to the transverse thermal resistance, d_{sub}/k_{sub}. 55

Figure 3.7 Spatial pressure profile and total pressure drop for varying values of axial thermal resistance during two-phase flow in the non-venting (NV), venting (V) and non-venting equivalent volume (NVEV) device. In the NVEV device the liquid channel occupies the same volume as the liquid channel, membrane and vent channel does in the venting device. Spreading only slightly alters the pressure profile and total pressure drop in the device. 56

Figure 3.8 Spatial substrate temperature and mean device temperature for varying degrees of axial thermal resistance in the non-venting (NV), venting (V) and non-venting equivalent volume (NVEV) device. In the NVEV device the liquid channel occupies the same volume as the liquid channel, membrane and vent channel does in the venting device. A high thermal resistance increases the temperature magnitude and increases spatial variations due to reduced spreading. 56

Figure 3.9 Vapor venting profile along the length of the venting device. Abrupt increase occurs when flow in the liquid channel transitions from single to two-phase, where the vapor formed can flow through the membrane. Spreading results in a shift upstream of the single to two-phase transition point resulting in earlier venting. 57

Figure 3.10 Impact of membrane thickness and intrinsic permeability on the total pressure drop, device temperature and heat transfer coefficient in the non-venting, venting and non-venting equivalent volume (NVEV) devices. In the

NVEV device the liquid channel occupies the same volume as the liquid channel, membrane and vent channel does in the venting device. Reducing membrane thickness and/or increasing permeability can significantly improve the performance of the venting device, potentially beyond that achievable in a NVEV device.. 58

Figure 3.11 Increasing membrane conductance leads to a clear reduction in pressure drop and device temperature as the vapor fraction removed through the membrane increases. The vapor removal and device performance is maximized at a conductance of 1e-14 m^3.. 60

Figure 3.12 Vapor removal fraction as a function of the conductance ratio. When the conductance of the membrane is increased to the same order as that of the channel, all the vapor produced is vented, leading to very low pressure drop and device temperatures. 61

Figure 3.13 Pressure drop, mean device temperature and heat transfer coefficient in the non-venting device, the venting device and the non-venting equivalent volume (NVEV) device as the fin-to-channel width is increased while maintaining the same total liquid flow-rate and heat flux. In the non-venting and venting devices the liquid channel is 100μm square while in the NVEV the liquid channel consumes the volume occupied by the membrane and the vent channel in the venting device and is 100μm x 265μm. Higher fin-to-channel width ratios lead to fewer channels and higher mass fluxes through each channel, increasing the pressure drop and device temperatures. Increased pressure also delays boiling and reduces the mean heat transfer coefficient. .. 62

Figure 3.14 Impact of fin-to-channel width ratio on the fin efficiency in the non-venting, venting and non-venting equivalent volume devices. As the fins are widened, the fin efficiency improves, though the advantage gained is small after a fin-to-channel width ratio of about 1 when using copper as the substrate.. 63

Figure 3.15 Venting percentage and spatial profile of mass flux vented as the fin-to-channel ratio is varied. The amount of vapor vented initially increases due to the larger pressure on the liquid side as the channel density reduces. 64

Figure 3.16 Pressure drop and heat transfer coefficient reduce monotonically as the channel diameters are increased in the non-venting, venting and non-venting equivalent volume (NVEV) devices. In the NVEV device the liquid channel occupies the same volume as the liquid channel, membrane and vent channel does in the venting device. Device temperatures rise after an initial drop due to the lowered heat transfer coefficient playing a greater role compared to the reducing saturation temperatures. The venting device performs better than the standard non-venting device but is outperformed by the non-venting equivalent volume device. 65

Figure 3.17 Vented vapor fraction (left) reduces as the channel diameters are increased due to the reduced trans-membrane driving pressure (right). These results imply the use of smaller channels to increase venting, but this results in higher pressure and temperature magnitudes when using the current membranes. 66

Figure 3.18 Pressure drop, mean device temperature and heat transfer coefficient as the liquid-to-vent channel ratio is varied in the non-venting, venting and non-venting equivalent volume (NVEV) devices at two different liquid side channel diameters, 50µm and 100µm. In the NVEV device the liquid channel occupies the same volume as the liquid channel, membrane and vent channel does in the venting device. As the vapor-to-liquid channel ratio is increased, the pressure drop, device temperatures and heat transfer coefficients improve in the venting device as compared to the non-venting device. However, the NVEV device again shows the lowest pressure drop and device temperatures despite having lower heat transfer coefficients. 67

Figure 3.19 Increase in the channel ratio leads to a smaller vent side pressure (right) and thus a larger fraction of the vapor venting (left). This behavior is more significant when using smaller channels where the magnitude of the pressures is larger. 68

Figure 4.1 Processing steps in fabrication of a silicon vapor venting heat exchanger. 76

Figure 4.2 Channel side of the silicon microchannel heat exchanger. The thermal isolation trenches were added to reduce heat loss from the heated channel region to the manifolds during diabatic experiments. 77

Figure 4.3 Design and assembly of the copper microchannel heat exchanger used in this work. Screws and edges of device are coated with high temperature RTV to provide sealing. The channel region is 19mm long and 5.5mm wide with nineteen 130µm x 134µm microchannels. 78

Figure 4.4 Top view of tested microchannel device showing the manifold, microchannels, thermocouple measurement points and the relative position of the AMD heater chip with strip heaters. The twelve thermocouples are embedded 1.2mm below the top of the channel walls and the heat applied approximately 2.4mm below the top surface. Only the middle two heaters on the test chip are used to generate heat flux. 79

Figure 4.5 Schematics of the three different types of copper devices that were assembled and tested in this work. The PTFE membrane is 65µm thick and the silicone film is 400µm thick. 80

Figure 4.6 Experimental setup to study adiabatic vapor-venting and hydraulic stability of the vapor venting silicon device. IR slot sensors are used to measure void fraction and interface velocities from which inlet, outlet and vented air mass can be determined. 81

Figure 4.7 Experimental setup to study diabatic vapor venting from a copper microchannel heat exchanger. 'P' represents pressure sensors and 'T' thermocouples. Heat flux is generated by an AMD test chip and control platform. Vapor vent rate is calculated by measuring the mass defect using the electronic scale. Vacuum on vent side generated by syringe and mass. For control and non-venting membrane devices the vent side apparatus is not used.. 83

Figure 4.8 Comparison of experimental liquid-only (lo) normalized total pressure drop versus input heat flux for the non-venting control device, non-venting membrane device (NVMD) and venting device shows average improvement ~60% between the control and venting devices. Non-venting membrane devices behave similar to control at mass flux of 102 kg/s-m^2 (A), but deviate at higher mass flux of 420 kg/s-m^2 (B) due to the impact of both hydrophobic membrane and mass flux on the flow regime. Numerical results compare well at 102 kg/s-m^2 but underestimates improvement as mass fluxes increase due to formation of complex churn-annular and droplet type flows. 89

Figure 4.9 Simulation and data for the normalized pressure drop as the pressure ratio is increased. Increasing the trans-membrane pressure by reducing the vacuum pressure results in increased venting and improved device pressure drop. When no vacuum is applied, the vapor self-vents due to the pressure in the liquid-side channel, and the improvement in the pressure drop is ~30%. 92

Figure 4.10 Experimental data of the power efficiency vs. the normalized trans-membrane ratio. Increasing the trans-membrane pressure by reducing the vacuum pressure, increases venting and results in smaller liquid side pressures. This reduces the required pumping power on the liquid side. As the vacuum level is increased beyond a certain extent however, the energy savings on the liquid side is offset by the pump power required on the vent side to maintain the given vacuum level resulting in a reduction in the efficiency. 93

Figure 4.11 Pressure and velocity changes during adiabatic air venting in the silicon venting microchannel device. As an air slug encounters the venting membrane, it begins to vent, causing the system pressure to drop and the flow to accelerate. For this particular experiment the correlation was found to be –0.7.

This type of instability is not expected to be significant in two-phase diabatic microchannel devices operating at typical flow-rates and heat fluxes where stratified flows are expected to be dominant. 94

Figure 4.12 Simulated demand curves of pressure drop vs. mass flux for the non-venting and vapor venting devices discussed in this study and based on the model discussed in Chapter 3. Comparison with an example pump supply curve shows that the negative slope -δ(ΔP)/δG for the non-venting devices is greater than that for the pump resulting in static Ledinegg instability. However, the negative slope is smaller for the venting devices making it more stable. .. 96

Figure 4.13 Average device temperatures in the control, non-venting membrane (NVMD) and venting devices at two of the four mass fluxes tested. Improvements in device temperatures in the venting devices are found to be mostly due to the improvement in saturation temperatures. Non-venting membrane devices had higher device temperatures than the control due to slightly higher saturation temperature and poorer heat transfer coefficient..... 97

Figure 4.14 Device temperatures improve almost linearly with increasing trans-membrane pressures as saturation temperature reduces. 98

Figure 4.15 Two-phase heat transfer coefficients in the control, non-venting membrane and venting devices at the four tested mass fluxes. The heat transfer coefficients in the venting device are found to be equivalent or slightly higher for the three higher mass fluxes but lower for the lowest mass flux. This is believed to be due to changes in flow regime between the control and venting devices. Improvements in the heat transfer coefficient in the venting device due to lower quality flows is also potentially being offset by the negative impact of reducing saturation pressures. 99

Figure 4.16 Thermal resistance of the three different types of heat exchangers at flow-rates of 2ml/min and 8ml/min. Given the high input powers, there is little difference in the thermal resistance between the devices. The two-phase and single phase regions are well described by Eqs. (4.14) and (4.15) respectively….. 101

Figure 4.17 Experimental and numerical results of venting rates at two of the four tested mass fluxes. Venting rates increase as more vapor is being generated and because of the rising pressure on the liquid side of the device. 104

Figure 4.18 Venting rates and venting fractions increase as the trans-membrane pressure increases. The increased vapor removal leads to improved pressure drops and device temperatures. 104

Figure 4.19 View of the top surface of the PTFE membrane during diabatic operation of the silicon heat exchanger shows the impact of condensation and evaporation. A) As the fluid is being heated, some of the liquid evaporates and condenses within and on the surface of the membrane, creating dark 'splotches.' B) As the heating is increased the amount of evaporation and condensation also increases resulting in the formation of large drops on the surface of the membrane. C) Once phase change occurs in the channels below the venting vapor pushes out the condensed fluid and clears the membrane as evidenced by the white open regions. The membrane is also sufficiently hot that further condensation is reduced. 107

Figure 4.20 SEM of the 220nm PTFE membrane before and after 30+ hours of cyclical use in the copper vapor venting device. A) SEM of unused membrane. B) SEM of membrane from venting region of the copper device after use. Comparison with (A) shows little wear or fouling on the membrane surface. C) SEM of membrane from non-venting region sandwiched between copper substrate and cap show that compression combined with thermal cycling results in a significant loss of porosity. The membrane also turned translucent in this region. 109

Figure 5.1 Schematic of a silicon device with an in-situ porous structure (center) that vents the vapor formed in the liquid channel on the right to the vent channel on the left. 117

LIST OF TABLES

Table 3.1 List of default test conditions 52

Table 4.1 Summary of experimental uncertainties 87

Table 4.2 Adiabatic air venting efficiency from an air-water mixture flowing in the silicon microchannel device 103

CHAPTER 1 INTRODUCTION

1.1 Motivation and Overview of Current Strategies

Effective thermal management is essential for the development of next generation computational systems. As shown in Figure 1.1, the International Technology Roadmap for Semiconductors (ITRS) predicts total power dissipation requirements of over 200W for high performance packages, junction temperatures less than 90°C and thermal resistances less than 0.1°C/W [1] over the next decade. However, these specifications don't capture the additional constraints that are imposed and the complexities in providing the required cooling while addressing reliability, compactness, noise, power consumption and cost of the thermal solution. One example of this complexity is seen in 3D Integrated Circuits, where logic, communication, storage and other functional IC's are combined in a single stacked structure with the heat generating component deep within the stack. This requires that the cooling solution be incorporated as a compatible element within the die stack itself and meet material, fabrication and footprint constraints that traditional planar microprocessor cooling solutions do not necessarily face [2,3]. The explosion of mobile computing devices is also pushing the boundaries of compact, highly reliable, and passive cooling solutions. The greatest need and urgency for high performance efficient cooling solutions however lie in the domain of data centers, servers and supercomputers. As reported by researchers at IBM [4], data centers accounted for almost 1.2% (5 GW) of the US energy consumption in 2007, of which almost 30%-40% (~2GW) was consumed by the cooling solutions alone. 'Green' data centers and energy efficient cooling solutions are thus of significant interest at the academic, corporate and federal level.

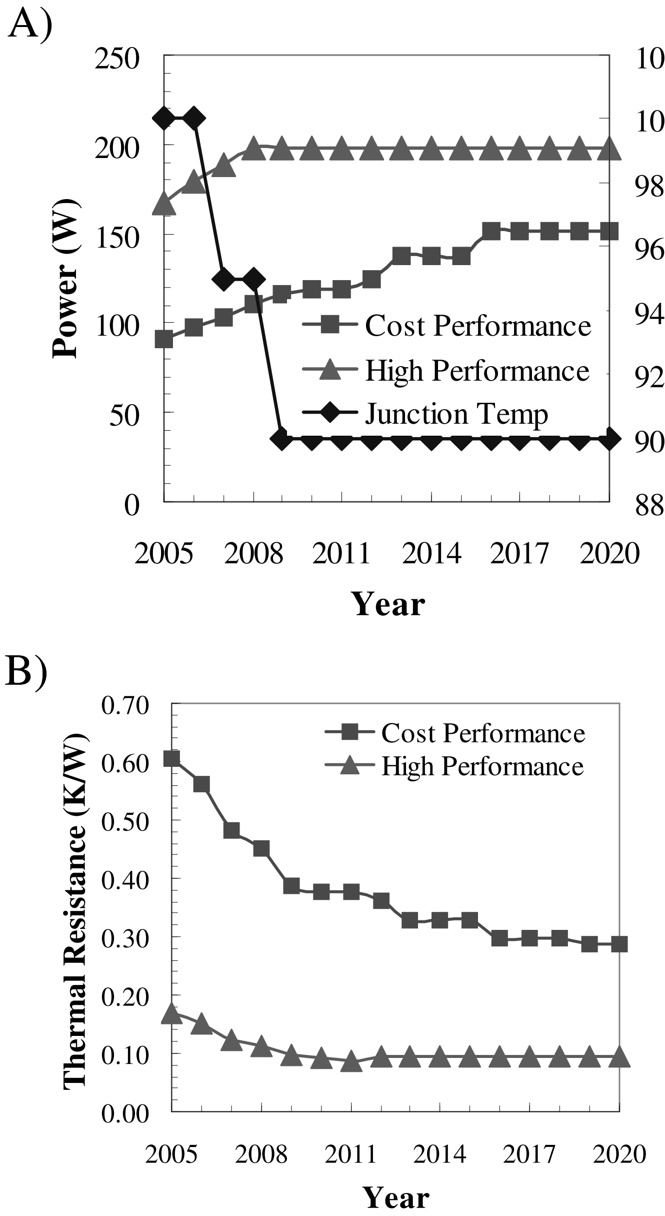

Figure 1.1 ITRS Roadmap showing A) the rise in power dissipation and reduction of junction temperature and B) the reduction in thermal resistance for high performance and cost performance IC's.

Cooling technologies such as fans (R_{th} ~ 10-100 K/W) and heat pipes (R_{th} ~ 1-10 K/W) [5] are reaching the limit of their cooling capacity while meeting the variety of performance, geometrical and cost constraints. To meet the current cooling demands, strategies such as thermoelectric cooling [6-8] , micro refrigeration [9-11], micro-jet [12-15] and microchannel liquid cooling have been investigated and reported in the literature. Liquid cooling using microfabricated structures is promising owing to small dimensions and very high thermal conductances as demonstrated by Tuckerman and Pease's seminal work using forced liquid convection in silicon microchannels to dissipate 790 W/cm^2 and obtain a thermal resistance of less than 0.1 ºC/W [16]. Though single-phase forced convection liquid cooling has seen only limited use in consumer electronics, such as the Apple G5, liquid cooling has seen extensive use in data centers [17], where the disadvantage of higher initial cost and extensive liquid plumbing are offset by the improved cooling and energy savings due to the reduced need for data center air-conditioning. The heated liquid can also more efficiently be utilized, such as to provide building heat and in adsorption chillers.

However, single-phase liquid cooling using microchannels [16,18-20] require large pressure heads to deliver the coolant at a rate such that the temperature non-uniformity across the chip, caused due to sensible heating of the fluid, is maintained below a required level. The need for a large pressure head requires larger pumps and higher power consumption, and increases the size and cost of the overall system. These growing problems associated with single-phase liquid cooling motivate us to find a more effective and efficient thermal solution.

1.2 Two-Phase Cooling

One widely researched solution to reduce this pressure head while providing large heat flux dissipation is two-phase convection in microchannels [21-24]. The large latent heat of vaporization enables comparably smaller flow rates than single-phase counterparts. Phase change also provides high heat transfer coefficients, leading to smaller thermal resistances, and may also improve temperature uniformity by maintaining the working fluid at the saturation temperature. Despite these advantages two-phase cooling faces major technical challenges that currently limit commercial application.

The growth and advection of the vapor bubbles in microchannels leads to an increase in the pressure-drop that can be approximated mathematically using the separated flow model of the pressure gradient during two phase flow in a horizontal channel, shown by Eq. (1.1).

$$-\left(\frac{dP}{dz}\right)_{tp,SFM}=\left(\frac{dP}{dz}\right)_{l}+\left(\frac{dP}{dz}\right)_{v}+C\cdot\left(\frac{dP}{dz}\right)_{l}^{0.5}\cdot\left(\frac{dP}{dz}\right)_{v}^{0.5}+Acceleration \tag{1.1}$$

The two-phase pressure gradient has three additional pressure-drop terms on the right due to friction of the vapor phase, interaction between the liquid and vapor phases and acceleration of the liquid to the vapor phase. This increase in pressure drop during two-phase flow in a variety of tubes and channels has been extensively studied over the years and the fundamental aspects are discussed in more detail in Ref. [25,26,5]. The increased pressure has also been experimentally observed in microchannels by several authors including Zhang *et al.* in silicon microchannels down to a diameter of 27μm [24] and Garimella *et al.* in circular channels down to a diameter of 0.5mm [27]. The former found the pressure drop to sharply increase by a factor of about 3 on two-phase flow and the latter found a monotonic increase in the pressure-drop by a factor ranging from 2.5 to 3 as vapor quality was increased from 2% to 18%. The large increase in the two-phase pressure drop with the vapor mass quality necessitates a larger, more power consuming pump thus negating some of the benefit of using two-phase over single-phase flows for cooling.

The increase in pressure results in an increase in the saturation temperatures as approximated by the Clausius-Clayperon relation shown in Eq. (1.2) where R is the molar gas constant and ΔH is the molar change in enthalpy during vaporization.

$$T_{sat,chan}=\left[\frac{1}{T_{sat}}-\frac{R}{\Delta\overline{\overline{H}}}\ln\left(\frac{P_{sat,chan}}{P_{sat}}\right)\right]^{-1} \tag{1.2}$$

This shift in saturation temperature delays the onset of boiling and manifests itself as an added thermal resistance as given by Eq. (1.3).

$$R_{th,tot} = R_{th,cond} + R_{th,conv} + R_{th,pres}$$

$$R_{th,pres} = \frac{T_{sat,chan} - T_{sat,amb}}{\text{heat dissipated}} \tag{1.3}$$

The large rise in the pressure drop also leads to single and multi-channel instabilities [28,29]. Wu and Cheng [28] studied flow instabilities in parallel, 186μm silicon microchannels and discuss the existence of multiple types of instabilities that occur at different mass flux and heat input rate combinations. Low-mass flux, high-heat flux conditions were found to result in large fluctuations in pressure-drop and wall temperatures. Static Ledinegg instabilities in parallel microchannel heat exchangers results in boiling in only a few channels leading to redistribution of liquid to the cooler single-phase channels and flow starvation in the hotter two-phase channels [30-32]. This problem can also manifest itself in larger systems such as server racks with nodes being liquid cooled in parallel; boiling in heat exchangers on the hottest nodes would result in flow mal-distribution at the rack level with less coolant being delivered to where it is needed the most.

1.3 Gas-Liquid Phase Separation

1.3.1 Description of the Proposed Solution

Zhou *et al.* [33] proposed the idea of vapor removal through a porous hydrophobic membrane in order to mitigate some of the problems observed during flow boiling in microchannels. A schematic of the vapor venting heat exchanger discussed in this dissertation is shown in Figure 1.2. The key component in the heat exchanger is the porous hydrophobic membrane that, through capillary forces, prevents the liquid from leaking out of the device but provides minimal flow resistance to the vapor phase. The vapor flows through the membrane into a separate set of parallel channels or plenum on the other side of the membrane. The vapor can then be reintroduced into the coolant flow downstream of the microchannels where the impact of having two-phase flow is less significant to the system. The removal of the vapor phase is predicted, by compact 1D/2D simulations (discussed in Chapter 3) and full 3-D [34] FLUENT (ANSYS Inc.) simulations, to significantly improve the pressure drop, lower device temperatures, and delay dry-out.

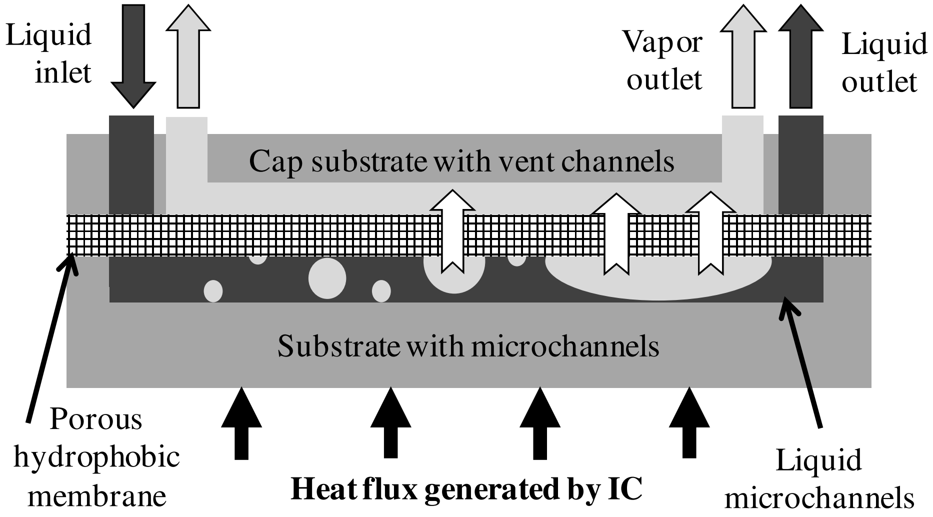
Liquid inlet
Vapor outlet
Liquid outlet
Cap substrate with vent channels
Substrate with microchannels
Porous hydrophobic membrane
Heat flux generated by IC
Liquid microchannels

Figure 1.2 Schematic of a vapor venting heat exchanger showing the three main components: the two-phase microchannels, the vapor vent channels and the porous hydrophobic membrane. The membrane separates the vapor phase from the two-phase mixture and transports it to the vent channel.

1.3.2 Phase Separation at the Macroscale

It is valuable to investigate the state of the art of phase separation techniques and applications. Phase separation has been investigated both at the macroscale and the microscale. The key application of phase separation at the macroscale is membrane distillation. Membrane distillation is used in a variety of industries for purification, desalination, concentration and separation of volatiles. Other macroscale applications of phase separation include clothing (Gore-Tex), as scrubbers/separators to help remove liquid or gas from a two-phase mixture during industrial operations and in degassing of molten alloys.

Lawson and Lloyd [35], El Bouravi *et al.* [36] and Alklaibi and Lior [37] provide reviews of the state of the art of membrane distillation and desalination including the factors that impact the distillation process, fundamentals of the vapor separation and transport process, and membrane materials. Membrane distillation, despite being a macroscale application of phase separation, is fundamentally similar to the phase separation heat exchanger proposed. However, unlike our application, membrane distillation relies on evaporation of the heated liquid across the membrane rather than boiling.

Unlike in membrane distillation, where the separation is enabled by surface tension, centrifugal and T-junction separators rely on body forces. Entrained liquid droplets often need to be removed from gas streams. To avoid the large pressure drops encountered in filter based scrubbers, a centrifugal separator could be used [38,39]. Liquid droplets impact the walls of the centrifugal separator and can be collected from the edges, as shown by Figure 1.3.A. A T-junction separator is often used to separate out two-phase flows encountered in industrial applications where the volume of liquid is too large to be scrubbed [40]. The T-junctions are oriented such that a two-phase flow entering the junction will split unevenly between the branches leaving a liquid rich flow in one branch and a gas rich flow in the other as shown in Figure 1.3.B. Repeated use of T-junctions can result in almost complete separation of the phases.

Xu *et al.* [41] describe several methods by which a molten aluminum alloy could be degassed. Methods include ultrasonic transduction to actively degas the molten aluminum alloy, inert gas bubbling and vacuum degassing. These techniques rely on a combination of diffusion across a concentration gradient and body forces to separate out the dissolved gas.

1.3.3 Phase Separation at the Microscale

At the microscale, phase separation has primarily been used for chemical/biological microfluidic applications [42-50] and in micro fuel cells [51-58]. Phase separation has also been used as a pumping technique to help drive flow and has been presented as a method to passively deliver fuel to the micro fuel cells [55-57]. Unlike at the macroscale, body forces are negligible, and phase separation is primarily achieved using surface tension forces, which can be controlled through device geometry and surface.

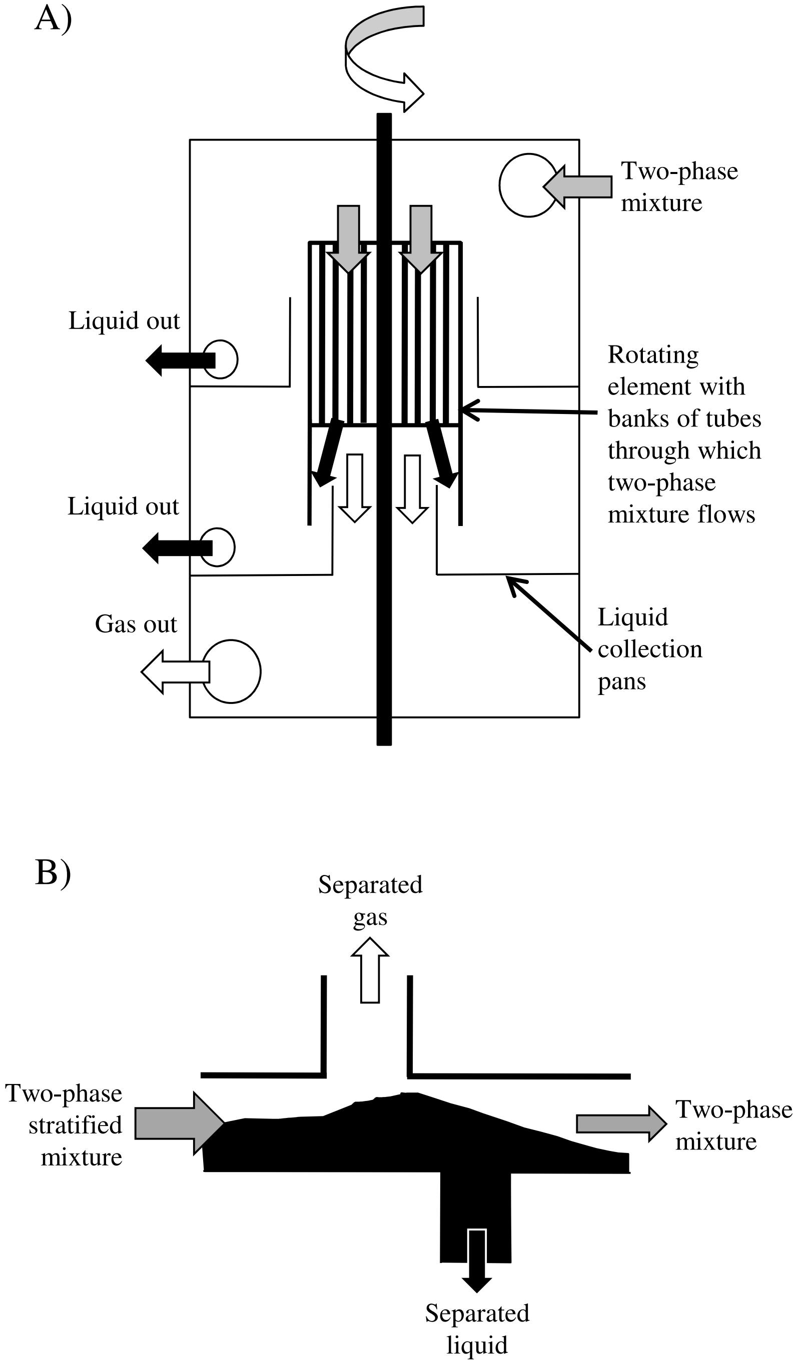
A)
Two-phase mixture
Liquid out
Rotating element with banks of tubes through which two-phase mixture flows
Liquid out
Gas out
Liquid collection pans
B)
Separated gas
Two-phase stratified mixture
Two-phase mixture
Separated liquid

Figure 1.3 Schematic view of the A) rotating phase separator described in Ref. [39] to separate out the liquid from a liquid droplet dispersed two-phase flow using centrifugal forces and B) T-junction based flow separator as described in Ref. [40] where a series of oriented junctions can be used to separate out the phases.

In microfluidic devices, the principle motivation for phase separation is the need to remove dissolved gases in the working fluids or remove trapped bubbles introduced during filling operations. Air bubbles are cytotoxic to cells and can result in cell membrane rupture [46]. Biological applications are limited by the need for biocompatible materials resulting in the majority of the previous studies exploring gas diffusion and removal through PDMS. Due to the very low permeability of ~1e-20 m^2, the gas removal rates are typically sub µl/min. Due to the low gas removal rates, microfluidic devices rely on bubble trapping using stepped structures and changes in cross-sectional area, to hold a bubble in place long enough for it to diffuse out of the microstructure. An example of a structure to capture and remove bubbles is provided by Sung *et al.* [50]. The device is composed of a two-layer structure, with the lower layer consisting of fine flow passages while the upper layer consists of a large plenum separated by a series of sieve like barriers. Incoming bubbles prefer to exit the smaller flow channels on the lower layer of the two-level device and fill the open areas between the sieves. This structure allows liquid to flow relatively unhindered around the bubbles and in the smaller flow channels while allowing the bubble to diffuse out of the device at a rate of 0.6 µl/min.

Unlike the passive degassing techniques common in the field, active degassing was demonstrated by Yang *et al.* [42] for portable dialysis applications. Ultrasonic transduction using an attached PZT was used to coalesce dissolved gas in the working fluid, which was then removed through hydrophobic treated side channels. At high driving voltages on the PZT almost 50% of the dissolved oxygen was removed, demonstrating the usefulness of such a device in controlling dissolved gas content in a liquid.

Meng *et al.* [52,53] at UCLA have carried out several thorough investigations in passive gas venting from water and methanol solutions for degassing applications in direct methanol fuel cells (DMFC) where the CO_2 formed at the anode inhibits delivery of the methanol to the fuel cell by plugging the microchannels (a problem not unlike that faced in two-phase microchannel heat exchangers). In a recent paper [53], they focused on the venting of gas bubbles from water and methanol solutions at room temperatures with top-down visualization carried out through commercially available, semi-transparent, polypropylene membranes. Air is introduced into the venting structure upstream and vented through the polypropylene membrane at trans-membrane pressures of 3.4 to 13.8 kPa. The introduced air bubbles were found to shrink in size as they traveled through the channel due to venting and a bubble evolution model was developed to describe this.

Concurrent with our own studies, Alexander and Wang [59] recently carried out a study of adiabatic gas venting from a microchannel for heat exchanger applications. They carried out side-visualization of air venting from an air-water mixture in a microfabricated silicon device with the pores directly fabricated into the channel side wall. The micron scale pores were surface treated to provide hydrophobicity. They carried out visualization of air-water mixtures at water inlet velocities ranging between 0.5 and 3.8 cm/s and pressures up to 8 kPa and observed air removal rates up to 50μl/min. They determined that air removal rate increases with the ratio of the pressure drop across the breather (pores) to the pressure drop across the bubble and that this ratio increases with channel aspect ratio (Height/Width) and decreases with liquid flow velocity.

A key drawback in the presented microscale studies is the typically low gas removal rates, incompatibility of the materials for use at high temperatures, low flow velocities and operating pressures and the use of adiabatic gas-water flows. Though useful insights can be derived from these studies it is not clear how applicable they are at the operating conditions encountered in a two-phase heat exchanger dissipating heat fluxes between 500 and 2000 kW/m^2. The required flow-rates and expected pressures are also much higher than previously studied. The lack of previous work exploring phase separation in heat exchangers helped define the objectives for my research work.

1.4 Objectives and Approaches

Due to the lack of previous work in phase separation heat exchangers, the overall goal of my work is to develop a broad understanding of the microfluidic phase separating heat exchanger technology, its underlying physics, its strengths and its limitations and then to apply this understanding to optimize the heat exchanger design and recommend areas for targeted future research.

To achieve this objective requires knowledge of the flow phenomena, an understanding of how various heat exchanger geometric and flow conditions impact the phase separation process and performance metrics, and the design, demonstration and characterization of a phase separating heat exchanger operating under a real world thermal load.

In Chapter 2, I present our results from high speed visualization studies of the flow phenomena encountered during adiabatic gas venting and diabatic vapor venting in a single microchannel. The adiabatic results were used to construct a new flow regime map for gas venting flows. Analysis of the data helped outline some of the factors that impact gas removal. The diabatic results were also summarized in a regime map and highlighted the differences with adiabatic operation. Diabatic visualizations also helped generate a preliminary understanding of the potential impact of flow regime on thermal and hydraulic performance.

In Chapter 3, I present a two-phase vapor venting flow model based on new two-phase pressure drop and heat transfer correlations. The compact model was used to study a variety of factors including the impact of channel diameter, liquid-to-vent channel diameter ratio, membrane conductance, channel density and substrate properties on the venting, hydraulic and thermal performance. Based on these studies we find that the vapor venting heat exchanger is only beneficial under certain limited conditions. Based on these findings I propose some design and material directions that would elevate the performance of the vapor separating heat exchanger over a traditional volumetrically equivalent heat exchanger.

In Chapter 4, I discuss the design, fabrication and characterization of a silicon gas venting device as well as a copper vapor venting heat exchanger dissipating up to 820kW/m^2. We identify a successful fabrication process for a silicon heat exchanger that opens the door for exotic channel designs and direct IC backside cooling. Characterization of the copper device finds hydraulic and thermal improvements over a non-venting control heat exchanger. We also find deviations between the experiment and the model and use the visualized flow phenomena from Chapter 2 to explore the possible source of the discrepancy. The results highlight the importance of flow phenomena and bulk characterization in developing a more accurate two-phase vapor venting model.

Chapter 5 provides a conclusion to the work and summarizes the key findings from each chapter, highlights the key contributions of the work to the field and outlines future research directions.

Gaining a solid understanding of phase separation in a microfluidic heat exchanger, and then applying this understanding to develop more effective two-phase heat exchangers that enjoy the thermal benefits of thin film evaporation and reduced saturation temperatures and the hydraulic and stability benefits of single-phase like pressure drops, could significantly improve the potential of two-phase microfluidic heat exchangers as a highly effective and energy efficient thermal management solution, particularly for high performance computing systems.

CHAPTER 2 ADIABATIC AND DIABATIC TWO-PHASE VENTING FLOW PHENOMENA IN A MICROCHANNEL

2.1 Motivation and Overview

Visualization of the vapor/gas venting from a microchannel is a critical element in understanding the vapor separation process during two-phase flow in compact geometries. High speed observations can be used study the factors that impact vapor and gas removal, optimize vapor venting channel designs and help delineate bulk device measurements where visual access of the venting process may not be possible.

In Section 2.2 we discuss the development and testing of a copper visualization device that allows for side-visualization of the air-water and vapor-water flow structures while using commercially available opaque, hydrophobic, microporous membranes. This visualization device overcomes the need to have transparent and semi-transparent membranes [53,52] or the need to microfabricate them directly into the structure [59]. Visualization of both adiabatic and diabatic two-phase flows help develop a better understanding of gas and vapor venting from microchannels. The advantage of adiabatic experiments, presented in Section 2.3.1, is the ability to accurately control the inlet quality and measure the gas venting rate while avoiding the complexities introduced by evaporation and condensation to the venting process. This allows us to carry out a more detailed analysis of the factors affecting venting rate and help generate design guidelines for gas and vapor venting devices. The adiabatic results are also applicable for use in fuel cells and microfluidic chemical and biological devices where gas venting is of great interest. The diabatic vapor venting results, presented in Section 2.3.2, helps provide a clearer picture of the impact of phase change in a vapor venting channel and is included to highlight some of the key features of vapor venting flow regimes that aren't manifested during adiabatic operation. These flow regimes help explain some of the thermal and hydraulic characteristics observed in a bulk vapor venting copper microchannel heat exchanger, discussed in greater detail in Chapter 4.

2.2 Experimental Method

2.2.1 Device design and fabrication

The device is designed to provide visualization of adiabatic air and diabatic vapor venting from two-phase flow produced by the injection of air into a water stream and by heating respectively. All the materials used in the fabrication were chosen to be thermally stable up to 125ºC. The cross-sectional and top views of the copper microchannel device are shown in Figure 2.1. The device is assembled from four separate pieces, labeled 1 through 4, that are screwed together with the membranes sandwiched between the liquid and vent halves of the device. The copper bodies, pieces 1 and 3, are made from electronics grade, polished copper with the microchannels end-milled with a high precision CNC facility. The liquid microchannel, machined in piece 1, has a length of 24mm, a width of 124µm and a depth of 98µm (hydraulic diameter = 110µm). This air injection channel, also machined in piece 1, is 2.5mm long, 132µm wide and 40µm deep, with a hydraulic diameter of 62µm. The air injection port needs to have a small hydraulic diameter to approximate a bubble nucleation site. The air injection channel intersects the liquid channel 6mm from the liquid inlet. The vent microchannel, machined in piece 3, has a length of 24mm, a width of 140µm and a depth of 150µm, with a corresponding hydraulic diameter of 145µm.

The gas/vapor separation membrane that faces the liquid carrying microchannel is an isotropically porous, unlaminated, hydrophobic Teflon with a 220nm effective pore diameter and a thickness of 65µm ± 5µm (Sterlitech Corp., WA, USA and GE Osmonics, MN, USA). This hydrophobic membrane allows transfer of the gas phase but holds back the liquid phase through surface tension forces.

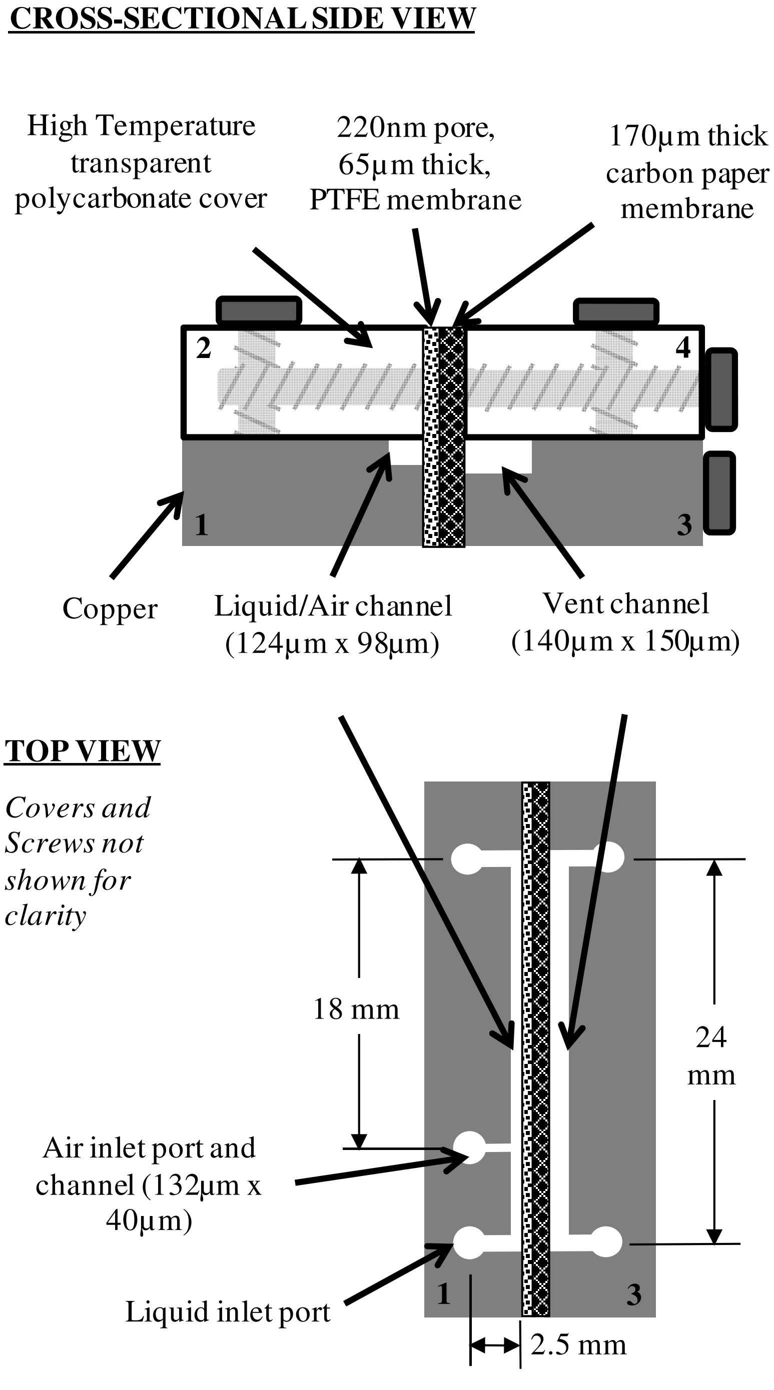
CROSS-SECTIONAL SIDE VIEW
High Temperature transparent polycarbonate cover
220nm pore, 65µm thick, PTFE membrane
170µm thick carbon paper membrane
2
4
1
3
Copper
Liquid/Air channel (124µm x 98µm)
Vent channel (140µm x 150µm)
TOP VIEW
Covers and Screws not shown for clarity
18 mm
24 mm
Air inlet port and channel (132µm x 40µm)
Liquid inlet port
1
3
2.5 mm

Figure 2.1 Cross-sectional side and top views of the copper microchannel device (figures are not to scale).

Assuming straight capillary pores and using the Young-Laplace equation the leakage pressure for the liquid phase is given by Eq. (2.1) [53],

$$\Delta P = \frac{4 \cdot \sigma \cdot \cos(\pi - \theta_{adv,\max})}{d} \tag{2.1}$$

where the surface tension, σ = 0.072 N/m, the advancing contact angle for water on Teflon, $\theta_{adv,max}$ = 123° [60] and manufacturer stated pore diameter, d = 220nm. The liquid breakthrough pressure for the Teflon membrane is found to be in excess of 700kPa. The maximum pressure encountered in our current experiments is less than an eighth of this value. A mechanically stiff, hydrophilic, carbon-mesh membrane (Toray Carbon Paper, courtesy of Honda Corp, Japan) with isotropic pores of diameters in the order of 10's of microns and a thickness of 170µm ± 10µm is added to provide mechanical support and stop the membrane from deforming and impeding visualization of the venting process.

2.2.2 Experimental Setup

The experimental setup for the adiabatic experiments is shown in Figure 2.2. Distilled water, filtered through 0.5µm and 20nm in-line filters, is pumped into the device using a Shimadzu LC-10AD peristalsis pump. Liquid inlet pressure is measured using an Omega PX219-30V45G5V pressure sensor with an accuracy of 5.4Pa. Liquid inlet flow rate is measured using a Sensirion SLG1430-24 flow meter with an accuracy of 10% of the measured value. Air, filtered through a single 20nm in-line filter, is pumped into the device through the air injection port using a syringe pump fitted with a 100ml glass syringe. Air pressure is measured using an Omega PX01C1-015G5T pressure sensor with an accuracy of 1Pa. Air volumetric flow rate is measured using a Sensirion CMOSense EcoLine EM1NL gas flow meter with an accuracy of 0.15ml/min. All thermocouples used are Omega 40 gauge, type K thermocouples and were converted to millivolt signals using Fluke 80TK and Omega SMCJ-K thermocouple-to-analog converters. The pair of IR slot sensors is used to determine interface velocities of air slugs in the outlet tubing. The distance between the sensors is 6.45mm and for a sampling rate of 200Hz can resolve interface velocities up to 1.29m/s. By measuring the front and back interface velocities of the air plug as well as the total residence time, the volume of each air slug and the air flow rate in the outlet tubing can be determined. The clamp on the outlet tubing allows us to raise the total static pressure of the device.

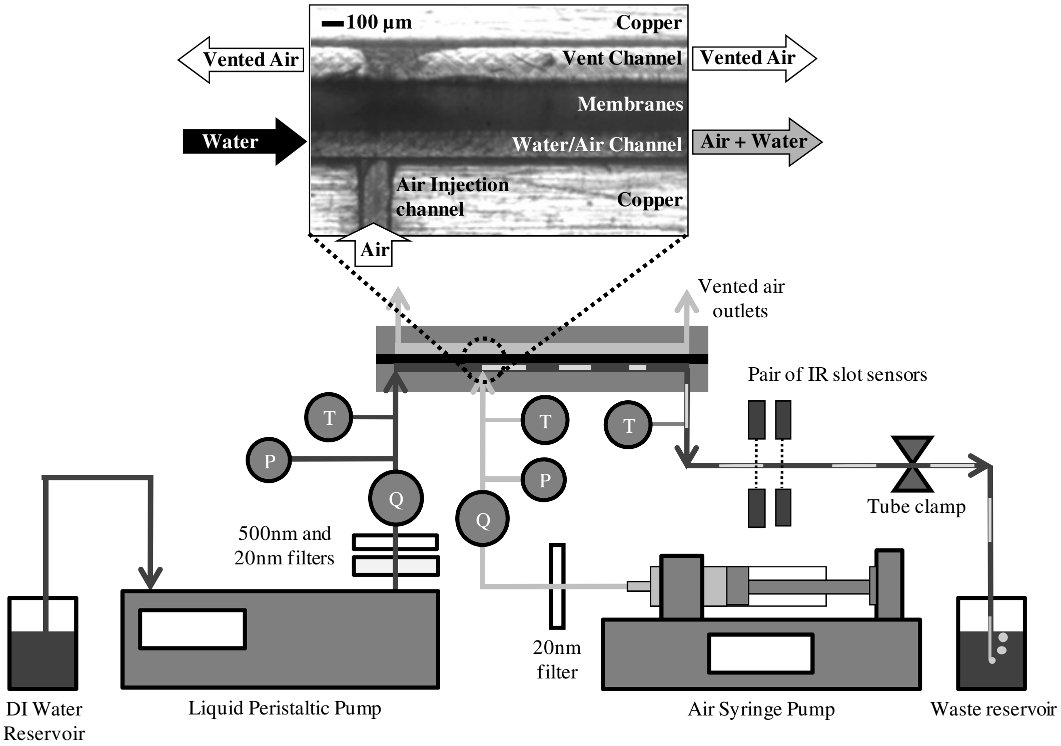
100 µm
Copper
Vented Air
Vent Channel
Vented Air
Membranes
Water
Water/Air Channel
Air + Water
Air Injection channel
Copper
Air
Vented air outlets
Pair of IR slot sensors
T
P
T
T
P
Q
Q
Tube clamp
500nm and 20nm filters
20nm filter
DI Water Reservoir
Liquid Peristaltic Pump
Air Syringe Pump
Waste reservoir

Figure 2.2 Experimental setup showing key equipment and close up of channel. T represents a thermocouple, P, a pressure sensor and Q, a flow meter. Liquid is pumped using the peristaltic pump and air is delivered by the syringe pump. The vent side of the channel is left open to the atmosphere. Non-vented air flow rate in the outlet tubing is measured using the pair of IR slot sensors that measure air slug velocities and residence times.

For the diabatic experiments, the air injection port is blocked and the air-injection equipment is not used. Vapor is generated by uniformly heating the side opposite the visualization surface with a 10W Kapton heater. Device temperatures were measured approximately half way along the main channel using a thermocouple. The parasitic heat loss for each flow rate was estimated from inlet and outlet fluid temperatures obtained during sensible heating of the fluid. This heat loss was found to be approximately 73% at the mass flux of 140 kg/s-m^2 and 52% at the mass flux of 340 kg/s-m^2. This calculated heat loss was applied during two-phase flow to estimate the thermodynamic exit quality, x_e, as given by Eq. (2.2), where m is the mass flow rate of liquid, C_p the heat capacity and ΔH_{fg} the latent heat of vaporization.

$$x_e = \frac{\left(1 - q_{loss\%}\right)\cdot q_{in} - \dot{m}\cdot C_p \cdot \left(T_{sat} - T_{in}\right)}{\dot{m}\cdot \Delta H_{fg}} \tag{2.2}$$

For adiabatic air-injection flows the initial inlet quality, x_i, is calculated using Eq. (2.3) where m_{liq} is the liquid mass flow rate and m_{air} is the air mass flow rate calculated from the volumetric flow rate and pressure dependent density.

$$x_i = \frac{\dot{m}_{air}}{\dot{m}_{air} + \dot{m}_{liq}} \tag{2.3}$$

Videos of the flow structures in the microchannel were recorded using a Vision Research Phantom v7.3 high-speed camera at rates of 5,000 to 20,000 frames per second. Voltage data from the thermocouples and pressure sensors is collected through a NI SCB-100 breakout box connected to an E-series NI DAQ card. Numeric data from the Sensirion flow meters were collected through two COM ports. Data and image collection were carried out on two separate computers but were triggered simultaneously using LabView. Baseline data was collected at the beginning of every experiment to correct for any offsets in the sensors. Single-phase liquid flow data was collected at several flow-rates to determine the single-phase hydraulic resistance per unit length of the liquid channel.

2.3 Results and Discussion

2.3.1 Adiabatic Air-Water Flow

2.3.1.1 Visualization of Flow-Regime

An example of adiabatic air venting through the membrane is shown in Figure 2.3, where the air velocity is 0.32m/s (5.6×10^{-9} kg/s) and the liquid velocity is 0.36m/s (4.3×10^{-6} kg/s). The sequence shows a bubbly type flow that is typically observed at low inlet air flow rates with the size of the bubbles increasing with air injection velocity. Bubbly type structures were also often observed downstream at the tail end of many of the other flow structures, which we attribute to the reduction of superficial air velocity due to air venting through the membrane.

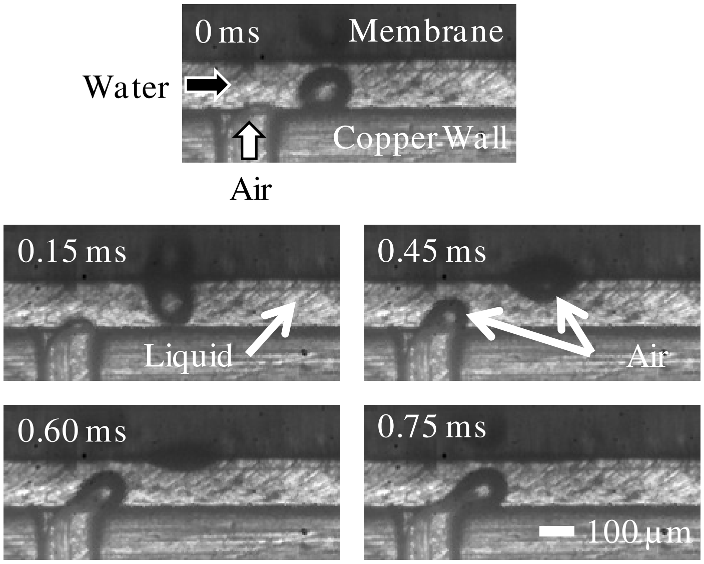

Figure 2.3 Sequence of images showing an example of bubbly air venting at a liquid velocity of 0.36m/s and an air injection velocity of 0.32m/s. As air is injected into the liquid stream, small bubbles break off the injection port (0ms) and attach to the membrane (0.15ms) through which the air can now escape causing the bubble to collapse (0.15ms-0.6ms) until it eventually disappears (0.75ms). As air flow rate is increased the bubbles get larger and move along the membrane surface once attached.

Figure 2.4 provides examples of the other major types of flow structures that were observed near the air injection port during the experiments and Figure 2.5 summarizes these observations on a superficial velocity regime map.

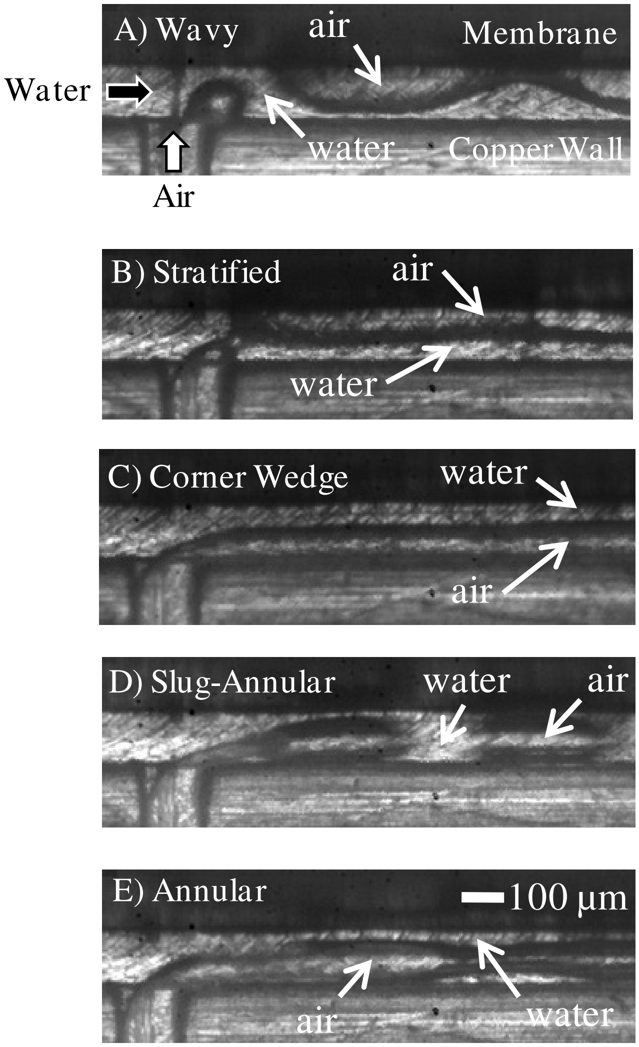
A) Wavy
air
Membrane
Water
water
Copper Wall
Air
B) Stratified
air
water
C) Corner Wedge
water
air
D) Slug-Annular
water
air
E) Annular
100 μm
air
water

Figure 2.4 Examples of steady state flow structures that were observed at different air and water velocities. A) Wavy flow, B) Stratified flow, C) Corner-wedge flow, where the flow structure forms on the plastic-copper corner, D) Slug-annular flow and E) Annular flow. The latter two flow regimes are observed at the highest tested Weber number of 0.6.

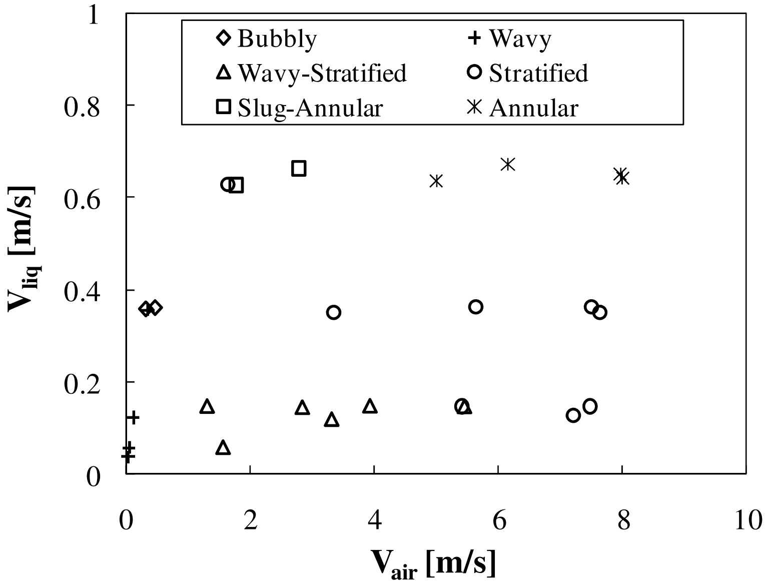

Figure 2.5 Superficial velocity flow regime map for adiabatic air-water two-phase flow in a microchannel with one porous hydrophobic wall.

For the liquid velocity range of 0.1 to 0.15m/s, as air velocity is increased to approximately 1.2m/s, the structure changes from bubbly to wavy (Figure 2.4.A) where the wavy flows are essentially several large static coalesced bubbles. As air velocity is increased to approximately 5.2m/s we see a mixed wavy-stratified/stratified type flow that transition from regions that start wavy-stratified, smooth out downstream and then end with a region of waviness and bubbly type flow. The waviness near the injection is due to the initial interaction between the air stream, the liquid stream and membrane, with the air velocity not sufficiently high to allow the air to uniformly spread across the membrane. At air velocities of 5.2m/s and above, smooth stratified flows are observed which then transition to wavy-stratified flows downstream (Figure 2.4.B). Stratified flows are only typically observed in horizontal macrochannels due to gravity but are produced here due to surface tension.

In the case of liquid velocities in the range 0.35 to 0.36m/s, the structure transitions from bubbly to stratified flow as air velocity is increased. A corner wedge structure (Figure 2.4.C) also occasionally manifests itself at the highest tested air velocity of 7.55m/s. This corner wedge structure spatially transitions to a regular stratified flow downstream. The location of the transition varied, but occurred within 3mm of the air-injection port.

At the highest liquid velocity of 0.63-0.67m/s, we again occasionally observed the corner wedge structure which at the lowest air velocity of 1.6m/s spatially transitions directly to a regular stratified flow, but on slight increase to 1.8m/s, transitions to slug and then bubbly flows on the membrane instead. As air velocity is increased from 1.8 to 2.8m/s, annular-slug (Figure 2.4.D) structures first become dominant and then, at velocities greater than 5m/s, changes to more continuous annular structures (Figure 2.4.E). The spatial transition of these annular flows to stratified and bubbly flows occur several millimeters downstream and increases with the superficial air velocity.

In general, traditional two-phase flow regimes maps, developed for mini and macro scale channels (with diameters larger than a millimeter or so), such as the widely adopted map and transition criteria developed by Taitel and Dukler [61] for gas-liquid flow in horizontal channels cannot be applied for two-phase flow in microchannels due to the impact of surface tension and confinement effects (as indicated by small Bond numbers), which lead to differing flow regimes. This is described in greater detail along with a comprehensive summary of previous work in the development and application of two-phase flow regime maps by Cheng *et al.* [62]. Chung and Kawaji [63] and Cubaud and Ho [64] are recent examples of adiabatic microchannel flow visualization and regime map development. Chung and Kawaji considered flow in circular glass capillaries of diameters ranging from 50µm to 526µm, with two phase flow generated by injection of nitrogen into the water stream at a mixer. They found that flow regimes observed in the 250µm and 526µm diameter capillaries were different from those observed in smaller 100µm and 50µm capillaries. Cubaud and Ho looked at two-phase air-water flow in rectangular, serpentine silicon channels of hydraulic diameters 200µm and 525µm and found a unique wedging type flow with liquid flowing along the corners of the channels.

To more closely mimic gas/vapor formation in real devices such as fuel cells and heat exchangers the air injection in our device is asymmetric, using a T-junction, which can lead to differing flow regimes as compared to coaxial liquid injection, as was used by Cubaud and Ho [64] and Chung and Kawaji [63] making a direct comparison between their observations and ours less appropriate. As experimentally observed by Garstecki *et al.* [65] and simulated by De Menech *et al.* [66], T-junction injection can lead to differing flow regimes with 'squeezing' type flows at low Capillary numbers (seen in Figure 2.3), 'dripping' flows at intermediate capillary numbers and 'jetting' type flows (seen in Figure 2.4.D and Figure 2.4.E) at higher capillary numbers. Though a comprehensive flow regime map for T-junction two-phase flows is not currently available the work of Garstecki *et al.* and De Menech *et al.* indicate that the liquid capillary number and the velocity ratios of the continuous and dispersed gas phase play an important role in the type of flow generated. The size of the structure is dependent on the velocity ratio, with $V_{air}/V_{liq} < 1$ leading to smaller bubbles and $V_{air}/V_{liq} > 1$ generally leading to larger structures as seen in Figure 2.5. The capillary number on the other hand determines the type of breakup that occurs as described above. Pressure mediated breakup at low capillary numbers is not considered to be as significant in our work since the depth of the injection port is smaller than that of the main channel and the air structures do not fill the cross-section of the channel as they grow. The 'squeezing' type breakup is only observed during bubbly flow at $V_{air}/V_{liq} \sim 1$ and Ca = 0.005, about a factor of two smaller than suggested by Garstecki *et al.* Higher velocity ratios and the hydrophobicity of the membrane help stave off breakup at higher velocity ratios by creating 'bridges' of gas connecting the injection port to the membrane. 'Jetting' flow leading to annular-slug and annular flows structures occurs begins in the range $0.005 < Ca < 0.009$ ($0.2 < We < 0.6$) where the liquid velocity is now sufficiently high to stop the injected air column from reaching the membrane and causing it to breakup downstream. This type of breakup is less amenable to gas venting as it leads to the vapor being surrounded by liquid films that stop the gas from reaching the membrane and venting.

2.3.1.2 Air-Venting Analysis

A closer analysis of venting area, Weber number, flow-regime and static pressure on air venting rates reveal useful design guidelines for gas/vapor venting devices. Since surface tension and inertial forces, rather than viscous forces, play an important role in our device, we choose the Weber number, $We = \rho V^2_{liq} D_h/\sigma$, where ρ is the density of the liquid, σ is the surface tension and D_h is the hydraulic diameter of the main channel, as the dimensionless parameter of interest for liquid flow.

Figure 2.6 highlights the role of Weber number and flow structure on the air venting rate at different pressures. At low inlet air flow rates where the two-phase pressure drop at the injection point is less than 20kPa, bubbly and wavy type flows dominate and result in complete venting of the injected air. As air injection at the two lower liquid velocities increase, the mass quality increases and results in an increase in the two-phase pressure drop. The flow-regime also changes to wavy-stratified and stratified. At the highest flow velocity and Weber number, annular type flows are dominant. Annular type flows require a much larger pressure to vent a given amount of vapor as compared to the lower Weber number flows and the increase in air removal rate with pressure (slope of the curve) is smaller than for the two lower liquid velocities.

Figure 2.7 and Figure 2.8 help explain the behavior observed in Figure 2.6 and also delineate the role of venting area to the venting performance. Points marked *, #1 and #2 in these figures and in Figure 2.9 are special flow circumstances that is discussed at the end of this section. Figure 2.7 considers the impact of the Weber number and quality on the venting rates by looking at the venting rate per unit system pressure (as measured at the T-junction) as the inlet quality is increased (by increasing the air injection rate). The venting rate per unit pressure, i.e. the venting effectiveness, should be maximized. As mass quality increases, there is initially a linear increase in the venting effectiveness followed by a roll-off as the venting effectiveness is maximized. For the low and intermediate flow rates this roll-off occurs at around $6x10^{-12}$ kg/s-Pa. However, for the higher Weber number flow the roll-off occurs much lower at around $2x10^{-12}$ kg/s-Pa.

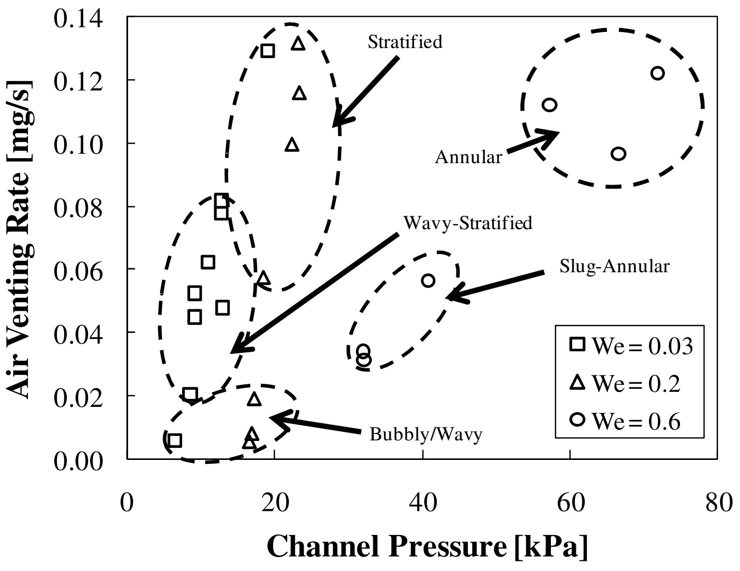

Figure 2.6 Air venting rate vs. pressure as measured at the air injection port. The type of flow-regime experienced influences the rate of air removal through the membrane. At the two lower Weber number flows, most of the air injected is removed but this is not the case at the higher Weber number flow, where differing flow regimes and partial venting result in higher pressure drops.

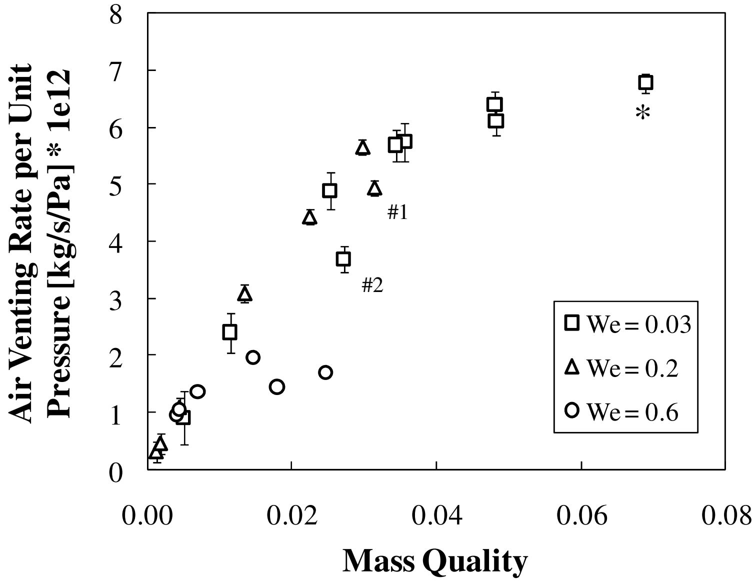

Figure 2.7 Air venting rate per unit injection point pressure (venting effectiveness) vs. Mass quality. The poor effectiveness of the highest Weber number flow is clearly seen with a roll-off of around 2×10^{-12} kg/s-Pa as compared to 6×10^{-12} kg/s-Pa for the lower Weber number flows. High Weber number flows can result in less desirable corner-wedge (#1) and annular type flows that delay venting and reduce the maximum venting effectiveness.

A plot of the normalized venting area with the quality, shown in Figure 2.8, indicates that the slope and roll-off in Figure 2.7 is related to the venting area. The venting area is the contact area between the air structure and the membrane and is measured directly from the images. This venting area increases linearly with quality until a value of 3% at which point all the available area has been utilized and air begins to appear in the outlet tubing. The roll-off in Figure 2.7 occurs at approximately the same quality, and the slope of the linear region in Figure 2.7 is found to be equal to $B \times A_{vent}$ where B is a constant. Thus venting effectiveness continues to rise as long as there is area to vent through and is maximized when all the area has been used up. At the highest Weber number however, where inertial forces are now becoming increasingly more important, the formation of long annular air structures at qualities > 1% impedes the air structures from contacting the membrane until much further downstream resulting in a much smaller total venting area seen by the air before reaching the outlet manifold. This results in the lower roll-off as seen in Figure 2.7.

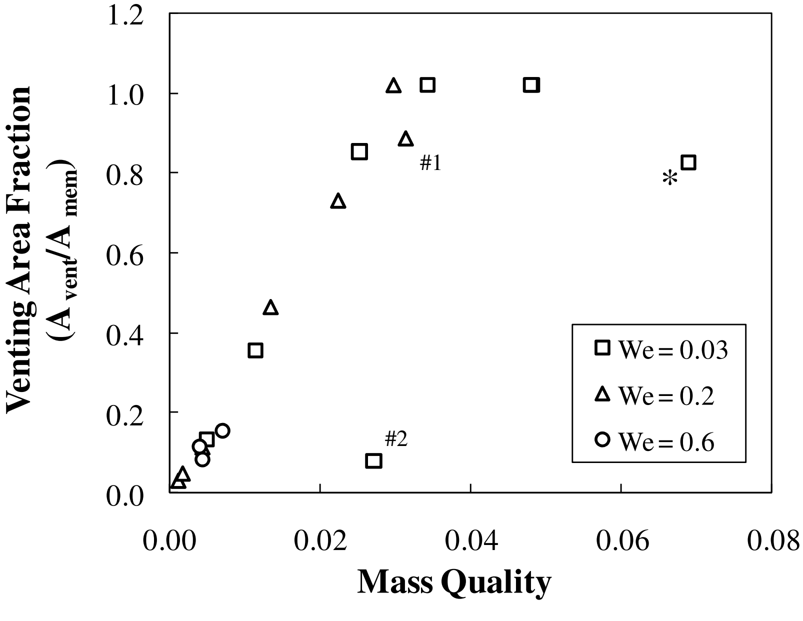

Figure 2.8 Normalized venting area vs. Mass quality. Contact area between air and membrane increases linearly with quality until all area has been utilized. At this point, the venting effectiveness is maximized and further venting occurs only if pressure is increased. At increased trans-membrane pressures (*), upstream venting rate increases, freeing more space for venting.

These plots indicate that as long as the air-structure does not result in separation of the gas phase from the membrane then the venting effectiveness is insensitive to the Weber number under the tested conditions. The Weber number is important however as it determines the manner of breakup of the dispersed gas phase during injection, which in turn determines how effectively the gas phase is brought into contact with the membrane. From a gas/vapor venting device design standpoint, it is important to maximize the total potential interaction area between the gas/vapor phase and the membrane, thus increasing the amount of gas/vapor a channel can support before its venting effectiveness is maximized. For a gas venting device it is also important to design the system for smaller Weber numbers to avoid the formation of annular type flow structures. This design rule doesn't necessarily apply for thermal vapor venting devices however as discussed in Section 2.3.2.

Since the slope of the linear region in Figure 2.7 is directly related to the venting area, assuming Darcy flow in the membrane, the venting rate per unit area per unit pressure must be a constant and equal to the membrane and fluid properties. To verify this it is necessary to determine the actual pressure experienced by the air structure. To determine this driving pressure, we measured the position and length of the venting structure, and then eliminated the single-phase liquid pressure contribution in the section upstream and downstream of the structure using the experimentally determined single-phase hydraulic resistance. We use the mean of the pressure across the structure as the driving pressure for venting, assuming that the pressure varies linearly along the structure. In the case of smaller bubbly type flows where curvature is significant, we incorporated the additional Laplace pressure with an average radius estimated from images taken during venting. Since the PTFE separation membrane is isotropic and the exposed areas on either side of the membranes are not equivalent (see Figure 2.1) we include a spreading effect in the determination of the venting area, with the dimension of the venting footprint (approximated as a rectangle) increased by half the thickness of the membrane stack. The venting footprint 'rectangle' assumes that the air structure stretches depth-wise through the channel which is valid in most wavy and stratified flows and some larger bubbly flows. The result of the calculations is shown in Figure 2.9. The venting flow rate per unit area per unit pressure is almost a constant for the tested mass qualities but shows a slight upward trend with quality, believed to be due to an increasing underestimation in the venting area when the structure spans a large fraction of the channel.

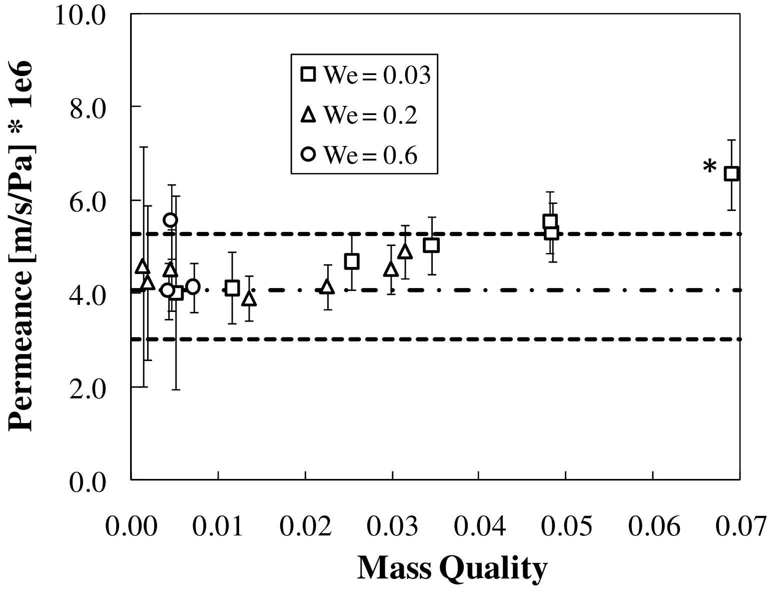

Figure 2.9 The venting rate per unit area per unit pressure (permeance) generally matches the theoretically calculated value of $4.1\mathrm{x}10^{-6} \pm 1.1\mathrm{x}10^{-6}$ m/s-Pa (– · – and – – respectively). The theoretical value is determined from the membrane thickness and intrinsic permeability measurements [67].

To compare this result with the membrane permeance, we used the experimentally determined value for the intrinsic permeability of the Teflon 220nm membrane of $5\mathrm{x}10^{-15}$ m^2 (5 milli-Darcy) [67] and determined the theoretical membrane permeance to be $4.1\mathrm{x}10^{-6}$ m/s-Pa ± $1.1\mathrm{x}10^{-6}$ m/s-Pa using Eq. (2.4).

$$\Phi_{mem} = \frac{Q_{air}}{\Delta P \cdot A} = \frac{\kappa}{t_{mem}} \cdot \frac{1}{\mu_{air}} \tag{2.4}$$

The membrane permeance, Φ_{mem}, assuming single-phase Darcy flow in the membrane, depends on just the thickness of the membrane, t_{mem}, its intrinsic permeability, κ, and the fluid dynamic viscosity μ. The intrinsic permeability depends on the structure of the pores and the porosity and typically scales with the square of the pore diameter. Since the intrinsic permeability of the carbon mesh support membrane varies between $1\text{x}10^{-12}$ and $12\text{x}10^{-12}$ m^2 (1-12 Darcy) [68,69] its contribution to the total permeance is neglected. The agreement between the current results and that theoretically predicted using Eq. (2.4) emphasizes that air venting is fundamentally limited by the membrane properties and it is important to choose a membrane that is both thin and has high gas/vapor permeability.

To study the impact of trans-membrane pressure on the venting performance we tightened the clamp shown in the setup in Figure 2.2 to increase the static pressure on the two-phase side of the device. The trans-membrane could also be increased by adding a vacuum to the vent channel on the other side of the membrane. The increase in static liquid pressure resulted in the data point indicated by the star (*) in Figure 2.7 through Figure 2.9. The rise in pressure increases the air vented at every point in the venting structure, causing the air structure to shorten and recede back upstream, reducing the normalized venting area from 1 to 0.8 as seen in Figure 2.8. In Figure 2.7, this would result in a higher roll-off, since the higher static pressure in the device has freed up more venting area. Thus, we could increase the maximum venting effectiveness by increasing the trans-membrane pressure.

The point marked #1 in Figure 2.7 through Figure 2.9, had a long 2.5mm corner-wedge flow before transitioning to a stratified flow. The corner flow is not ideal for venting by reducing the potential venting area as seen in Figure 2.8, and the venting effectiveness rolls-off at a slightly lower value than expected for the given Weber number and quality in Figure 2.7. The other data-point of interest, marked #2 in the previous figures, indicates an unusual flow regime, where instead of developing a stratified flow, the structure instead resembled a short corner-wedge flow followed by bubbly/slug type flow. This flow structure was only observed once during testing.

2.3.2 Diabatic Vapor-Liquid Flow

2.3.2.1 Visualization of Flow-Regime

Though the adiabatic visualization and analysis provides useful insight for gas and vapor venting devices it is valuable to consider the types of flow regimes encountered during phase change and how they might specifically inform heat exchanger design. Figure 2.10 and Figure 2.11 provide examples of the flow regimes that were observed during diabatic operation. With an average mass-flux velocity of 140 kg/s-m^2 and thermodynamic exit quality of less than 1%, the flow structures are initially bubbly type flow (Figure 2.10.A) with individual bubbles nucleating and growing on the copper surface and then venting through the membrane, similar to the adiabatic venting sequence shown in Figure 2.3. As the quality increases we see slug type flow (Figure 2.10.B) with a distinctive asymmetric front and back interface due to the non-wetting hydrophobic membrane. When the quality exceeds 1%, stratified flow becomes dominant (Figure 2.10.C) with the liquid film thickness reducing as quality increases.

We also observed bubble nucleation and growth within the stratified region with the bubble breaking through the liquid film and merging with the vapor film once it has grown large enough. As quality increases further we begin to observe a cyclical stratified flow. This cycle initially starts with a wetting phase where liquid slugs initially wet the copper surface, followed by the establishment of the stratified flow structure. Over time the film thickness in this stratified region gradually reduces until eventually there is a dry-out period where there is only vapor flowing through the channel at the observed location. At the highest tested quality of 10% this cycle was found to last approximately 0.1 to 0.12 seconds. This cyclical behavior has been experimentally observed in microchannels and the process described by Kandlikar [70] and modeled by Thome *et al.* [71]. However, in these and other previous work in this field, the cyclical process involves a liquid only period, followed by a period of annular flow with thinning liquid films followed by a dry region. Due to the hydrophobicity of the membrane in our channel, the annular region is replaced with a stratified region, and liquid slugs that fill the entire cross-section are replaced with liquid droplets travelling on just the wetting surfaces.

For the liquid mass flux of 340 kg/s-m^2, at low qualities, we observe larger bubbly type vapor structures that, unlike the smaller bubbles formed at the lower mass flux, form on the membrane rather than the copper surface (Figure 2.10.D). This may be due to growth of vapor pockets in the membrane due to evaporation. If the rate of vapor removal through the membrane is smaller than the rate of vapor generation in these vapor pockets then they would grow into the channel as observed. Stratified flow is observed at higher qualities similar to the lower flow-rate but the liquid films are generally thinner with liquid also flowing as droplets on the membrane surface. In the quality range between 6% and 11% we begin to see cyclical behavior, but the flow structures are quite different from the lower-flow rate case.

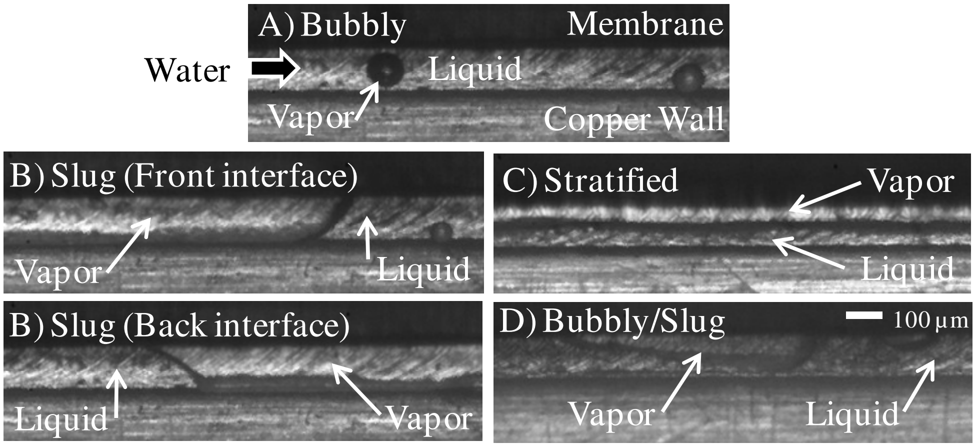
Water
A) Bubbly
Membrane
Liquid
Vapor
Copper Wall
B) Slug (Front interface)
Vapor
Liquid
C) Stratified
Vapor
Liquid
B) Slug (Back interface)
Liquid
Vapor
D) Bubbly/Slug
100 μm
Vapor
Liquid

Figure 2.10 Examples of the dominant flow regimes observed during diabatic operation with the black arrow indicating direction of liquid flow. A) Bubbly flow is typically observed at very low mass qualities <1%. B) Slug type flows are also only observed at low qualities and have a distinctive asymmetric shape due to the hydrophobicity of the membrane. C) Stratified flows are dominant at intermediate qualities up to 10% with cyclical wetting-stratified-dryout behavior observed at G = 140 kg/s-m^2 and qualities > 4%. D) At the higher mass flux of 340 kg/s-m^2 and at low qualities larger bubbles are observed forming on the membrane, then coalescing to form stratified and slug flows.

The cycle begins with wetting liquid rivulets and drops flowing not just on the copper surface but on the plastic and membrane surfaces as well (Figure 2.11.A). This initial period is then followed by a short period of churning annular type flow (Figure 2.11.B) with a vapor core surrounded by a liquid film. The thin liquid film in contact with the membrane breaks up, with the liquid beading up to leave distinct liquid droplets on the surface of the membrane (Figure 2.11.C), and liquid films on the wetting surfaces that evaporate over time. Several more periods of this churning annular slugs (as many as a dozen) follow, both removing and leaving new droplets on the membrane and replenishing the liquid films, until eventually a long dry-out period is achieved (Figure 2.11.D) during which the thin films almost completely evaporate.

The entire cycle then repeats as liquid upstream overcomes the increased pressure in the channel due to vaporization and rewets the channel. The liquid droplets, depending on the size, number and contact with the copper and plastic wetting surfaces, either remain on the membrane until the next cycle or coalesce to form larger drops that are then pushed out. At the highest tested quality of 20% the cycles were found to last between 0.02 and 0.1 seconds in duration.

A diabatic flow regime map for the data is shown in Figure 2.12. The low quality flow regimes of bubbly, slug and plug type flows are not included because they cannot be accurately associated with a particular quality due to lack of spatial data. Comparing with the adiabatic visualization and data points plotted in Figure 2.12, we see that in the diabatic case the wavy, wavy-stratified, corner-wedge or smooth annular flows are not observed. Hetsroni *et al.* [72] and more recently Harirchian and Garimella [73] provide visualization of the different types of diabatic flow regimes encountered in two-phase water and refrigerant flow in microchannels. Harirchian and Garimella [74] and Revellin and Thome [75] also develop new transition criteria, using refrigerant data, to describe the changes in flow regime with the Bond number (Bo), Boiling number (Boi), Reynolds number (Re) and Weber number (We), which together capture the effect of inertia, heat flux and confinement effects in the microchannels.

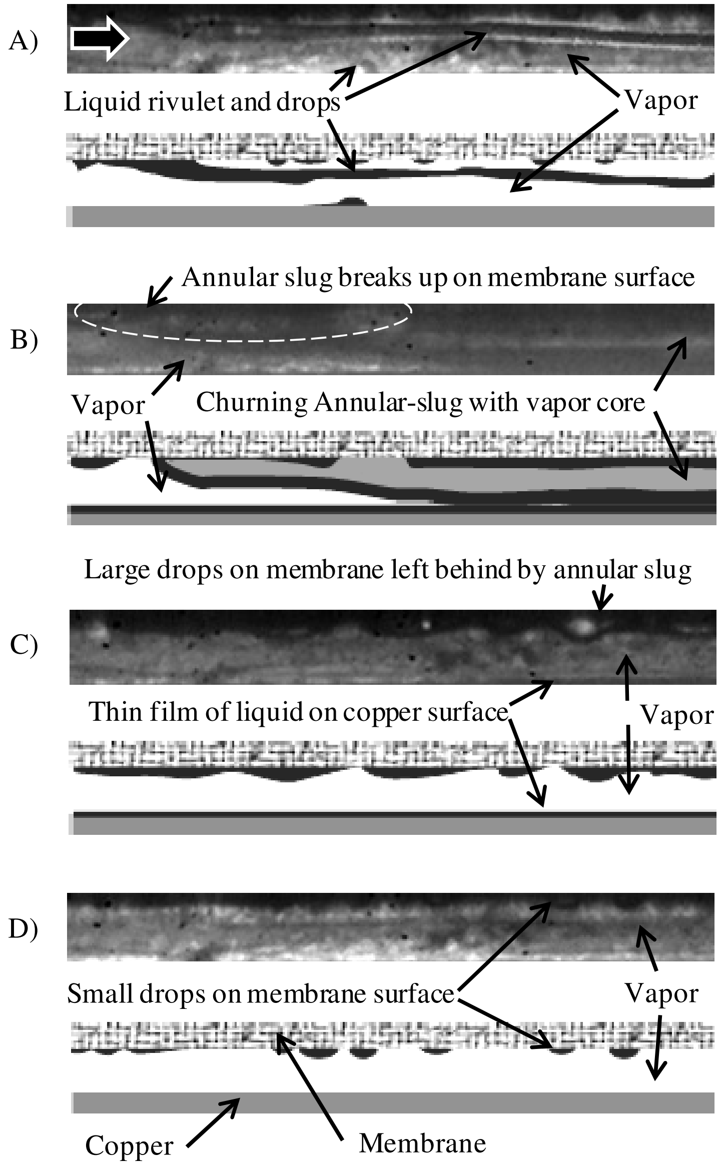
A)
Liquid rivulet and drops
Vapor
B)
Annular slug breaks up on membrane surface
Vapor
Churning Annular-slug with vapor core
C)
Large drops on membrane left behind by annular slug
Thin film of liquid on copper surface
Vapor
D)
Small drops on membrane surface
Vapor
Copper
Membrane

Figure 2.11 Sequence of images at various times during cyclical churn-annular flow that is observed only at the higher mass flux of 340 kg/s-m^2 and at qualities > 10%. Schematics are drawn directly from the images and are included for clarity. Initial wetting by liquid rivulets occurs on the various surfaces (A) followed by several churning annular slugs (B). These churning annular structures appear to breakup on the membrane surface leaving behind large droplets (C) most of which coalesce and are pushed out leaving behind smaller drops during the dry-out phase when the thin liquid films on the wetting surfaces evaporate (D). The entire cycle then repeats and found to vary from 0.02s to 0.1s (f ~ 10 to 50 Hz).

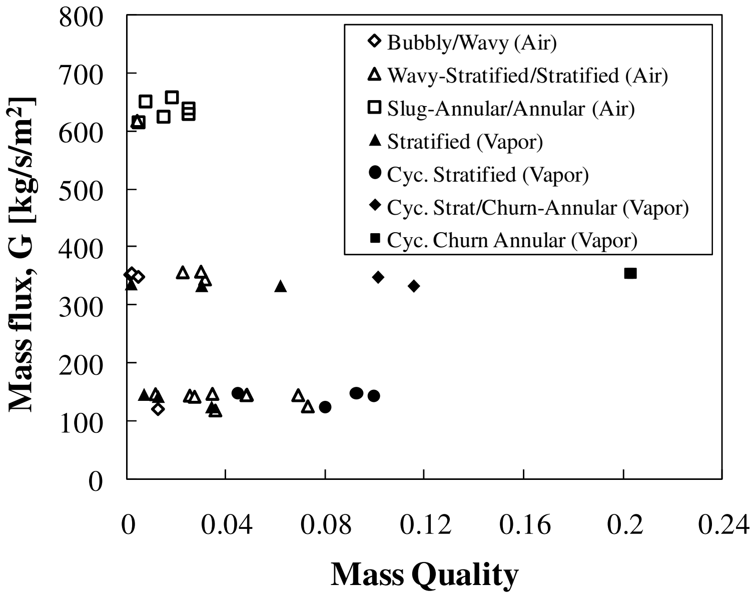

Figure 2.12 Diabatic flow regime map with mass flux plotted against the quality for the vapor separation microchannel at the two tested mass fluxes. At G = 140 kg/s-m^2 stratified and then cyclical stratified flows are observed and at G = 340 kg/s-m^2, stratified type flows give way to a cyclical mixed stratified and churning-annular type flow which then leads to cyclical churn-annular type flows at higher qualities. In general the flows at the higher mass flux were more chaotic.

Figure 2.13 shows our data plotted on the flow regime map proposed by Harirchian and Garimella along with their transition criteria. Below the line, they found the flow was primarily confined slug flow and above the line, churn and confined annular type flows. Their prediction of churning annular flow is consistent with our data. Below the transition line we find stratified flow to be dominant along with both bubbly and slug flows at very low qualities. The existence of stratified flow and bubbly flow is not surprising as the hydrophobic membrane encourages the confined vapor slugs to spread out and ‘wet’ the membrane, forming bubbly flow at low qualities and stratified flows at higher qualities.

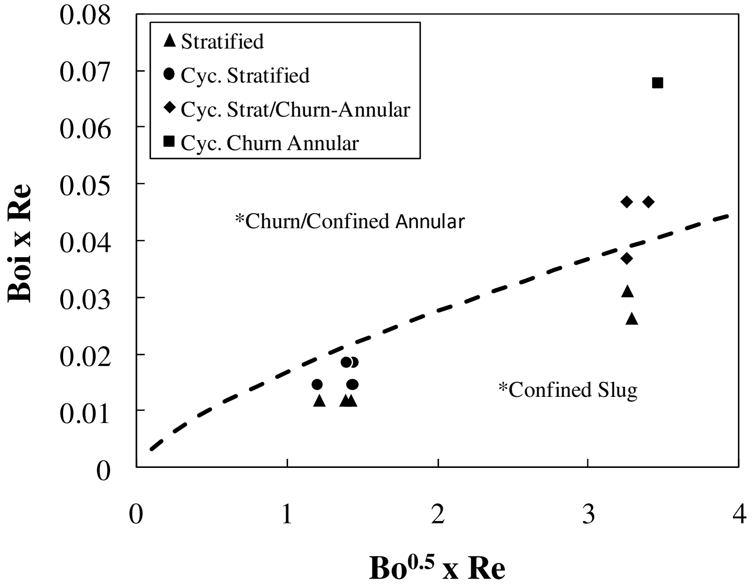

Figure 2.13 Flow map and transition criteria as proposed by Harirchian and Garimella [74]. The y-axis is the product of the Boiling number (Boi) and the Reynold's number (Re) and the x-axis the product of the square root of the Bond number (Bo) and Re. Harirchian and Garimella's reported flow regimes is included (*) for comparison. The curve indicates when slug type flows become churn/annular in nature. The transition criteria developed predicts the churn type flows seen in our device, but the predicted slug type flows are manifested as stratified flow in our device due to the hydrophobicity of the membrane.

2.3.2.2 Impact of flow-regime on pressure drop and heat transfer

The observed diabatic flow regimes are expected to impact both the pressure drop and heat transfer coefficients in the channel. Annular flow is typical for boiling flows in microchannels and enjoys a high heat transfer coefficient due to the evaporation of the thin films on the walls of the channel. In the vapor venting device at low mass fluxes, stratified flow is dominant. Stratified flow has a single thicker evaporating film, with a maximum observed thickness of around 60-80μm. Assuming the heat transfer is dominated by thin film evaporation, the comparatively thicker evaporating film would result in a poorer heat transfer coefficient. At higher mass fluxes however, the flow regime in the venting device transitions to a churning-annular type flow similar to what would be experienced in a typical non-venting microchannel. The maximum film thicknesses on the heated copper surface for this flow regime is observed to only be around 10-30μm. The thinner films are expected to result in higher heat transfer coefficients as compared to a stratified flow case.

Analytical modeling of the pressure drop for stratified and smooth annular flow using techniques outlined by Carey [76] and Tong and Tang [26] doesn't result in a significant difference in the total pressure drop. However, in the churning-annular case, the flow is more chaotic with the liquid films breaking up on the membrane surface and flowing as droplets. Droplet flow on a hydrophobic surface could potentially result in lowered pressure drops, though further analysis is needed.

2.4 Summary and Conclusion

In the work presented in this chapter we have developed and tested a single microchannel copper device that allows visualization of venting flow structures when using a porous hydrophobic Teflon membrane and porous carbon-mesh membrane. Phase separation and removal through the membranes was studied both adiabatically and diabatically by injecting air through a T-junction and by heating until vaporization respectively. Mass qualities of 0.1% to 7% were achieved in the adiabatic experiments and up to 20% during diabatic experiments. The flow regimes obtained in each was visualized, mapped and compared to key work in the field highlighting the differences in observed flow structures when a hydrophobic membrane is incorporated.

In adiabatic experiments we find bubbly flows at low qualities, changing to wavy stratified and smooth stratified as air injection rates increase. At higher liquid flow-rates the behavior changes resulting in 'jetting' type breakup and the formation of annular type flows that are not conducive to air venting. During diabatic operation we find bubbly and slug type flows at low qualities followed by stratified and cyclical stratified flows at higher qualities and low liquid flow rates. As the flow rate is increased we see churn-annular type flows forming at higher qualities. The occurrence of churn-annular type flows is expected to help improve heat transfer coefficients and potentially the two-phase pressure drops.

Analysis of the venting rates during adiabatic operation finds that the maximum quality the device can support before maximizing its venting effectiveness can be improved by adding an outlet choke, reducing vent-side pressure, increasing the membrane-channel area and using thin membranes with higher permeabilities. We also find that venting effectiveness doesn’t depend on the Weber number as long as the air-structures interact with the membrane.

The work presented in this chapter represents an important step in the design of a gas and vapor venting devices, particularly vapor venting heat exchangers, by generating a preliminary flow-regime map for a phase separated two-phase flows and experimentally identifying several factors that help improve venting effectiveness. The work also highlights the potential importance of flow regime in altering the heat transfer and pressure drop in a microchannel.

CHAPTER 3 MODELING AND PARAMETRIC ANALYSIS OF TWO-PHASE VAPOR VENTING FLOW IN HEAT EXCHANGERS

3.1 Motivation and Overview

This chapter describes the development and application of a microchannel two-phase flow model that incorporates local vapor removal through a membrane and mating vent microchannel. A parametric analysis using the developed model is useful to gain an understanding of the factors that influence the performance of the vapor venting heat exchanger and how that performance could potentially be improved. The base correlations used in the model are obtained from experimental data obtained from a non-venting control device described in Chapter 4. A comparison of the simulation and experimental results for a vapor venting device are also detailed there. This chapter focuses on the impact of conductive spreading, membrane conductance, channel density and fin thickness, liquid and vent channel hydraulic diameter and liquid-to-vent channel hydraulic diameter ratio on the pressure drop and substrate temperature. To determine under what conditions a venting device provides superior performance we compare the performance of a vapor venting heat exchanger against: i) a non-venting control with a liquid channel of the same diameter as that in the venting device and, ii) a volumetrically equivalent, non-venting heat exchanger that occupies the same total volume as the vapor venting heat exchanger. Details of the model are described in the following three sections with simulation parameters and geometries described in Section 3.5. Results of the parametric analysis can be found in Section 3.6.

3.2 Description of the Computational Domain and Solution Techniques

Figure 3.1 highlights the computational element and the key boundary conditions used in the two-phase venting model discussed in this chapter. This element is assumed to be an interior element in the device and does not consider the impact of the edges of the device. Region A, B and C are solved separately (only A and C in the case of non-venting microchannel) and then matched at the boundaries. The three regions are solved using three nested iterative loops to reach the final solution for the domain as a whole.

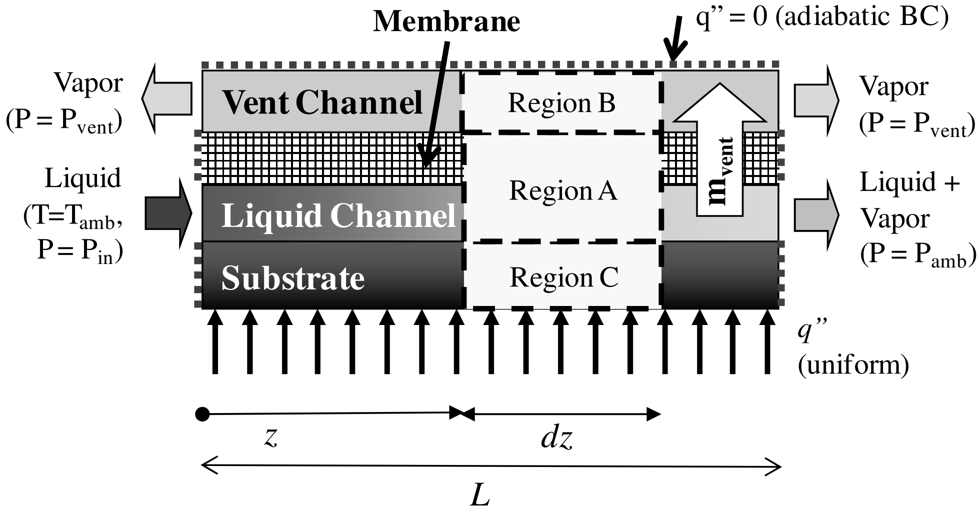

Figure 3.1 Schematic of computational element used in simulations presented in this study. External boundary conditions are presented. Region A: 1D two-phase flow in the microchannels with heat flux provided by solution of Region C. Also considers single-phase flow in the membrane based on pressure profile in liquid and vent channels, the latter obtained from the solution to Region B. Region B: 1D single-phase vapor flow in vent channel with vapor injection provided from solution to Region A. Region C: 2D solid conduction in substrate with convective boundary condition on top surface provided by solution of Region A.

Region A deals with 1D two-phase flow in the microchannel. A marching technique is used to solve for the pressure, fluid temperature, vapor mass quality, mass-loss due to venting, fin efficiency and heat transfer coefficients along the length of the channel. At the inlet, the liquid flow-rate, temperature and thermodynamic quality is specified while at the outlet, the pressure, typically 101kPa, is specified.

Along the bottom length of the channel the wall heat flux is specified and along the top length of the membrane, the vent side pressure is specified. Region A is solved iteratively by guessing the inlet pressure and solving for the outlet pressure until the simulated outlet pressure is within 1% of the specified outlet pressure. Initially, both the input heat-fluxes and vent side pressure are applied as given but subsequent iterations use the pressure and heat-flux output from Region B and C as corrected inputs in the solution for Region A. Since fluid properties can change quite significantly with pressure and temperature, a MATLAB based steam-table [77] as well as several property tables are used to calculate the new fluid properties at each step. The impact of the square cross-section is captured using the hydraulic diameter approximation as well as the appropriate friction factor. Similarly, we use single phase and two-phase heat transfer relations developed for pipe flow. Due to the typically lower thermal conductivity of the capping material (e.g. silicone film, PTFE membrane) we assume that only three of the four walls participates in heat transfer and make the Nusselt number correction to the heat transfer coefficients as described in Qu and Mudawar [21]. Another key assumption in the model is that the momentum and energy relations and correlations developed for pipe flow remain valid despite asymmetric suction. Analytical relations for asymmetric suction of the kind that could be incorporated into the current model are not currently available with even *symmetric* suction problems requiring perturbation, numerical or power-series type solutions of the fourth-order non-linear ODE for the momentum [78].

We also consider flow in the membrane within the solver for Region A and treat the flow as being 1D, single-phase and Darcy in nature. Since the thickness of the membrane is more than two orders of magnitude smaller than the length of the membrane along the channel, the flow in the membrane is assumed to be 1D and normal to flow in the channels. We assume that only vapor flows through the membrane and that there is no entrained liquid mass in the venting vapor. We also assume that due to the high temperature of the surrounding substrate and the membrane, the rate of condensation of the venting vapor within the membrane is negligible, thus resulting in single-phase vapor flow in the membrane. Due to the low maximum Reynolds number of 0.1 and a Knudsen number < 1 for the steam flow through a typical micron pore sized membrane that we are considering in this work, we ignore any non-linear inertial and molecular flow effects [79]. Given these assumptions the pressure drop across the membrane can be described by the Darcy equation for viscous flow in porous media, Eq. (3.1), where G is the mass flux velocity, κ the intrinsic permeability and t_{mem} the membrane thickness.

$$\Delta P_{mem} = G_{mem} \cdot \frac{\mu_v}{\rho_v} \cdot \left(\frac{1}{\kappa} \cdot \frac{1}{t_{mem}} \right) \tag{3.1}$$

Due to the large pressure difference that can exist across the membrane, the density of the vapor in the membrane is taken to be an average of what it would be on either side of the membrane. Though pressure drop in the liquid- and vent-side manifolds can be neglected due to their large hydraulic diameter, venting from the outlet manifold can be significant and is included in the model.

Region B evaluates 1D, adiabatic, single-phase vapor flow in the vent channel with a mass-flow boundary condition at the interface with Region A and pressure boundary conditions at either end of the vent channels. Averaged fluid properties are used since neither temperature nor pressure are expected to change significantly in the vent channel for our simulation and experimental conditions. We assume flow in the vent channel to be single-phase vapor and adiabatic due to the small convective heat transfer coefficient and temperature difference (confirmed via experiments) during vapor flow. Similar to Region A, we again assume fully developed pipe-flow pressure drop relations are applicable with mass influx from the liquid channel treated as variable mass flux along the length of the vent channel. Region B is solved immediately following Region A and both A and B are run in a loop until the pressure profile on the vent side converges.

Region C deals with 2D conduction in the substrate and is solved using a 2D central-discretized scheme with constant material properties to obtain heat flux at the top surface and substrate temperatures. The heat flux boundary condition at the bottom of the substrate is set by the user and for the current work is assumed to be uniform. The sides are assumed to be adiabatic since the total free convective resistance is much larger than the forced convection thermal resistance in the channels. We also assume that there is no conduction from the lower liquid-channel containing substrate to the vent-channel containing capping substrate. This is because steady state heat flow is expected to be small since the top substrate is assumed to be well insulated and heat flow to the vapor is minimal. The top surface of region C is a convection boundary condition where the heat transfer coefficient and fluid temperature are inputs from the solution of Region A. With the given boundary conditions the new heat input profile at the channel walls can be calculated and used as an input for re-solving Region A+B. Region C and Region A+B are solved in a loop until convergence.

The simulation results as a whole were confirmed against analytical models (single-phase momentum and energy conservation, two-phase energy conservation) and alternate numerical models (two-phase momentum conservation) to confirm the validity of the model. In single-phase, the results matched to within 1% and during two-phase flow the pressure drop matched to within 5%when using a 100µm grid. Better accuracy during two-phase flow can be achieved by using a smaller grid at the expense of computation time. In the current work, the grid size is set to 50µm for most cases. The large pressure drops that arise when simulating flow in 50µm diameter channels result in computation errors when a grid of 50µm is used, thus requiring a smaller 25µm grid.

3.3 Pressure Drop Models

Single-phase liquid and vapor flow in the liquid channel and single-phase vapor flow in the vent channel is modeled using standard Poiseuille flow, Eq. (3.2), with the laminar fanning friction factor, f, given by Eq. (3.3) for a rectangular channel [80]. G is the mass flux velocity, d the depth of the channel and w the width of the flow channel.

$$\left(\frac{dP}{dz}\right)_{sp} = -\frac{2 \cdot f \cdot G^2}{\rho \cdot D_h} \tag{3.2}$$

$$f = \frac{24}{\mathrm{Re}}\left(1 - \frac{1.3553}{AR} + \frac{1.9467}{AR^2} - \frac{1.7012}{AR^3} + \frac{0.9564}{AR^4} - \frac{0.2537}{AR^5}\right) \tag{3.3}$$

$$AR = d / w$$

The two-phase pressure drop can be modeled in four distinct ways: homogenous model, separated-flow model, two-fluid model and phenomenological models. The two-fluid and phenomenological models, though more accurate, are more complex to solve and in the case of the phenomenological models is specific to certain flow regimes. The homogenous model [25], given by Eq. (3.4), is the simplest of the two-phase models and treats the two-phase flow as a 'single' phase with quality, x, averaged fluid density and viscosity, Eq. (3.5), and an effective friction factor Eq. (3.6), where B is a constant.

$$\left(\frac{dP}{dz}\right)_{tp\ friction,HEM} = -\frac{2 \cdot f_{tp} \cdot G^2}{\rho_{tp} \cdot D_h} \tag{3.4}$$

$$\begin{gathered} \frac{1}{\rho_{tp}} = \frac{x}{\rho_v} + \frac{1-x}{\rho_l} \\ \frac{1}{\mu_{tp}} = \frac{x}{\mu_v} + \frac{1-x}{\mu_l} \end{gathered} \tag{3.5}$$

$$f_{tp} = B \cdot \mathrm{Re}_{tp}^{-1} = B \cdot \left(\frac{G \cdot D_h}{\mu_{tp}}\right)^{-1} \tag{3.6}$$

The key assumption in the homogenous model is that the vapor and liquid phases are traveling at the same velocity. The homogenous equilibrium model is often considered to be poor at predicting two-phase pressure drops, particularly in microchannels where bubbly type flow, for which this model is most appropriate, is rarely encountered. However, experimental work by Zhang *et al.* [81] found good agreement with this model suggesting that it may still be applicable at the microscale.

The separated flow model for a horizontal channel [25], given by Eq. (3.7) and originally developed by Lockhart and Martinelli for adiabatic air-water flows, allows for different velocities in the liquid and vapor phase. However, unlike the homogenous model, this model requires correlations for the two-phase multiplier, φ_l, in the frictional component (1st term on the right) and for the void-fraction, ε, in the accelerative component (2nd term on the right). The Zivi void fraction correlation, Eq. (3.8), is widely used for ε and is derived from an energy analysis approach [82]. Lockhart and Martinelli developed a graphical correlation relating the two-phase multiplier with the Martinelli parameter. Chisholm *et al.* [25] then presented this graphical correlation mathematically as shown by Eq. (3.9) where C is the Chisholm parameter and X is the Martinelli parameter, given by Eq. (3.10).

$$\left(\frac{dP}{dz}\right)_{tp,SFM} = -\phi_l^2 \cdot \left(\frac{dP}{dz}\right)_l + \frac{d}{dz}\left(\frac{G^2 \cdot x^2}{\rho_v \cdot \varepsilon} + \frac{G^2 \cdot (1-x)^2}{\rho_l \cdot (1-\varepsilon)}\right) \tag{3.7}$$

$$\varepsilon = \left(1 + \frac{(1-x)}{x} \cdot \left(\frac{\rho_v}{\rho_l}\right)^{2/3}\right)^{-1} \tag{3.8}$$

$$\phi_l^2 = \left(1 + \frac{C}{\mathrm{X}} + \frac{1}{\mathrm{X}^2}\right) \tag{3.9}$$

$$\mathrm{X}^2 = \frac{\left(dP/dz\right)_l}{\left(dP/dz\right)_v} = \frac{\left(\dfrac{2 \cdot f_l \cdot G^2 \cdot (1-x)^2}{\rho_l \cdot D_h}\right)}{\left(\dfrac{2 \cdot f_v \cdot G^2 \cdot x^2}{\rho_v \cdot D_h}\right)} = \frac{f_l}{f_v} \cdot \frac{\rho_v}{\rho_l} \cdot \left(\frac{1-x}{x}\right)^2 \tag{3.10}$$

(for laminar liquid-laminar vapor flow)

An alternate form of the frictional component of the two-phase pressure drop equation is given by Eq. (3.11) where the two-phase pressure drop is a serial sum of the pressure drop due to the liquid flow, the pressure drop due to the vapor flow and an additional pressure drop due to the interaction of the phases. Thus the Chisholm parameter C is a measure of the interaction of the phases.

$$-\left(\frac{dP}{dz}\right)_{tp,SFM} = \left(\frac{dP}{dz}\right)_l + \left(\frac{dP}{dz}\right)_v + C \cdot \left(\frac{dP}{dz}\right)_l^{0.5} \cdot \left(\frac{dP}{dz}\right)_v^{0.5} \tag{3.11}$$

In Lockhart and Martinelli's work the value for C was found to be 5, 10, 12 and 20 when the liquid and vapor phases were laminar-laminar, laminar-turbulent, turbulent-laminar and turbulent-turbulent. The separated flow model has had wide use in the modeling of two-phase flow at the macroscale and microscale with authors modifying C to capture additional effects. References [83-85] provide recent reviews on previous correlations for two-phase flow in microchannels.

In order to predict the pressure-drop during venting using our model it is first necessary to determine the correct form of the two-phase pressure drop equation through comparison with non-venting two-phase data. This data was obtained using the setup and procedure discussed in Chapter 4. We compared control data obtained for 2 ml/min against four models with the results shown in Figure 3.2:

i) Homogenous equilibrium model given by Eq. (3.4),

ii) Lockhart and Martinelli separated flow model, Eqs. (3.7) to (3.10), with $C = 5$ since our liquid and vapor phases are always laminar

iii) Mishima and Hibiki [86] separated flow model with $C = 21\cdot(1\text{-}\exp(-319\cdot D_h))$

iv) HJ Lee *et al.* [83] separated flow model with $C = 121.6\cdot(1\text{-}\exp(-22.7\cdot Bo))x_e^{1.85}$.

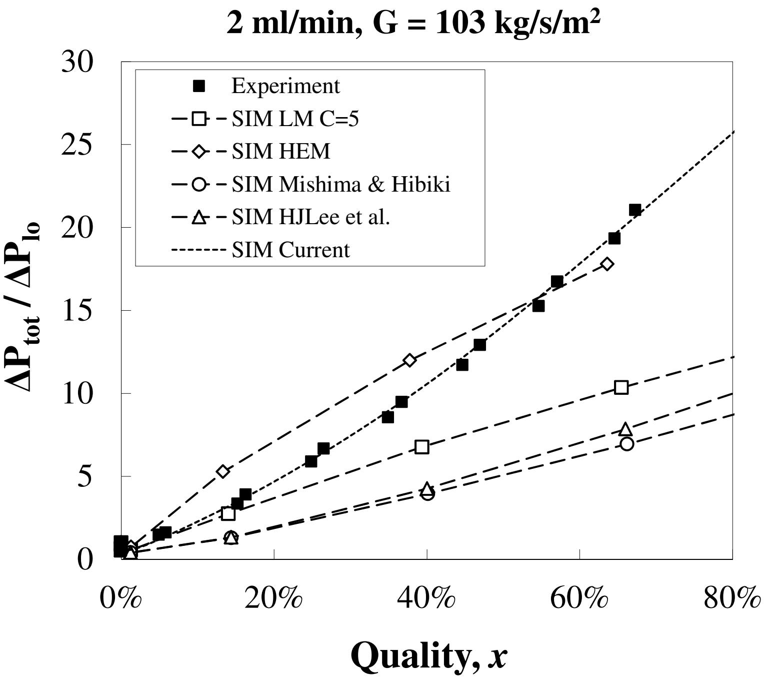

Figure 3.2 Comparison of experimental liquid-only (lo) normalized two-phase pressure drop versus vapor quality data against four available correlations: Lockhart and Martinelli (LM) separated flow correlation with C = 5, homogenous equilibrium model (HEM), separated flow correlation by Mishima and Hibiki [86], separated flow correlation by HJ Lee *et al.* [83]. Exp. data falls mostly between LM and HEM models but agrees better in trend with the correlation by HJ Lee *et al.* Correlation developed in this study is given by Eq. (3.12).

As shown in Figure 3.2, the experimental normalized pressure drop (two-phase pressure drop / liquid-only pressure drop) versus the vapor quality falls mostly between the values predicted by the Lockhart and Martinelli separated flow model and the homogenous equilibrium flow model. However, the trend in the data is similar to the model proposed by HJ Lee *et al.* Modifying their model we obtain a new correlation for the pressure drop with the Chisholm parameter given by Eq. (3.12). This correlation agrees well with our experimental data, suggesting that the Chisholm parameter does have the same power relationship with the vapor quality as proposed by HJ Lee *et al.* They suggest that the reason behind this dependence is the increased velocity ratio and thus interaction between the phases as quality increases; however a more detailed study on the physical nature of this dependence is required.

$$C = 1.84 \cdot \mathrm{Re}_{lo}^{0.3} + 2.5 \cdot \mathrm{Re}_{lo} \cdot x^{1.85}$$

$$\mathrm{Re}_{lo} = \frac{G \cdot D_h}{\mu_f} \tag{3.12}$$

The Bond number dependence was not included in our model as we did not experimentally study other hydraulic diameter channels or alternate working fluids. However, experimental data at higher flow rates of 4 ml/min, 6 ml/min and 8 ml/min suggests that the Chisholm parameter is increasing with the flow velocity. Qu and Mudawar [87] and Lee and Garimella [85] also find a dependence on the velocity though the relationships are different. In this work we chose to use the *Re* number as the dimensionless parameter to capture the flow velocity dependence, however the *We* or *Ca* numbers could also be used. Further work is necessary before the most appropriate dimensionless quantity to capture the flow-velocity dependence can be confirmed.

3.4 Convective Heat Transfer Models

The single-phase fully developed heat transfer coefficients for the liquid and vapor are modeled using Eq. (3.13) where a Nusselt number of 2.98 was used [88]. This Nusselt number represents constant wall temperature in a square channel since the default substrate being simulated is copper. The validity of this is confirmed in Section 3.5. We also calculate local fin efficiency based on the local heat transfer coefficient to determine the fraction of exposed area participating in heat transfer. The fin efficiency is determined in our flow model (Region A) and is input as a boundary condition in the conduction solver (Region C). Since the thermal entry length can make up a significant portion of the flow length we model the single-phase thermally developing heat transfer coefficient using Eq. (3.14). The first three eigenvalues and constants from Kays and Crawford [88] for the series solution are listed.

$$h_{sp,fd} = \frac{Nu_m \cdot k}{D_h}$$

$$Nu_m = 2.98 \qquad (3.13)$$

$$Nu_m = \frac{1}{2z^+} \ln\left[\frac{1}{8 \cdot \sum_{n=0}^{\infty} \left(E_n / \lambda_n^2\right) \exp\left(-\lambda_n^2 \cdot z^+\right)}\right] \qquad (3.14)$$

$$\lambda_n^2 = [5.96 \quad 35.64 \quad 78.9]$$
$$E_n = [0.598 \quad 0.462 \quad 0.138]$$

Several empirical correlations for the two-phase heat transfer coefficients now exist in the literature for a variety of experimental conditions. To determine the correct two-phase heat transfer relationship for our simulations we compared the experimental data against two widely used models. The model proposed by Kandlikar and Balasubramanian [89] is given by Eq. (3.15) and the model proposed by Lee and Mudawar [90] by Eq. (3.16). These correlations were chosen because the experimental conditions used in the development of these correlations were the closest to our own.

$$h_{tp,NBD} = \left(0.6683 \cdot Co^{-0.2} + 1058 \cdot Boi^{0.7} \cdot F_n\right) \cdot (1 - x_e)^{0.8} \cdot h_{sp,fd}$$

$$Co = \left(\frac{1 - x_e}{x_e}\right)^{0.8} \left(\frac{\rho_v}{\rho_l}\right)^{0.5} \qquad (3.15)$$

$$Boi = \frac{q''}{G \cdot \Delta H_{lv}}$$

$F_n = 1$ (for water)

$$h_{tp} = 3.856 \cdot \mathrm{X}^{0.267} \cdot h_{sp,fd} \qquad 0 < \mathrm{x} \leq 0.05$$

$$h_{tp} = 436.48 \cdot Boi^{0.522} \cdot We_{lo}^{0.351} \cdot \mathrm{X}^{0.665} \cdot h_{sp,fd} \qquad 0.05 < \mathrm{x} \leq 0.55 \tag{3.16}$$

$$We_{lo} = \frac{G^2 \cdot D_h}{\rho_l \cdot \sigma}$$

The results of the comparison are shown in Figure 3.3 with our data falling between the two tested models for most of the quality range. Similar to Lee and Mudawar we developed a correlation that fits our data based on the Martinelli parameter, *X*. The new correlation is given by Eq. (3.17) and matches the experimental data at all flow-rates with a mean approximate error of 13%.

$$h_{tp} = 20 \cdot \mathrm{X} \cdot h_{sp,fd} \tag{3.17}$$

The heat transfer coefficient data collected at different input heat-fluxes and mass fluxes were found to collapse to a single curve when plotted against the vapor quality, suggesting little dependence of the heat transfer coefficient on either the heat-flux or mass-flux. Agostini and Thome [91] in their review find similar behavior in the literature though it is typically only observed for high quality flows of over 50%.

The reducing heat transfer coefficient with quality can be explained using the three-zone model developed by Thome *et al.* [71]. The three zones are composed of a liquid slug that wets the channel walls, an annular region where heat transfer occurs through evaporation of the thin film of liquid and finally a dry-out region with a poor heat transfer coefficient when all the liquid has evaporated. The heat transfer coefficient at a particular location is given by the temporal average of the heat transfer coefficient for each of these three flow regimes. In our case, we believe that the heat transfer reaches a maximum at some quality < 5% and then monotonically reduces with quality because the fraction of time spent in ‘dry-out’ versus annular thin film evaporation increases with quality.

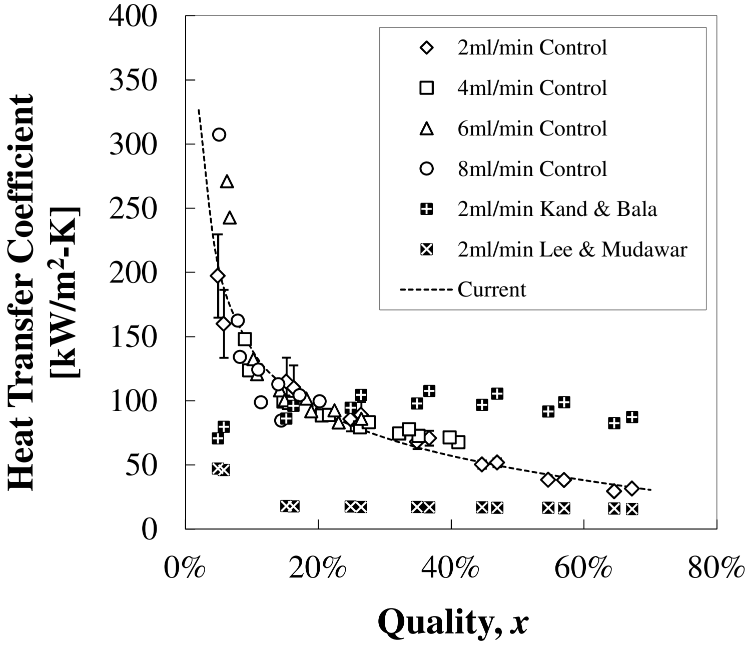

Figure 3.3 Comparison of experimental data against two widely used heat transfer coefficient correlations proposed by Kandlikar and Balasubramanian [89] and Lee and Mudawar [90]. Data at all flow-rates was found to be well correlated by Eq. (3.17).

3.5 Description of the Simulated Heat Sink

The three types of heat sinks that are simulated and compared are shown in Figure 3.4 along with a list of the default conditions for the channels, membrane and flow in Table 3.1.

The geometric constraints were chosen based on the typical dimensions studied in the two-phase literature and manufacturability in substrates such as copper. The heat flux is typical for current high power microprocessors. Water was chosen as the working fluid due to its superior thermal properties as compared to refrigerants and dielectric fluids and also due to the need to confirm the models with experiments, which were carried out using water. The default membrane properties were chosen based on a widely available porous hydrophobic PTFE membrane with 220nm pores that is used in our experimental work (see Chapters 2 and 4) due to its high selectivity and thermal stability.

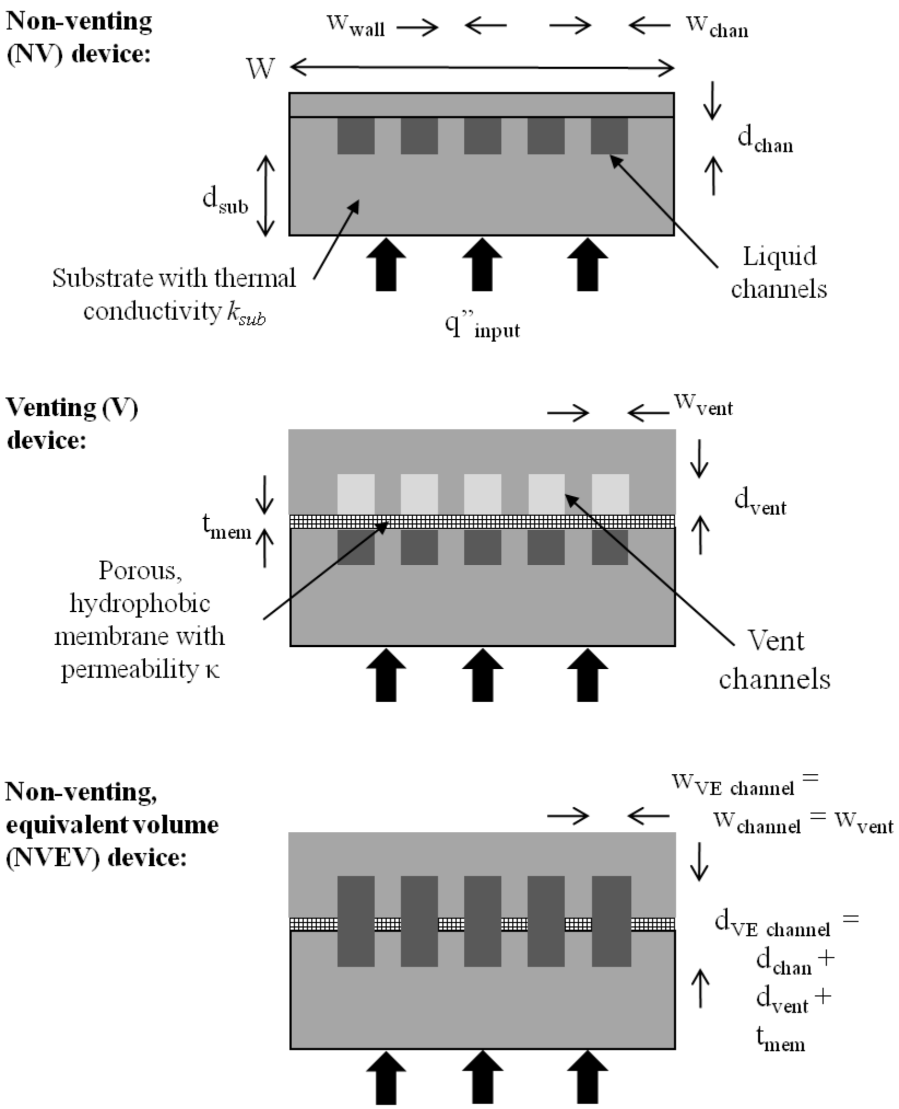
Non-venting (NV) device:
w_{wall}
w_{chan}
W
d_{chan}
d_{sub}
Substrate with thermal conductivity k_{sub}
Liquid channels
q''_{input}
Venting (V) device:
w_{vent}
d_{vent}
t_{mem}
Porous, hydrophobic membrane with permeability κ
Vent channels
Non-venting, equivalent volume (NVEV) device:
$w_{VE\ channel} = w_{channel} = w_{vent}$
$d_{VE\ channel} = d_{chan} + d_{vent} + t_{mem}$

Figure 3.4 Schematics of the three different types of device configurations that were simulated. The NVEV device is designed to occupy the same total volume as the venting device with a comparatively larger liquid channel while the non-venting device has the same liquid channel hydraulic diameter as the venting device.

Table 3.1 List of default test conditions

Item	Quantity
Working Fluid	Water
Substrate Conductivity, k_{sub}	400 W/m-K
Substrate thickness, d_{sub}	2.4 mm
Input Heat Flux, q''_{input}	100 W/cm^2
Flow Rate, f	5 ml/min, 0.083 g/s
Liquid inlet temperature, T_{amb}	25 C
Liquid outlet pressure, $P_{o,}$ P_{amb}	101 kPa
Vent outlet pressure, P_{vent}	101 kPa
Device length / Channel length, L	10 mm
Device Width, W	10 mm
Liquid channel height, d_{chan}	100 µm
Liquid channel width, w_{chan}	100 µm
Vent channel height, d_{vent}	100 µm
Vent channel width, w_{vent}	100 µm
Wall width / Fin thickness, w_{wall}	100 µm
Membrane permeability, κ	5e-15 m^2
Membrane thickness, t_{mem}	65 µm

3.6 Simulation Results and Discussion

3.6.1 Impact of Substrate Spreading during Single Phase Flow

One of the key questions during the development of the two-phase model is the validity of the constant channel wall heat flux boundary condition and the need to include substrate conduction. This constant heat flux boundary condition is sometimes incorrectly assumed in the literature when developing two-phase correlations; however, the validity of this assumption is dependent on the substrate thermal conductivity and thickness as well as the convective caloric resistance. It is also necessary to verify the wall boundary condition to determine if the default Nusselt number of 2.98 is valid for the simulation conditions when using a 2.4mm thick copper substrate. To consider the importance of heat spreading, we first considered the impact of varying the substrate conductivity and thickness, collectively the axial thermal resistance $R_{ax} = L/(k_{sub}*d_{sub}*W)$, on the pressure drop, fluid and substrate temperature and channel wall heat flux during single phase flow. To maintain single phase flow we increased the flow rate from 5 ml/min to 10 ml/min and reduced the heat flux to 50 W/cm^2.

Figure 3.5 shows the spatial variation of wall heat flux, pressure, fluid and substrate temperatures with the axial thermal resistance. We find that for the case of a highly resistive substrate such as thin films of silicon or glass, the wall condition approaches the ideal 'constant heat flux' boundary condition. At the other end of the spectrum, the use of thick, highly conductive substrates leads to a constant wall temperature boundary condition. For silicon and copper substrates of thicknesses commonly encountered in the literature the wall condition lies between that of a constant heat flux and constant temperature boundary condition and for 2.4mm thick copper with an axial R_{th} ~ 1 C/W, is closer to constant wall temperature than constant heat flux boundary condition.

Interestingly, spreading leads to variations in the pressure drop with increased spreading leading to lower single phase pressure drops. This is due to warmer, less viscous fluid flowing for a comparatively longer fraction of the channel length than in the constant heat flux case. The substrate temperature has a more complex relationship since it is dependent on the transverse thermal resistance and the fluid temperature. This is made clear in Figure 3.6 where we compare the substrate temperature against the average Biot number with the thickness of the substrate chosen as the characteristic length scale. For Biot numbers less than 0.1 the temperature of the substrate is dominated by convection, and since greater spreading increases the average fluid temperature, the substrate temperature increases with reducing axial thermal resistance. After a Biot number of 0.1 however, conduction begins to dominate and the substrate temperature increases with transverse thermal resistance. Thus the lowest substrate temperature is obtained at around Biot ~ 0.1 where the dependence switches from convection to conduction.

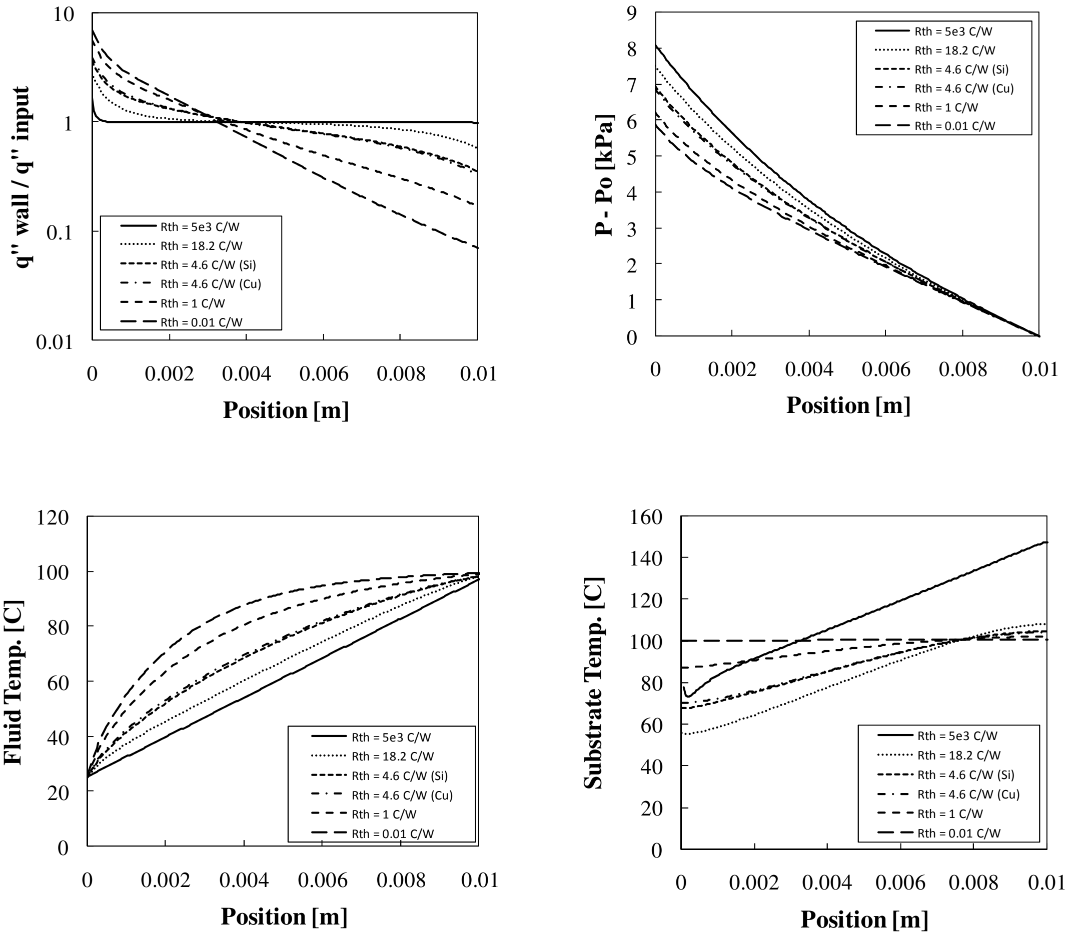

Figure 3.5 Simulated input power normalized channel wall heat flux (top left), pressure drop (top right), fluid temperature (bottom left) and mean substrate temperature (bottom right) along the length of a 1cm long, 100μm x 100μm channel, dissipating 50 W/cm^2 heat flux, and experiencing single phase liquid flow. Several substrate thickness and conductivities were simulated, combined as R_{th}, the axial thermal resistance. The highest R_{th}, indicative of low thermal conductivity thin substrates, leads to a constant wall heat flux like boundary condition while low R_{th} leads to constant wall temperature like boundary condition. Pressure drop reduces with R_{th} due to increased fluid preheating. Simulations were carried out using conjugate conduction-convection finite difference model with laminar friction factor pressure drop and developing Nusselt number relations for the heat transfer.

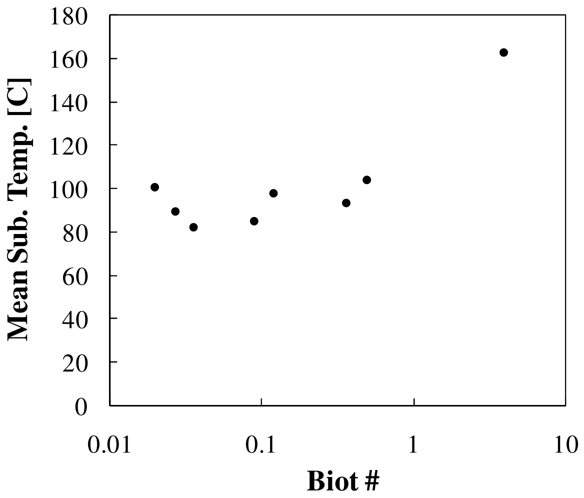

Figure 3.6 Mean device temperature as a function of the Biot number, where Bi = h^*d_{sub}/k_{sub}. For low Biot numbers the device temperature is sensitive to the fluid temperature and at high Biot numbers to the transverse thermal resistance, d_{sub}/k_{sub}.

3.6.2 Impact of Substrate Spreading during Two-Phase Flow

Spreading also has an impact during two-phase flow similar to that observed during single phase flow. However, we now have the opportunity to consider the impact that spreading might have on vapor venting and device performance. Figure 3.7 shows the spatial and bulk pressure drop. Vapor removal leads to an average improvement in the pressure drop of around 23% compared to a non-venting device, though a volumetrically equivalent heat exchanger would perform better with an improvement of over 80%. Changes in axial resistance of 5 orders of magnitude impact the relative pressure drop only slightly among the three device types.

Figure 3.8 shows the spatial and bulk substrate temperatures. Again we find a slight improvement in the venting devices due to the improvement in the pressure. This improvement is found to be a maximum of 3.5 C. The volumetrically equivalent device, due to the much lower pressure drop, also has the lowest device temperature for all but the highest axial resistance case. Due to the large transverse resistance for this simulation case the device temperatures are much higher such that the reduction in the heat transfer coefficient in the larger volumetrically equivalent device plays a greater role in setting the substrate temperature as compared to the reduction in fluid saturation temperatures due to the improved pressure drop. Thus both venting and non-venting devices thermally outperform the larger diameter equivalent volume devices as the Biot numbers and transverse thermal resistance increases.

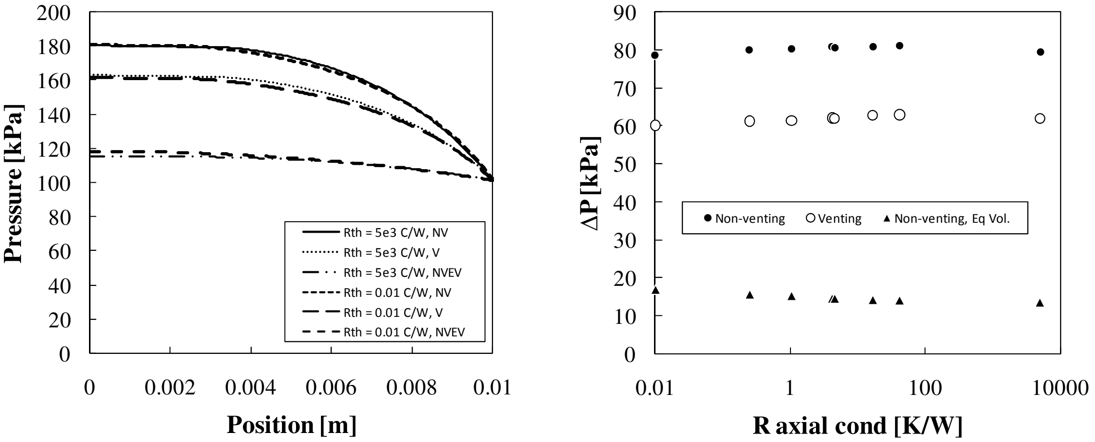

Figure 3.7 Spatial pressure profile and total pressure drop for varying values of axial thermal resistance during two-phase flow in the non-venting (NV), venting (V) and non-venting equivalent volume (NVEV) device. In the NVEV device the liquid channel occupies the same volume as the liquid channel, membrane and vent channel does in the venting device. Spreading only slightly alters the pressure profile and total pressure drop in the device.

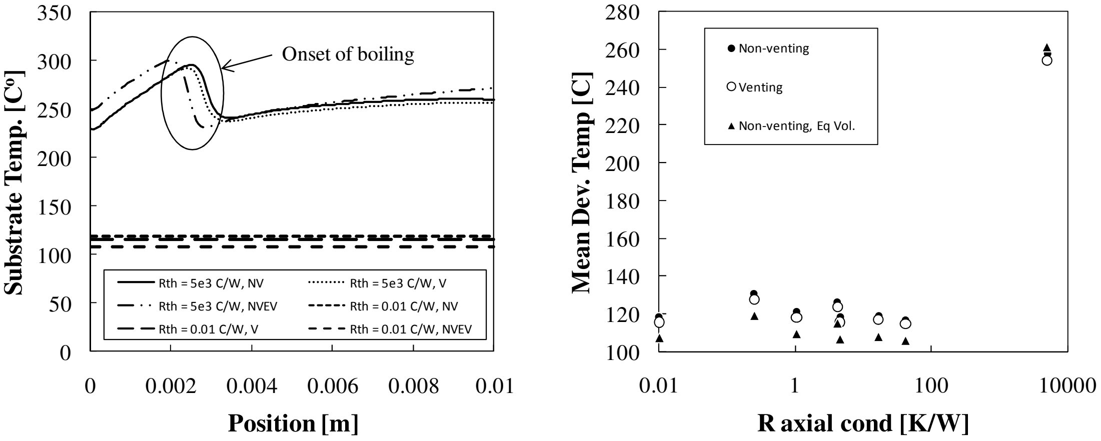

Figure 3.8 Spatial substrate temperature and mean device temperature for varying degrees of axial thermal resistance in the non-venting (NV), venting (V) and non-venting equivalent volume (NVEV) device. In the NVEV device the liquid channel occupies the same volume as the liquid channel, membrane and vent channel does in the venting device. A high thermal resistance increases the temperature magnitude and increases spatial variations due to reduced spreading.

Figure 3.9 shows the vapor removal rate along the length of the channel and indicates that as spreading increases the vapor removal starts earlier along the channel. This is due to greater power redistribution to the upstream half of the device such that boiling and vapor generation begins earlier. The slight increase in the vapor removal combined with higher average fluid temperature in the single phase region leads to a slightly smaller pressure drop with decreasing axial resistance as can be seen in Figure 3.7.

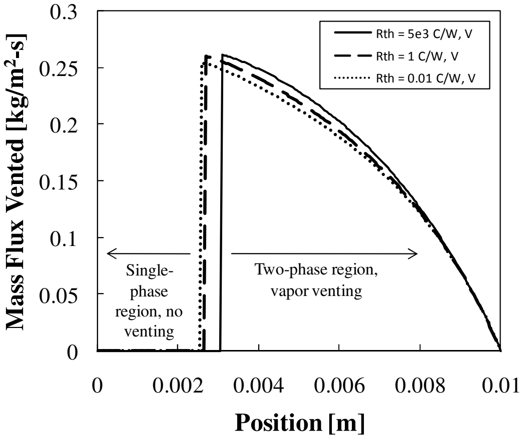

Figure 3.9 Vapor venting profile along the length of the venting device. Abrupt increase occurs when flow in the liquid channel transitions from single to two-phase, where the vapor formed can flow through the membrane. Spreading results in a shift upstream of the single to two-phase transition point resulting in earlier venting.

Thus, the hydraulic and thermal improvement of the venting device over a non-venting device increases with reducing axial substrate resistance. However, it is thermally superior to the non-venting equivalent volume device only at high transverse resistances.

3.6.3 Impact of Membrane Conductance

Given a fixed area, the membrane conductance, $C_{mem} = \kappa \cdot L \cdot w_{chan}/t_{mem}$, is directly proportional to the membrane intrinsic permeability, κ, and inversely proportional to the membrane thickness, t_{mem}. The larger the conductance the smaller the required pressure drop to vent a given volume of vapor. Thus it is strongly beneficial to have a membrane with a very high conductance for a vapor venting heat exchanger.

Figure 3.10 shows the pressure drop, substrate temperature and heat transfer coefficient for a non-venting, vapor venting and non-venting equivalent volume device as the membrane thickness and membrane permeability are increased.

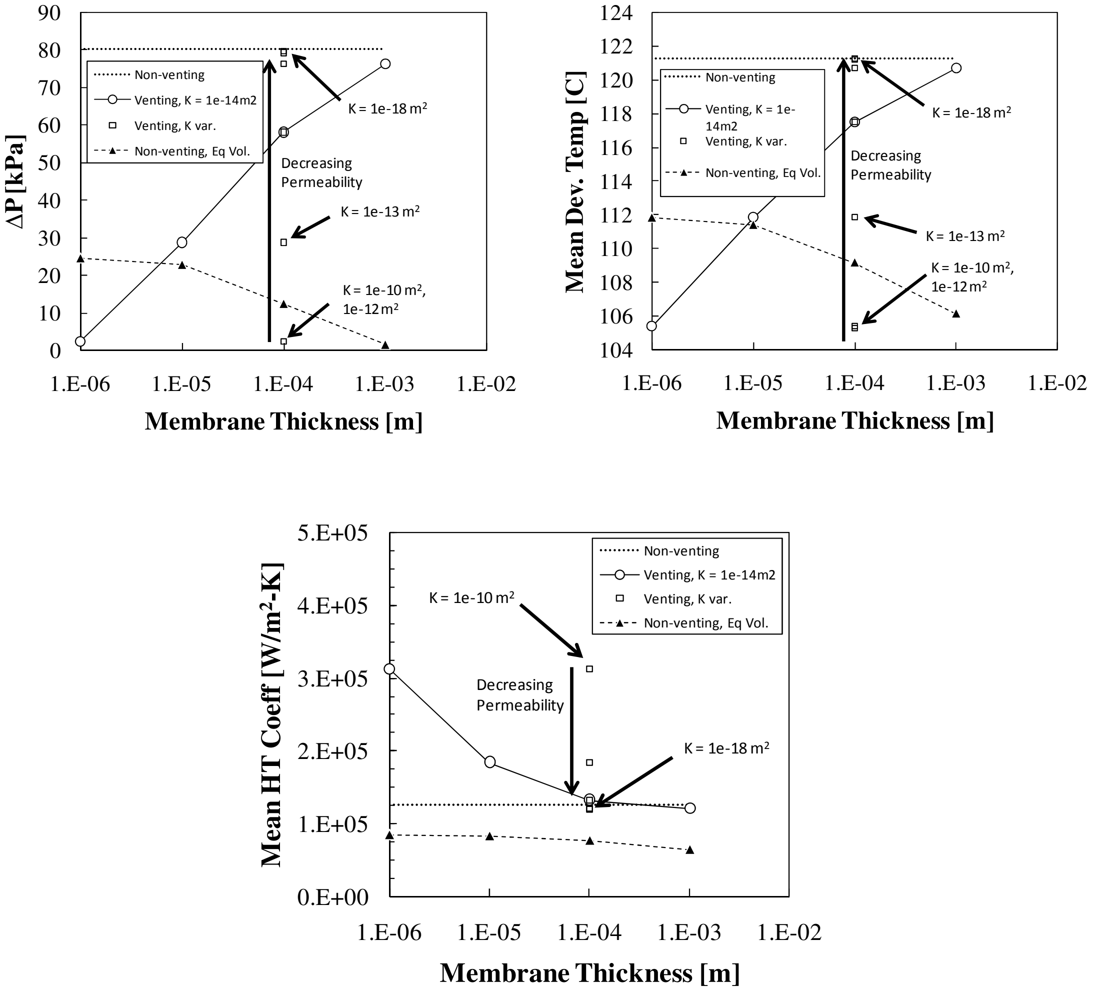

Figure 3.10 Impact of membrane thickness and intrinsic permeability on the total pressure drop, device temperature and heat transfer coefficient in the non-venting, venting and non-venting equivalent volume (NVEV) devices. In the NVEV device the liquid channel occupies the same volume as the liquid channel, membrane and vent channel does in the venting device. Reducing membrane thickness and/or increasing permeability can significantly improve the performance of the venting device, potentially beyond that achievable in a NVEV device.

As the membrane thickness is increased, the membrane conductance reduces, reducing the improvement in pressure drop and device temperature as well as reducing the heat transfer coefficient. Additionally the non-venting equivalent volume device becomes more beneficial as the additional volume gained from the elimination of the membrane increases the hydraulic diameter and thus reduces the pressure drop. And despite the reducing heat transfer coefficient the improvement gained from the reduction in saturation temperatures helps lower the substrate temperatures. It is also evident that increasing the permeability for a given thickness helps reduce pressure drops and device temperatures for the venting device. The pressure drop and temperature curves for the venting device and non-venting equivalent volume device show an envelope of potential membrane thickness-permeability combinations that would lead to equivalent or superior hydraulic and thermal performance. For a 100µm thick membrane, permeabilities of 3e-13 m^2 or higher are necessary to provide superior performance. If a thinner membrane is used, a lower permeability membrane would be sufficient.

Figure 3.11 shows the pressure drop, device temperature and vapor venting fraction as a function of the membrane conductance. As expected, the pressure drop and device temperature reduce as the venting fraction increases with increasing membrane conductance. For the given channel dimensions, complete venting is achieved with a conductance of 1e-14 m^3 or greater.

Figure 3.12 shows the venting fraction plotted against the membrane-channel conductance ratio. No vapor venting occurs when the conductance of the membrane is four orders of magnitude smaller than that of the channel (= D^4/L) and complete venting occurs when the conductances are of the same order or larger.

To maximize the pressure drop and device temperature improvement over a non-venting device it is essential to use a membrane with a conductance above that of the microchannels. Similarly, to improve the performance of the venting device over that of a non-venting equivalent volume device it is beneficial to use a membrane with a conductance larger than that of the volumetrically equivalent microchannels. This can be achieved through the use of thinner membranes; however this must be balanced against manufacturability, reliability and mechanical considerations that may limit the minimum thickness of the membrane. Membranes can be made more permeable by increasing the pore diameter but this limits the maximum pressure drop that can be sustained before liquid overcomes the capillary pressure and begins to leak through the membrane into the vent channels. Membranes with permeabilities in the range of 1e-12 m^2 to 1e-15 m^2 are commercially available and could be potentially used for the venting heat exchanger.

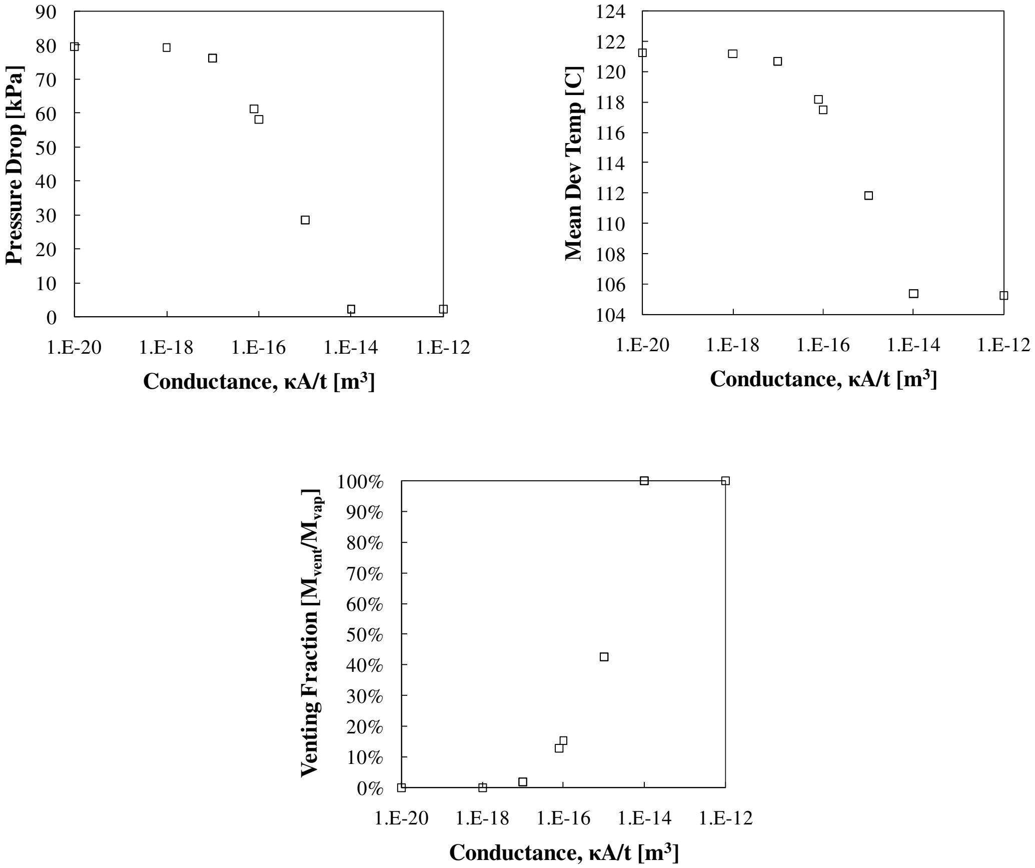

Figure 3.11 Increasing membrane conductance leads to a clear reduction in pressure drop and device temperature as the vapor fraction removed through the membrane increases. The vapor removal and device performance is maximized at a conductance of 1e-14 m^3.

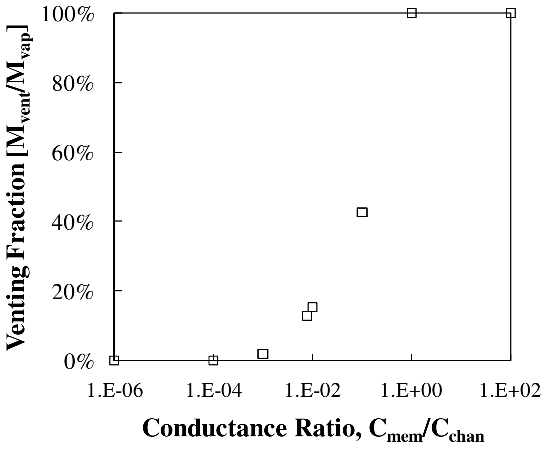

Figure 3.12 Vapor removal fraction as a function of the conductance ratio. When the conductance of the membrane is increased to the same order as that of the channel, all the vapor produced is vented, leading to very low pressure drop and device temperatures.

3.6.4 Impact of Channel Density

Figure 3.13 shows the impact of channel density, or fin-to-channel width ratio, on the pressure drop, substrate temperature and mean heat transfer coefficient. Increasing the fin width leads to fewer channels and consequently higher mass flux, since the total mass flow rate remains the same between the test conditions. As the channel density is reduced the mass flux increases and the pressure drop increases. The increased pressure drop increases the saturation temperature and thus device temperatures. The heat transfer coefficient also reduces with increasing fin-to-channel ratio since the flow remains as a single phase fluid for comparatively longer due to the shift in saturation conditions.

In all simulated cases the venting device performs better than the non-venting control device with the largest improvement in pressure drop of 23% obtained at a ratio of 1 and in temperature of 3.2% at a fin-to-channel ratio of 2.5, though the temperatures are most favorable at the smallest ratio of 0.1. However, the non-venting equivalent volume device consistently outperforms the venting device.

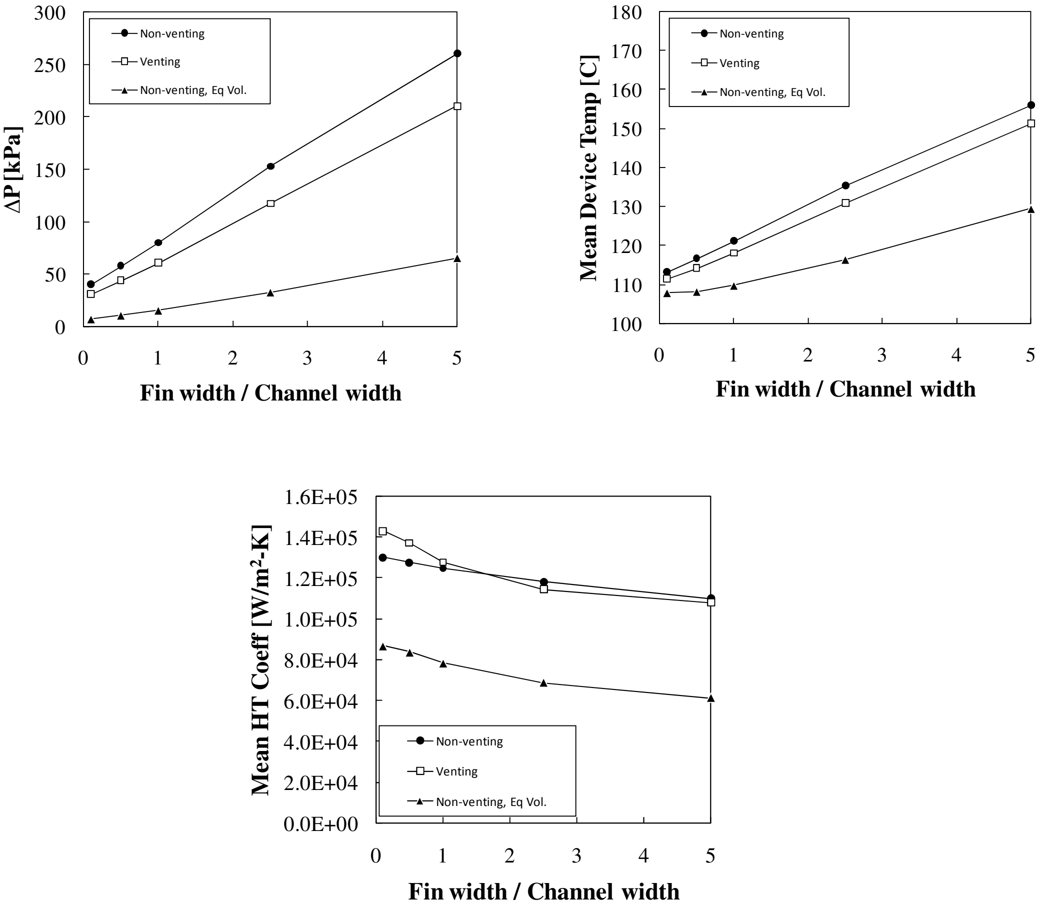

Figure 3.13 Pressure drop, mean device temperature and heat transfer coefficient in the non-venting device, the venting device and the non-venting equivalent volume (NVEV) device as the fin-to-channel width is increased while maintaining the same total liquid flow-rate and heat flux. In the non-venting and venting devices the liquid channel is 100µm square while in the NVEV the liquid channel consumes the volume occupied by the membrane and the vent channel in the venting device and is 100µm x 265µm. Higher fin-to-channel width ratios lead to fewer channels and higher mass fluxes through each channel, increasing the pressure drop and device temperatures. Increased pressure also delays boiling and reduces the mean heat transfer coefficient.

Changing the fin width also alters the fin efficiency as shown in Figure 3.14, where small fin widths lead to a lowered efficiency. The non-venting equivalent volume device has the poorest fin efficiency due to the comparatively taller channels.

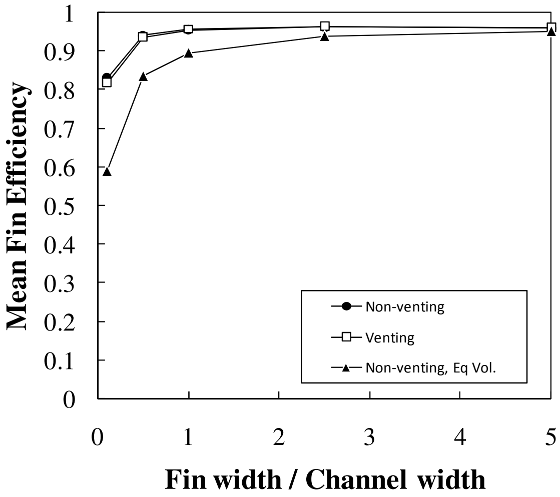

Figure 3.14 Impact of fin-to-channel width ratio on the fin efficiency in the non-venting, venting and non-venting equivalent volume devices. As the fins are widened, the fin efficiency improves, though the advantage gained is small after a fin-to-channel width ratio of about 1 when using copper as the substrate.

Figure 3.15 shows the bulk and spatial vapor removal rate in the venting device. The vapor vented is dependent on the area of membrane exposed to two-phase flow and the driving pressure. As the channel density is reduced, the mass flux increases, causing the pressure to rise. The rise in pressure helps increase venting but conversely leads to a relatively longer fraction of single-phase flow in the channel. The reduction in density also reduces the total amount of venting area available. The competing factors result in the non-monotonic behavior in the vapor removal as the fin-to-channel ratio is increased.

From a thermal standpoint it is beneficial to have a device with the smallest fin-to-channel ratio and the highest channel density. This leads to the lowest pressure drop and substrate temperature. The addition of a membrane may not lead to the highest potential improvement at this operating point but the lowered magnitudes are more beneficial.

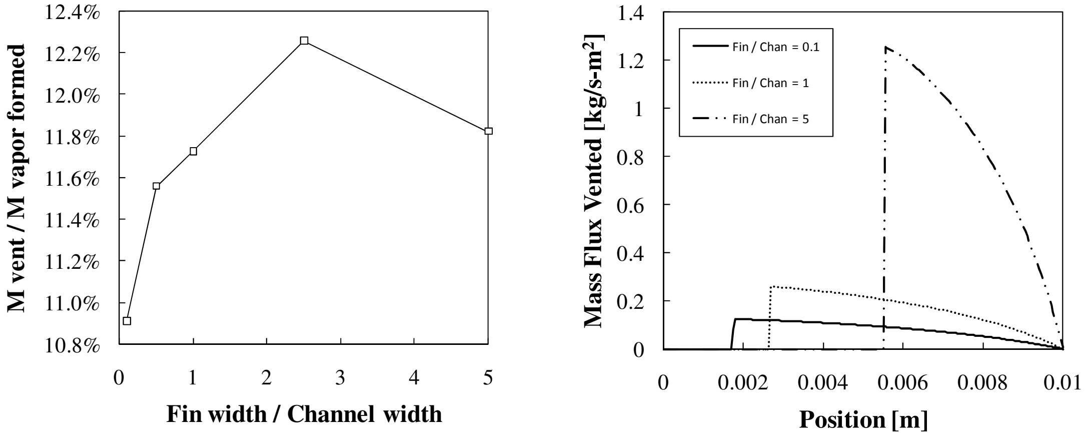

Figure 3.15 Venting percentage and spatial profile of mass flux vented as the fin-to-channel ratio is varied. The amount of vapor vented initially increases due to the larger pressure on the liquid side as the channel density reduces.

3.6.5 Impact of Channel Hydraulic Diameter

The bulk pressure drop, substrate temperature and heat transfer coefficient as the liquid and vent channel diameters are increased from 50μm to 250μm are shown in Figure 3.16. The improvement in the pressure drop and temperature between the venting and non-venting device is largest at the smallest channel diameter of 50μm and is found to be 46% and 9% respectively. The non-venting equivalent volume device again consistently outperforms both the venting and non-venting control devices. The device temperatures show a non-monotonic behavior due to the competing effects of lower saturation temperatures as the channels get larger versus lowered heat transfer coefficients. Since the pressure drop scales with the fourth power of the diameter the reduction in pressure drop and saturation temperature is larger at smaller channel diameters. At larger channel diameters the reduction in saturation temperature begins to be offset by the reduction in the heat transfer coefficient resulting in an increase in the device temperatures.

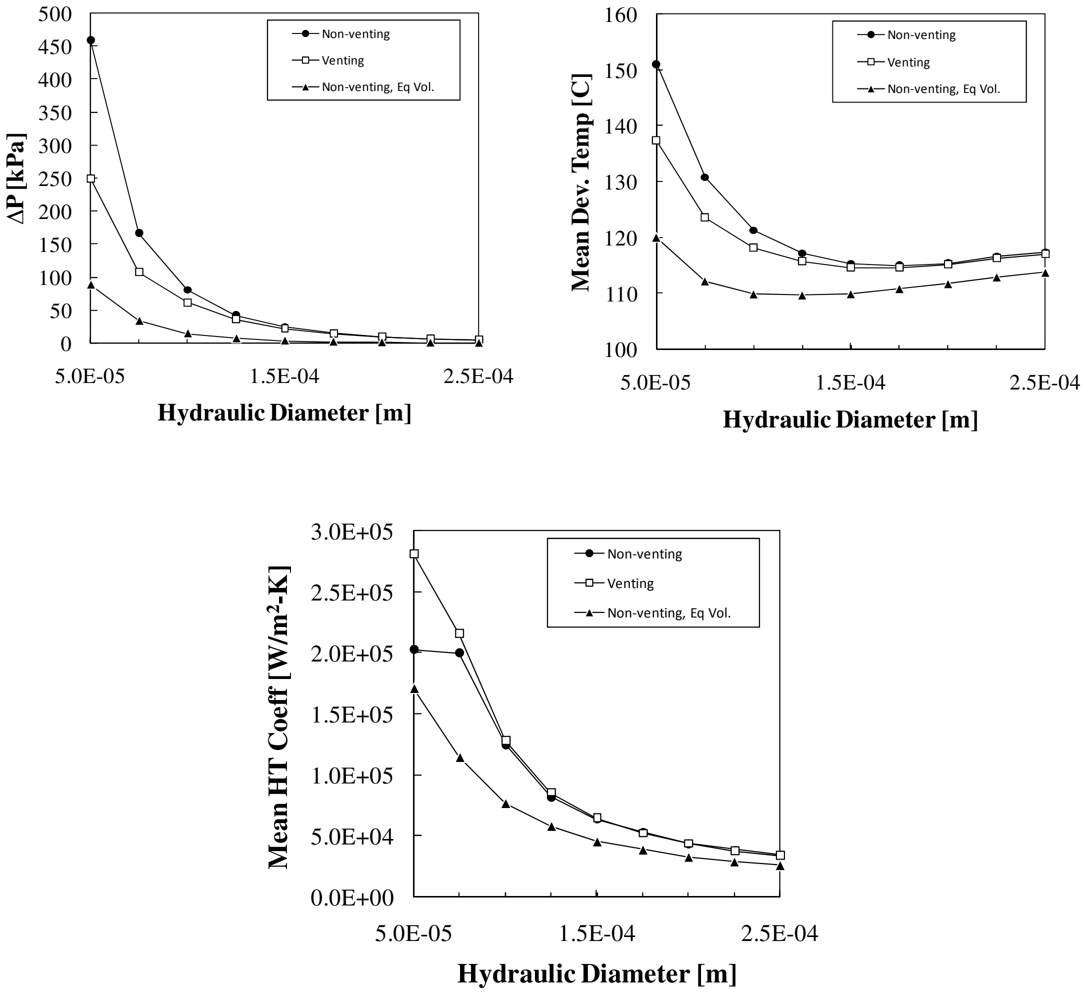

Figure 3.16 Pressure drop and heat transfer coefficient reduce monotonically as the channel diameters are increased in the non-venting, venting and non-venting equivalent volume (NVEV) devices. In the NVEV device the liquid channel occupies the same volume as the liquid channel, membrane and vent channel does in the venting device. Device temperatures rise after an initial drop due to the lowered heat transfer coefficient playing a greater role compared to the reducing saturation temperatures. The venting device performs better than the standard non-venting device but is outperformed by the non-venting equivalent volume device.

Figure 3.17 shows the vapor removal fraction and trans-membrane pressure as the channel diameters are increased. Due to a strong reduction in the pressure drop as the channel is increased from 50µm, the trans-membrane pressure reduces, decreasing the amount of vapor vented. The amount of vapor removed at smaller channels would be even higher if not for the shift in saturation conditions that occur due to the larger liquid pressure, resulting in comparatively longer single-phase flow in the device. The vapor removal is also reduced due to the larger pressure that develops in the smaller vent side channels as vapor is vented. These results support the earlier discussion in Section 3.6.3 regarding the membrane-channel conductance ratio, where the venting is maximized at larger ratios. In the current simulation, as the channel diameters are increased, the conductance ratio reduces from 0.06 to 5e-4 and venting fraction reduces from 25% to 1%. A small channel combined with a better membrane could lead to complete venting and significant pressure drop and thermal improvements.

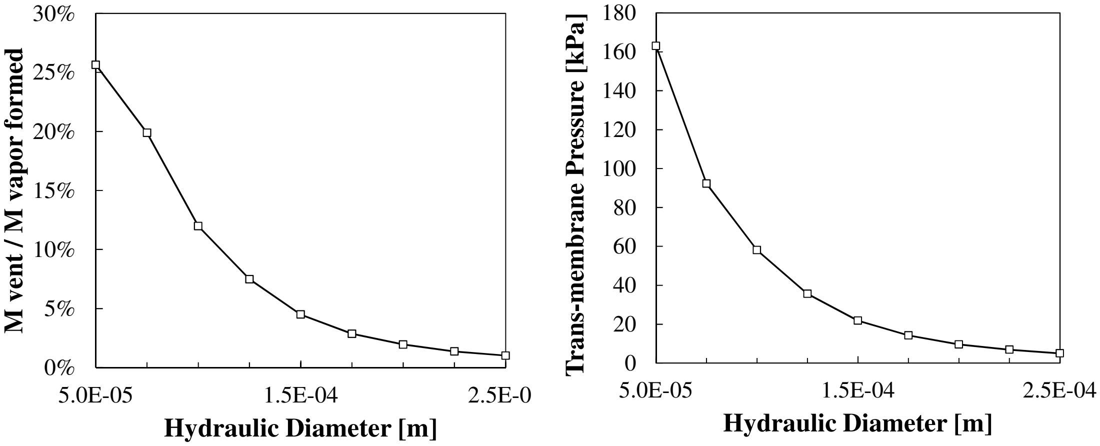

Figure 3.17 Vented vapor fraction (left) reduces as the channel diameters are increased due to the reduced trans-membrane driving pressure (right). These results imply the use of smaller channels to increase venting, but this results in higher pressure and temperature magnitudes when using the current membranes.

3.6.6 Impact of Liquid-Vent Channel Diameter Ratio

The last aspect we considered is the impact of varying the ratio of the liquid to vent channel diameters. Increasing the vent side channel diameter reduces the vent side pressure that develops as vapor flows, which impedes further venting through the membrane. However, increasing the vent side channel also increases the total volume of the device and provides an advantage for the non-venting equivalent volume device.

Figure 3.18 shows the pressure drop, substrate temperature and heat transfer coefficient for the non-venting, venting, and non-venting equivalent volume devices. Increasing the vent side channel diameter shows improvement in the pressure drop and device temperature for the venting and non-venting equivalent volume devices. The heat transfer coefficient however increases for the venting device due to increased vapor removal as the vent channels get larger and reduces for the non-venting equivalent volume device due to the increasing flow channel diameter.

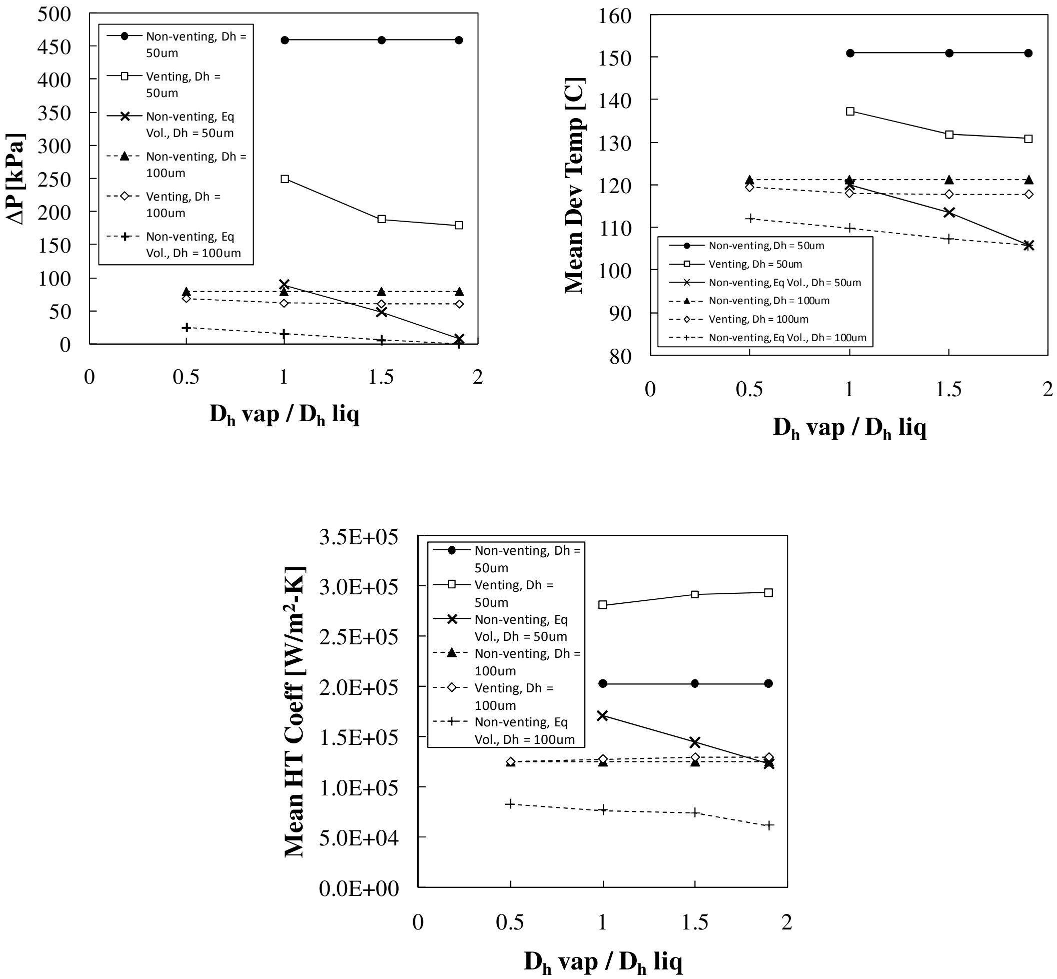

Figure 3.18 Pressure drop, mean device temperature and heat transfer coefficient as the liquid-to-vent channel ratio is varied in the non-venting, venting and non-venting equivalent volume (NVEV) devices at two different liquid side channel diameters, 50µm and 100µm. The NVEV device occupies the same volume as the venting device. As the vapor-to-liquid channel ratio is increased, the pressure drop, device temperatures and heat transfer coefficients improve in the venting device as compared to the non-venting device. However, the NVEV device shows the lowest pressure drop and device temperatures.

In all cases the venting device performs better than the non-venting control but poorer than the non-venting equivalent volume device. The maximum pressure drop and temperature improvement over the non-venting control occurs at the largest vent-to-liquid channel ratio of 1.9 for the 50μm liquid channel diameter case and is found to be 61% and 13% respectively. The venting device performs comparatively better against the non-venting equivalent volume device at the lowest vent-to-liquid channel ratio of 1 (for the 50μm channel case) and 0.5 (for the 100μm and 200μm channel cases).

Figure 3.19 shows the vapor fraction removed and the vent side pressure for the venting device and shows that increasing the vent side channel diameter helps increase the amount of vapor removed by lowering the vent side pressure.

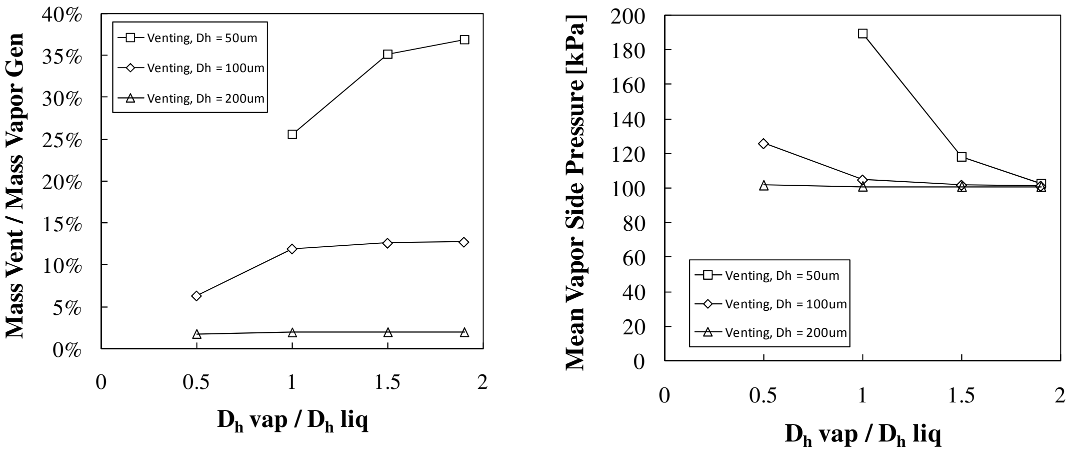

Figure 3.19 Increase in the channel ratio leads to a smaller vent side pressure (right) and thus a larger fraction of the vapor venting (left). This behavior is more significant when using smaller channels where the magnitude of the pressures is larger.

The results indicate that maximizing the vent side channel diameter helps increase the amount of vapor removed and reduces the pressure drop and device temperatures. Increasing the vent channel diameter also increases the total volume and so a non-venting equivalent volume device performs comparatively better as well.

3.7 Limitations of the Current Approach and Future Developments

A key limitation in the model developed is the lack of flow regime dependent behavior. As discussed in Chapter Two, Harirchian and Garimella [74] and Revellin and Thome [75] have made important recent contributions to flow regime development but further investigation is necessary for the use of water as the working fluid as well as for flow in high aspect ratio channels (as is the case in the volumetrically equivalent device discussed here). The addition of flow regime dependent behavior is expected to reduce the thermal performance of the volumetrically equivalent device since annular flows, which is assumed in the model, is less likely in larger narrower channels, with less thermally beneficial plug and/or stratified type flows more likely to develop. Similarly, as discussed in Chapter 2, we expect flow regime to play a role in the venting device as well; the addition of a hydrophobic membrane can alter the flow structure with stratified flows, which possess poorer thermal characteristics, more common at lower mass fluxes, and churning annular flows, with potentially better thermal characteristics, dominant at higher mass fluxes.

In future modeling work we would incorporate flow regime transitions to the model as well as flow regime specific heat transfer and hydraulic models. As observed in the previous chapter the simple transition criteria developed by Harirchian and Garimella works reasonably well in predicting our flow transitions from stratified to churn/annular flows. Simplified film thickness based heat transfer models or model modifiers could then be included for flow regime sensitive heat transfer. Two-phase flow in large aspect ratio channels requires the development of new transition criteria since little published data is currently available. The work of Steinbrenner *et al.* [93] is the most promising as they model and study the flow regimes in high aspect ratio channels during adiabatic gas-liquid flow for use in fuel cell microchannels. Incorporating these phenomenological models would help provide a more accurate picture of the performance of the vapor venting and non-venting volumetrically equivalent channels.

3.8 Summary of Findings and Conclusions

The key goal of this chapter was to develop a two-phase vapor venting model and then use it to study the impact of various factors on the venting, thermal and hydraulic performance of a vapor venting heat exchanger.

Substrate conduction resistance:

- Substrate heat spreading has little impact in improving the hydraulic performance of the venting or non-venting equivalent volume devices over that of control non-venting device.
- The venting device has the best relative thermal performance compared to the non-venting equivalent volume device at high Biot number conditions but at the expense of high temperature magnitudes.
- The venting device has the best relative thermal and hydraulic performance compared to the standard non-venting device using low axial resistance substrates with high spreading.

Membrane Conductance:

- The venting device performs thermally and hydraulically better relative to the non-venting control as the membrane-to-channel conductance ratio is increased from 1e-4 to 1.
- The venting device also outperforms the non-venting equivalent volume device at conductance ratios of unity order with performance improving as the membrane thickness is reduced.

Channel density/Fin width

- Reducing the fin-to-channel width ratio increases the channel density and reduces the mass flux per channel. This leads to reduced pressure drops and improved device temperatures.
- The venting device performs thermally better at low channel densities and hydraulically better at higher channel densities compared to the non-venting control.

- The venting device does not perform better than the non-venting equivalent device under any tested condition. It performs less poorly thermally at high channel densities and hydraulically at low channel densities.

Channel hydraulic diameter:

- The venting device performs better than the standard non-venting device at all diameters but the best at the smallest tested channel diameter, at the expense of large pressure and temperature magnitudes. Increasing the channel size reduces the magnitude but also reduces the need for vapor separation as the advantage of vapor venting reduces.
- The non-venting equivalent volume device outperforms the venting device under all tested conditions, though its hydraulic advantage reduces as the channel size reduces and its thermal advantage reduces as the channel size increases.

Vent-to-liquid channel ratio:

- The venting device's hydraulic and thermal performance relative to that of the standard non-venting device improves as the vent-to-channel diameter ratio increases. The performance is comparatively better when using smaller liquid channels at the expense of higher pressure and temperature magnitudes.
- The venting device performs worse than the non-venting equivalent volume device at all tested conditions with the disadvantage the least at the low vent-to-liquid channel ratios.

The results show that the addition of a venting membrane always leads to better hydraulic and thermal performance when compared against a standard non-venting device but is only better than a non-venting equivalent volume device under very limited conditions. Increasing the membrane-to-channel conductance ratio is essential to improve performance and can be achieved through the use of smaller liquid channels, reducing the thickness of the membrane, using membranes with high permeability or increasing the vapor removal area.

For example, in a 50µm liquid channel device a membrane with 20X conductance than the default 65µm thick, 220nm pore diameter PTFE membrane could potentially lead to complete venting and low pressure drops and device temperatures, even beyond that capable by a non-venting equivalent volume device. Assuming simple capillary pores, the permeability scales with the square of the pore diameter, thus increasing the pores to approximately 1.1µm or larger from the current 220nm pores would provide sufficient increase in the conductance, though the breakthrough pressure, which scales inversely with the pore diameter, would be ~5X smaller. It is also advantageous to increase the vent side channel diameter without increasing the volume considerably. This could be achieved by using a very low aspect ratio vent chamber rather than mating channels, though this require the membrane be attached to the liquid channels using epoxy or the use of mechanically stiff membranes. The combination of small diameter liquid channels, high conductance membranes and larger hydraulic diameter, low volume vent channels could provide significant hydraulic and thermal benefits compared to a standard non-venting or volumetrically equivalent non-venting device.

CHAPTER 4 DESIGN, FABRICATION AND EXPERIMENTAL CHARACTERIZATION OF AIR AND VAPOR VENTING MULTICHANNEL DEVICES

4.1 Motivation and Overview

Having carried out adiabatic and diabatic visualization of phase separation in single channels to construct flow regimes in Chapter 2, and modeled and carried out a parametric analysis of a microchannel vapor venting heat exchanger in Chapter 3, it is now critical to characterize the performance of actual operating two-phase vapor venting heat exchangers, and compare it against the previous numerical and visualization work.

In this chapter we focus on the design, fabrication and characterization of a silicon microchannel gas venting device and a copper microchannel vapor venting heat exchanger heated via an AMD thermal test chip. The devices were designed to operate at temperatures up to 125°C and gage pressures of 150 kPa (20 psi) with the copper device capable of dissipating heat fluxes of 820 kW/m^2 for water mass fluxes ranging from 102 kg/s-m^2 to 420 kg/s-m^2 (2 ml/min to 8 ml/min). The key goals of the work covered in this chapter were to i) identify successful fabrication schemes to construct vapor venting heat exchangers in copper and silicon, ii) characterize the hydraulic, thermal and venting performance of the fabricated devices and iii) compare the results against a non-venting heat exchanger and two-phase vapor-venting flow model (discussed in detail in Chapter 3).

Heat exchanger design and fabrication is discussed in the following section, followed by the experimental setup and data reduction in Section 4.3. Section 4.5 presents the experimental results and discussion of the findings from the silicon and copper devices.

4.2 Design of the Vapor Separating Microchannel Devices

4.2.1 Venting Membrane

The porous hydrophobic membrane is the key component in the vapor venting heat exchanger and enables the separation and transport of the vapor/gas phase. Pore size, membrane thickness, intrinsic permeability, hydrophobicity, and thermo-mechanical stability are all important aspects that need to be considered when selecting or fabricating the phase separation membrane. The liquid leakage pressure (or breakthrough pressure) for the membrane is determined by the Young-Laplace equation, Eq. (4.1), and varies inversely with the pore diameter, d_{pore}, and directly with the cosine of the advancing contact angle, $\theta_{adv,max}$, and the surface tension, σ [52].

$$\Delta P_{leak} = \frac{4 \cdot \sigma \cdot \cos(\pi - \theta_{adv,\max})}{d_{pore}} \tag{4.1}$$

The total pressure drop across the membrane for single-phase, viscous, laminar flow, with Reynolds and Knudsen numbers less than 1, is given by Darcy Law, Eq. (4.2), where κ, is the intrinsic permeability of the membrane, t_{mem} is the thickness, G_{mem} the mass flux and μ and ρ the dynamic viscosity and density of the fluid being transported.

$$\Delta P_{mem} = G_{mem} \cdot \frac{\mu}{\rho} \cdot \left(\frac{1}{\kappa} \cdot \frac{1}{t_{mem}} \right) \tag{4.2}$$

The general relation between κ and pore diameter, d, is given by Eq. (4.3) and if we assume that the pores in the membrane can be approximated as capillaries, then κ can also be related to the porosity, ε, as shown in the second equality.

$$\kappa = C \cdot d^2 = \frac{\varepsilon \cdot d^2}{32} \tag{4.3}$$

The ideal membrane for use in two-phase heat exchangers would: i) possess a leakage pressure, ΔP_{leak}, larger than the maximum operating pressure expected across the membrane and ii) have a low pressure drop across the membrane, ΔP_{mem}, to increase the vapor removal rate. This requires that the membrane have a large contact angle with the working fluid, high intrinsic permeability and be thin. Hydrophobic membranes with graded pore diameters, with pores at the separation surface facing the two-phase flow being small to ensure liquid does not leak into the membrane, and larger pores in the bulk of the membrane to increase permeability, is ideal, though not easily available.

Based on the requirements and our previous study into the temperature dependent behavior of various hydrophobic membranes [67] we chose to use the same 220nm pore diameter PTFE membrane used in Chapter 2, obtained from GE Water, USA and Sterlitech, USA, as the vapor separation layer. The membrane has a porosity of 0.5-0.8, measured thickness of 65µm ± 5µm, static contact angle of 123° for water at room temperature [60] and manufacturer stated upper limit temperature of 260°C.

4.2.2 Silicon Heat Exchanger

The key advantages of silicon fabricated heat exchangers are the flexibility in channel geometry design, the ability to fabricate resistive heaters and temperature sensors on the backside of the heat exchanger for on-chip thermal heating and sensing, and the low thermal mass that enables study of transient temperature effects. The key processing steps for the fabrication of the silicon heat exchanger is shown in Figure 4.1.

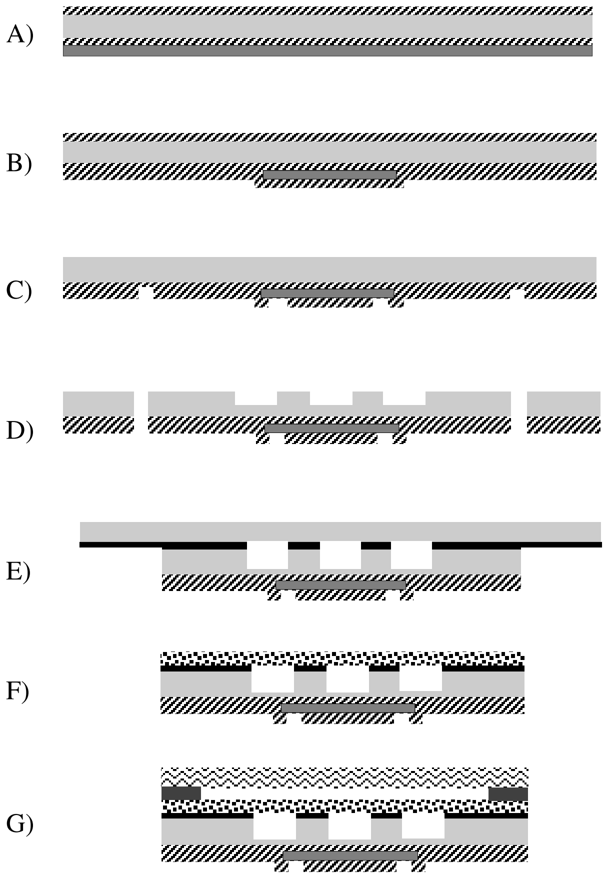

Growth of 0.25 µm of oxide on 400 µm double polished Si wafer, followed by sputtering of 0.5 µm of Al.

Once heaters and sensors have been patterned (Mask 1) and dry-etched, 0.5 µm of LTO is deposited to protect the metal structures

Backside LTO is patterned (Mask 2) and then pad-etched to allow wire bonding. Frontside oxide is stripped for dry etching.

Front-side liquid channels are then patterned (Mask 3) and dry-etched, followed by backside pattern (Mask 4) and dry-etch to create ports and release device.

2.5 µm of SU-8 is then contact printed on front-side using a SU-8 coated transfer wafer.

Membrane is attached and the SU-8 UV exposed and hard cured at 150 °C.

Double sticky mylar sheet is laser ablated to form vapor channels and attached to top of membrane followed by a glass slide to cap the device.

▒	Porous membrane (50 µm)	▨	SiO_2 (0.25 + 0.5 µm)	■	SU-8 (2.5 µm)
■	Double-sticky mylar (50 µm)	■	Aluminum (0.5 µm)	≋	Glass slide (2 mm)

Figure 4.1 Processing steps in fabrication of a silicon vapor venting heat exchanger.

Several different geometries were fabricated: straight parallel channels, serpentine single channels and aligned and staggered square pin fin arrays. Figure 4.2 shows the channel side of a serpentine channel heat exchanger before incorporation of the membrane using the contact print process (step E in Figure 4.1). This silicon heat exchanger is capped with glass to allow for observation of the flow and venting on the vapor side of the device. The straight parallel channel heat exchanger was tested and is presented here. This parallel channel heat exchanger has six channels with a length of 15mm, width of 400µm and depth of 170µm (hydraulic diameter = 240µm). A single vapor chamber was used to capture the vapor vented through the membrane. This vapor chamber has a length of 15mm, width of 5mm and a depth of 50μm. The hydraulic diameter of the vapor chamber/channel should ideally be larger than the liquid channels to maximize venting as discussed in Chapter 3, however the depth was limited here by the thickness of the Mylar sheet used to make the vapor chamber. Heat flux is generated by four aluminum thin film resistive heaters with an average room temperature resistance of 43 Ohms. The heaters and the channel region of the device occupy the same footprint of $0.75cm^2$. Sixteen thin film aluminum resistance thermometers were fabricated but not used due to poor reliability. The dog-bone extensions on either side were necessary for the attachment of ports and the thermal trench added to minimize conduction loss from the heated microchannel region to the plenums.

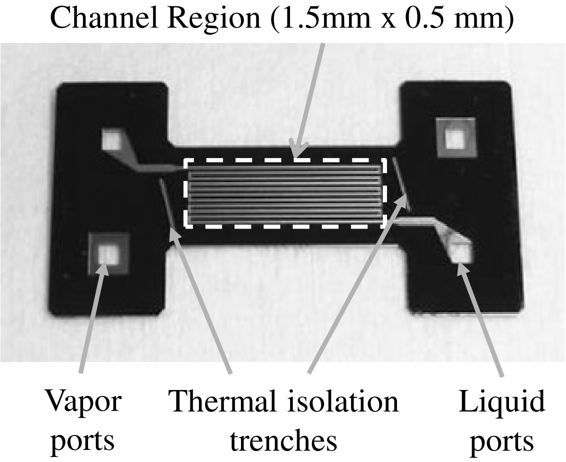

Figure 4.2 Channel side of the silicon microchannel heat exchanger. The thermal isolation trenches were added to reduce heat loss from the heated channel region to the manifolds during diabatic experiments.

4.2.3 Copper Heat Exchanger

The copper heat exchanger fabricated for this study is shown in Figure 4.3 and Figure 4.4. One major advantage of this heat exchanger is the ability to easily insert or remove membranes such that different types of membranes could be used and then studied after use to gauge the impact of wear and fouling. The same microchannel device is used for all the experiments thus removing a source of variability between different device configurations. The copper microchannels and PTFE membrane were capped with either high temperature abrasion resistant polycarbonate/ULTEM or with copper. The liquid and vapor microchannels are fabricated out of 2.4mm thick polished copper using conventional machining. The copper heat exchanger has 19 channels with a length of 19mm, average width of 130µm (±5µm) and a depth of 134µm (±5µm). The mating vapor channels have the same length, a width of 125µm (±5µm) and a depth of 132µm (±10µm). Heat exchanger temperatures are measured using twelve thermocouples embedded approximately 1.2mm below the top of the channel walls in the arrangement shown in Figure 4.4. Fluid outlet, copper cap and ambient temperatures were also measured using thermocouples. Heat flux was generated by an AMD Thermal Test Chip, 19mm long and 11mm wide, with four heaters, each 18mm long and 2.75mm wide. Only the middle two heater strips were used, resulting in a heated area of approximately 1cm^2.

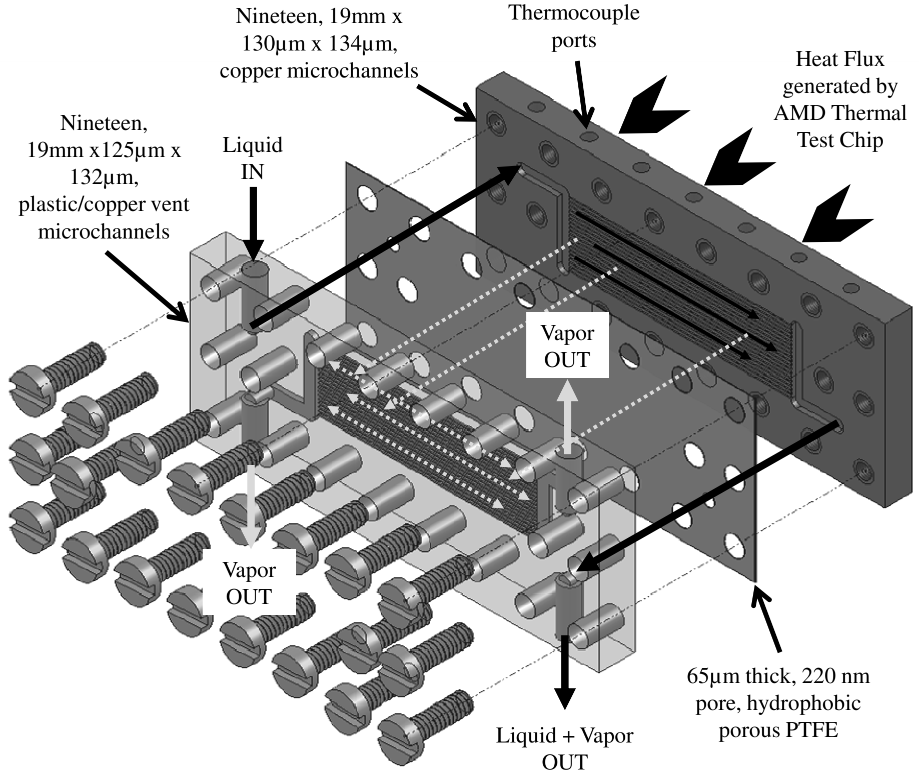
Nineteen, 19mm x 130µm x 134µm, copper microchannels
Thermocouple ports
Heat Flux generated by AMD Thermal Test Chip
Nineteen, 19mm x125µm x 132µm, plastic/copper vent microchannels
Liquid IN
Vapor OUT
Vapor OUT
65µm thick, 220 nm pore, hydrophobic porous PTFE
Liquid + Vapor OUT

Figure 4.3 Design and assembly of the copper microchannel heat exchanger used in this work. Screws and edges of device are coated with high temperature RTV to provide sealing. The channel region is 19mm long and 5.5mm wide with nineteen 130µm x 134µm microchannels.

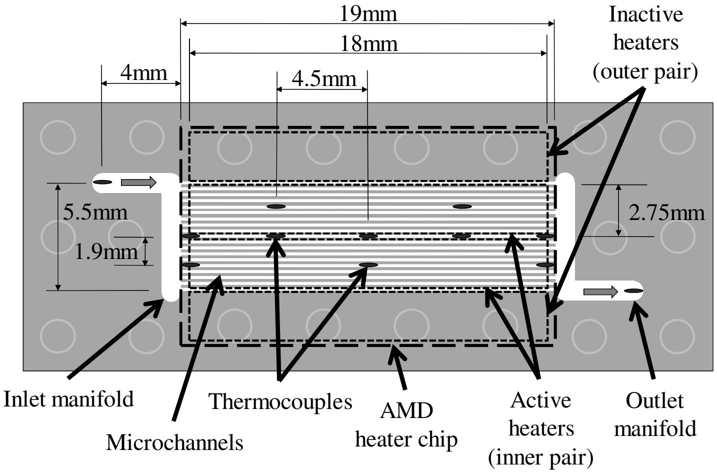
19mm
18mm
4mm
4.5mm
Inactive heaters (outer pair)
5.5mm
1.9mm
2.75mm
Inlet manifold
Microchannels
Thermocouples
AMD heater chip
Active heaters (inner pair)
Outlet manifold

Figure 4.4 Top view of tested microchannel device showing the manifold, microchannels, thermocouple measurement points and the relative position of the AMD heater chip with strip heaters. The twelve thermocouples are embedded 1.2mm below the top of the channel walls and the heat applied approximately 2.4mm below the top surface. Only the middle two heaters on the test chip are used to generate heat flux.

Three different device configurations were experimentally characterized as shown in Figure 4.5. In the control device, Figure 4.5.A, the channels are capped with a 400μm thick, non-porous high temperature silicone sheet and then with a flat copper cap. The sheet provides better sealing and prevents inter-channel leakage due to variations in surface planarity between the tops of the channel walls and the flat cover. In the venting heat exchanger, Figure 4.5.B, the porous membrane is sandwiched between mating sets of channels on the liquid and vent side. And finally, in the non-venting membrane device (NVMD), the porous PTFE membrane used in the venting device is instead capped with the flat copper plate.

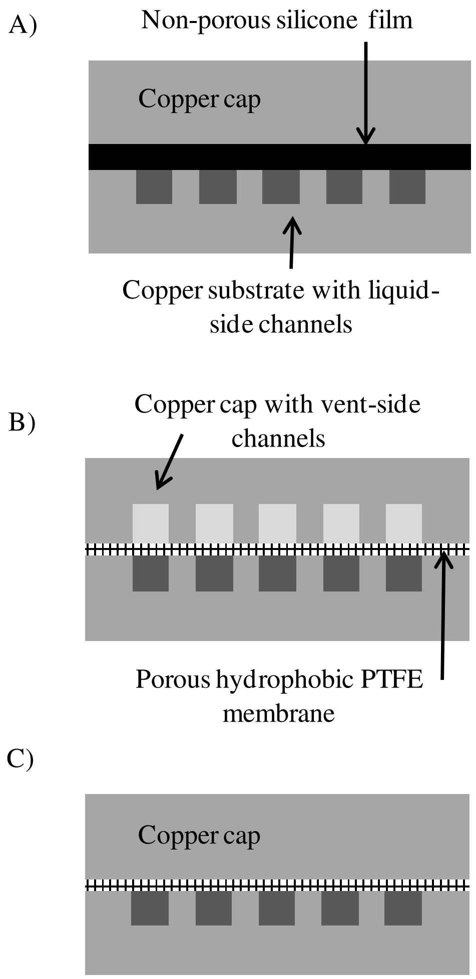
A)
Non-porous silicone film
Copper cap
Copper substrate with liquid-side channels
B)
Copper cap with vent-side channels
Porous hydrophobic PTFE membrane
C)
Copper cap

Figure 4.5 Schematics of the three different types of copper devices that were assembled and tested in this work. The PTFE membrane is 65µm thick and the silicone film is 400µm thick.

4.3 Experimental Method

4.3.1 Silicon: Adiabatic Experimental Setup and Procedure

The 400µm x 170µm parallel channel silicon heat exchanger is first tested using an adiabatic, air-water flow to quantify the adiabatic venting rate and venting efficiency of the device. The apparatus used is shown in Figure 4.6.

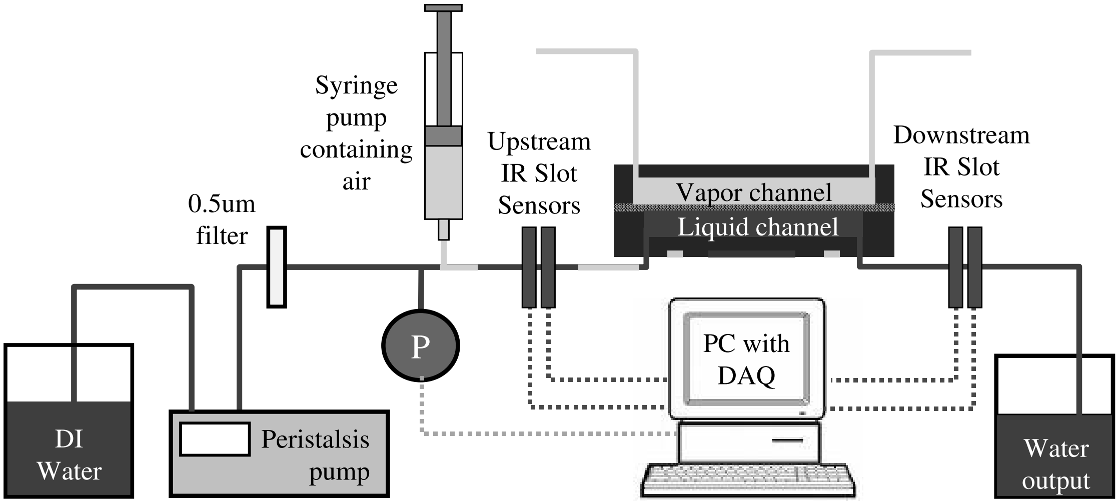

Figure 4.6 Experimental setup to study adiabatic vapor-venting and hydraulic stability of the vapor venting silicon device. IR slot sensors are used to measure void fraction and interface velocities from which inlet, outlet and vented air mass can be determined.

DI water, filtered in-line using a Swagelok 0.5μm particle filter, is pumped through the silicon device at 0.5 ml/min using a Shimadzu LC-10AD peristalsis pump, until the Omega PX309 0-5 psig pressure transducer reads steady state. The Harvard 11+ syringe pump is then switched on and air pumped at 1 ml/min. The air mixes with the liquid to form intermittent slugs of air and water downstream of the T-junction. Once steady state conditions for the mixed flow is reached, several minutes of data are recorded at 500Hz using a NI E-series PC-based DAQ card via a NI SCB100 breakout box. At the completion of the run, the air supply is switched off and the liquid allowed to flush any remaining air bubbles out of the system, before the experiment is repeated at the next air and liquid flow rate.

Air slug velocities, upstream and downstream of the silicon device, are determined from the interface velocities, measured using the pairs of IR slot sensors. The sensors use the change in the refraction of index to detect the presence or absence of liquid in the tubing (and not IR absorption, which is present, but not significant in the measurement). Average upstream air mass flow rate is calculated from the pump volumetric flow-rate and pressure. Non-vented downstream air mass flow rates are measured from the interface velocities and air-slug residence times. Since there is only a short length of 1/16” ID tubing downstream of the device, the pressure in the outlet tubing is assumed to be atmospheric.

4.3.2 Copper: Diabatic Experimental Setup and Procedure

The apparatus used to test the heat exchangers is shown in Figure 4.7. For the non-venting control and non-venting membrane heat exchangers, the vent side vacuum is not used. The fluid is pumped at a constant flow-rate using a Shimadzu LC10-AD peristalsis pump. The liquid-side inlet pressure is measured using an Omega PX219-30V45G5V pressure sensor and the vent-side vacuum pressure measured using an Omega PX219-30V15G5V pressure sensor. The syringe provides a vacuum of approximately 18kPa gage (83kPa absolute) when fitted with a 2kg mass (used by default); the vacuum can be adjusted by varying the attached mass. The vacuum is used to remove any condensed vapor and to increase the vapor removal rate by increasing the driving pressure across the membrane. Since the liquid is in a closed loop, vapor venting through the membrane results in a mass loss that is measured using a VICON electric mass scale with RS-232 attachment. The ice bath condenser ensures that the measured mass loss is solely due to vented vapor. To minimize heat loss to the ambient, the exposed copper cover of the heat exchanger is insulated with fiberglass and polyimide. The inlet and outlet tubing in the vicinity of the device is also insulated with fiberglass. All the thermocouples used in the study, save the inlet thermocouple, are Omega 40-gauge type-K insulated thermocouples. A type-T thermocouple is used to measure the inlet fluid temperature and is read by the AMD control system. Input heat flux was controlled and measured using the AMD control software. The temperature and pressure measurements were gathered at 10Hz using a NI E-series PC DAQ board via a low noise NI SCXI signal conditioning board and breakout box.

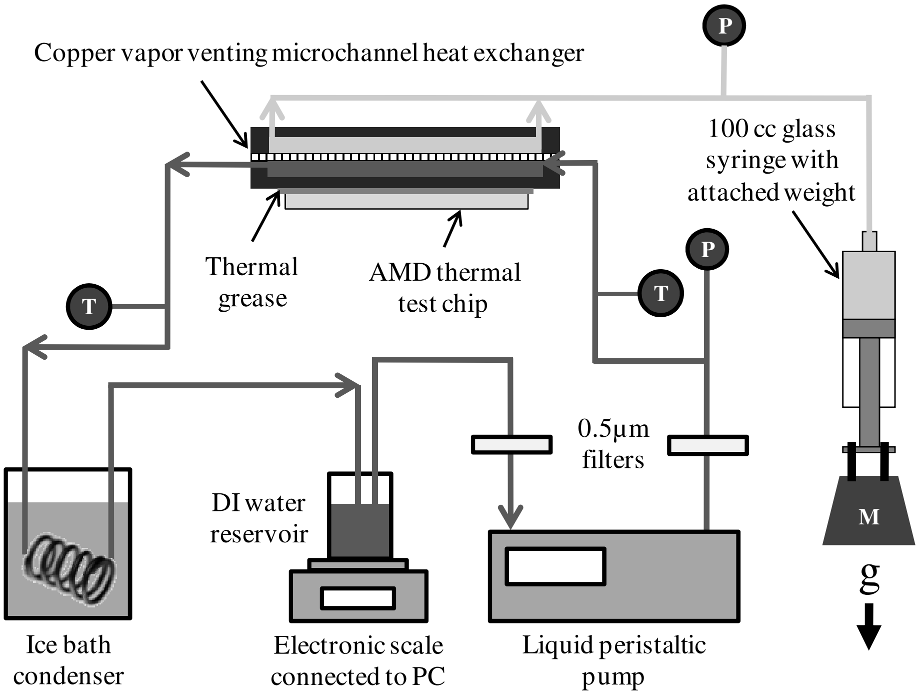
Copper vapor venting microchannel heat exchanger
P
100 cc glass syringe with attached weight
Thermal grease
AMD thermal test chip
P
T
T
0.5µm filters
DI water reservoir
M
g
Ice bath condenser
Electronic scale connected to PC
Liquid peristaltic pump

Figure 4.7 Experimental setup to study diabatic vapor venting from a copper microchannel heat exchanger. ‘P’ represents pressure sensors and ‘T’ thermocouples. Heat flux is generated by an AMD test chip and control platform. Vapor vent rate is calculated by measuring the mass defect using the electronic scale. Vacuum on vent side generated by syringe and mass. For control and non-venting membrane devices the vent side apparatus is not used.

4.3.3 Data Reduction and Error Analysis

4.3.3.1 Input and Effective Heating Power

The total input heating power is delivered using the thermal test chip and control hardware. The control system self-calibrates at the beginning of every run resulting in an uncertainty of 1mW. The heat flux reported in this work is based on the *actual* power absorbed by the fluid (after heat losses) divided by the heater area of 1cm^2. The sensible heating of the fluid during single-phase runs at the beginning of each experiment was used to determine the heat loss fraction at each tested mass flux. The average heat loss was found to be 24% at 102 kg/s-m^2, 10% at 208 kg/s-m^2, 6% at 307 kg/s-m^2 and 3% at 420 kg/s-m^2. Due to the increased convective heat transfer coefficient during two-phase flow the actual heat loss is expected to be smaller during flow boiling. Therefore, the single-phase heat loss fraction results in an overestimation of the thermal resistance and an under-estimation of the heat transfer coefficient during flow boiling.

4.3.3.2 Pressure Drop

The total measured pressure drop is composed of the terms listed in Eq. (4.4).

$$\Delta P_{tot} = \Delta P_{\mathrm{plenums}} + \Delta P_{\mathrm{tubing}} + \Delta P_{\mathrm{minor}} + \Delta P_{cont} + \Delta P_{\mathrm{exp}} + \Delta P_{\mathrm{chan,sp}} + \Delta P_{\mathrm{chan,tp,acc}} + \Delta P_{\mathrm{chan,t}} \quad (4.4)$$

The friction loss in the plenums (term 1) and tubing (term 2) and minor losses due to contractions, expansions and turns (term 3) are ignored as they were calculated to be less than 1% of the total pressure drop. The contraction and expansion at the plenum-channel and channel-plenum region (term 4 and 5) are the largest minor loss terms and is calculated using Eq. (4.5) and (4.6) as presented by Qu and Mudawar [87] where K_{con} is the contraction coefficient, N the number of channels, A_{chan} and A_{plen} the cross-sectional area of the channels and plenum and G the mass flux velocity.

$$\Delta P_{con} = \frac{1}{2\rho_f}\left(G^2 - G_{plen}^2 + K_{con}G^2\right) \quad (4.5)$$

$$\Delta P_{\mathrm{exp}} = \frac{1}{2}\left(\frac{1}{\rho_f} + \frac{x_e}{\rho_{fg}}\right)\left(G_{plen}^2 - G^2 + \left(1 - \frac{NA_{chan}}{A_{plen}}\right)^2 G^2\right) \quad (4.6)$$

The combined channel-plenum contraction and expansion loss is less than 1.4% of the total pressure drop in the copper channels and less than 1% in the silicon channels.

Since the mass quality in the adiabatic two-phase flow in the silicon channels is less than 1% the acceleration/deceleration component (term 7) is negligible. The separated flow form of the accelerative pressure drop in the channel is given by Eq. (4.7) [94], where the void fraction, ε, is determined by the Zivi void fraction correlation, Eq. (4.8) [82]. The two-phase accelerative component is found to be a maximum of 12% of the total pressure drop in the copper control devices and 14% in the copper venting devices.

$$\Delta P_{chan,tp,acc} = \frac{G^2}{\rho_f}\left(\frac{x_e^2}{\varepsilon}\cdot\frac{\rho_f}{\rho_g} + \frac{(1-x_e)^2}{(1-\varepsilon)} - 1\right) \tag{4.7}$$

$$\varepsilon = \left(1 + \frac{(1-x_e)}{x_e}\cdot\left(\frac{\rho_g}{\rho_f}\right)^{2/3}\right)^{-1} \tag{4.8}$$

The experimental and modeled pressure drop for the copper devices presented in this paper represents the sum of term 6, 7, and 8 in Eq. (4.4) with terms 1-3 ignored and terms 4 and 5 calculated out of the experimental data and not included in the model. Terms 1-5 represent a pressure drop of less than 2.4% of the total pressure drop.

4.3.3.3 Temperature, Heat Transfer Coefficient and Thermal Resistance

The type-K thermocouples used in the copper device were calibrated while embedded in the device against the type-T thermocouple (pre-calibrated by AMD Inc.), and an ice bath at 0°C. In-device calibration accounts for any contact thermal resistances and results in an uncertainty of ±0.3°C. Saturation temperature, determined from the measured pressure using a steam table, has an uncertainty of 0.05°C.

The two-phase heat transfer coefficient is calculated using Eq. (4.9):

$$h_{tp} = \frac{q_{sat}}{A_{chan,tp}\cdot\left(T_{d,tp} - T_{sat,m}\right)} \tag{4.9}$$

where q_{sat} is the fraction of the effective input power, q_{in}, that is used for phase change and can be estimated as $q_{sat} = q_{in} - m \cdot C_p \cdot (T_{sat,in} - T_{in})$. $T_{sat,m}$ is the mean of the calculated inlet saturation temperature, $T_{sat,in}$, at P_{in} and the outlet saturation temperature, assuming that saturation temperatures vary linearly along the two-phase region of the channel. The device temperature, $T_{d,tp}$, is calculated from the average of the two downstream center-line thermocouples since the three upstream thermocouples were found to be more strongly influenced by the single phase flow at low exit qualities. The area, $A_{chan,tp}$, is assumed to be the wetted surface area in the microchannels experiencing two-phase flow and does not include the area covered by the capping material.

Using error propagation rules, the uncertainty in the heat transfer coefficient, averaged over all the runs where two-phase flow was produced, is found to be 10%, 12% and 10%, for the control, non-venting membrane and venting membrane devices respectively. The uncertainty is highest at low qualities where the temperature difference between the device and fluid is small. The uncertainties in the temperature measurements and in the absorbed power are the major contributors to the uncertainty in the heat transfer coefficient.

4.3.3.4 Flow Rate and Velocity

Transient flow velocity is determined only in the silicon device by using the pairs of IR slot sensors to measure interface velocities. The maximum velocity that can be measured is 640 mm/s with an uncertainty of 10 mm/s.

The peristalsis pump, which provides liquid to both the silicon and copper heat exchangers, has an uncertainty of 5%. The electronic mass scale has a stated accuracy of 0.002g and is sampled once a second, resulting in a mass flow rate uncertainty of 0.12g/min.

4.3.3.5 Summary of Uncertainties

Table 4.1 summarizes the uncertainties in the raw and calculated values discussed in this study.

Table 4.1 Summary of experimental uncertainties

Quantity	**Device**	**Uncertainty**
[a]Flow velocity	Silicon	10 mm/s
Pressure drop	Silicon	0.9 kPa
Liquid flow rate	Silicon and Copper	5%
[a]Mass flux velocity, *G*	Copper	9%
Pressure drop	Copper	1 kPa (liquid-side) 0.5 kPa (vent-side)
[a]Normalized liquid-side pressure drop	Copper	0.3 (103 kg/s-m^2), 0.1 (208 kg/s-m^2) 0.09 (307 kg/s-m^2), 0.07 (420 kg/s-m^2)
[a]Normalized trans-membrane pressure drop	Copper	0.3
Temperature	Copper	0.3 °C
Venting rate	Copper	0.12 g/min
[a]Heat transfer coefficient	Copper	10-12% (average), 16-47% (max.)
Total input power	Copper	0.1 mW
[a]Heat flux	Copper	5%

[a] calculated values

4.4 Modeling

The diabatic experimental data obtained from the copper heat exchanger is compared against the two-phase vapor venting model. The development of this model is discussed in detail in the preceding Chapter. The pressure drop and heat transfer correlations used in the model was developed from data obtained while running the non-venting control copper device presented here. The model is then used to predict the behavior of the venting device and compared against experimental data to determine when and why the venting device behaves differently and gain an understanding of the physics involved.

4.5 Results and Discussion

4.5.1 Hydraulic Characteristics

4.5.1.1 Steady State Pressure Drop

The reduction in the steady state pressure drop after the onset of boiling in microchannels is one of the key demands for the vapor venting technology as it leads to: 1) smaller pumping power (and thus pump size), 2) reduced fluid saturation and heat exchanger temperature and 3) potentially reduced impact of Ledinegg instability.

Figure 4.8 illustrates both the experimentally measured and simulated normalized pressure drop, $\Delta P_{tot} / \Delta P_{lo}$, against heat flux at the lowest and highest of the four tested mass fluxes in the copper device. The pressure is normalized with the liquid only pressure drop to account for the slight variations in the pressure drop between the different devices due to small differences in the hydraulic diameter (< 10μm). A minimum of two-data sets, taken non-sequentially, is presented to indicate repeatability. Figure 4.8 also include the pressure drop that is measured when using the non-venting membrane device (NVMD), Figure 4.5.C. The improvement in the normalized pressure drop is found to be approximately 60% between the control and venting membrane devices. Using the numerical model described in Chapter 3 we find excellent agreement with the experimental data at the lowest mass flux of 103 kg/s-m^2 but find an increasing under-prediction of the pressure drop improvement during venting as the mass flux increases from 208 kg/s-m^2 to 420 kg/s-m^2. Interestingly we also observe a deviation in the non-venting membrane device from the control data at 420 kg/s-m^2 that is not observed at the lowest tested mass flux. The results suggest that the additional pressure reduction is related to both mass-flux increase and the presence of the membrane.

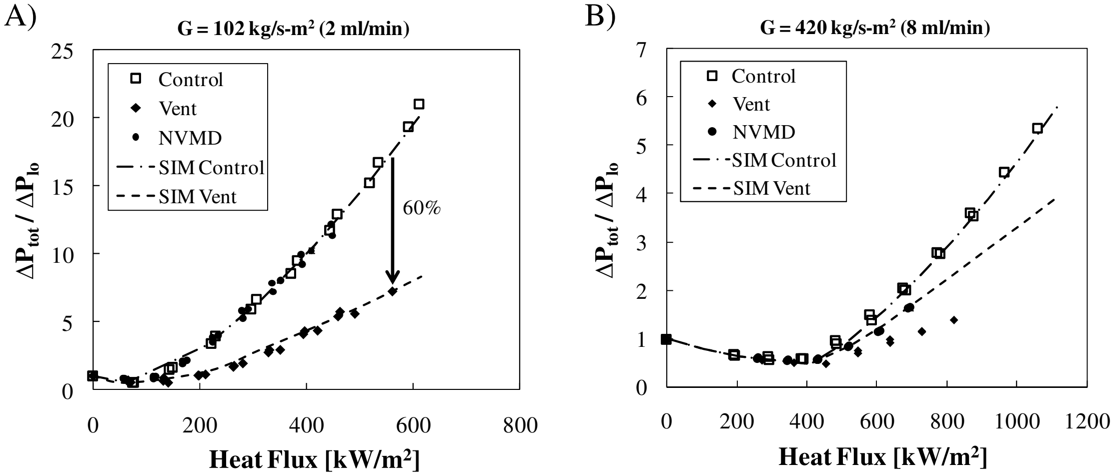

Figure 4.8 Comparison of experimental liquid-only (lo) normalized total pressure drop versus input heat flux for the non-venting control device, non-venting membrane device (NVMD) and venting device shows average improvement ~60% between the control and venting devices. Non-venting membrane devices behave similar to control at mass flux of 102 kg/s-m^2 (A), but deviate at higher mass flux of 420 kg/s-m^2 (B) due to the impact of both hydrophobic membrane and mass flux on the flow regime. Numerical results compare well at 102 kg/s-m^2 but underestimates improvement as mass fluxes increase due to formation of complex churn-annular and droplet type flows.

The primary and most easily understood source of improvement in the pressure drop in the venting devices is the removal of vapor from the two phase flow, resulting in a reduction in mass flux, *G*, as well as quality, *x*, leading to a reduction in both the frictional and accelerative two-phase pressure drops (refer to Eqs. (3.7) to (3.10)). Another important source of pressure drop improvement is the change in flow-regime due to the hydrophobic membrane. The visualization work, discussed in Chapter 2, found that as mass-flux was increased the two-phase flow transitioned from mostly smooth stratified flow at a mass flux of 140 kg/s-m^2 to increasingly more chaotic and churn-annular type flows at a mass flux of 340 kg/s-m^2. Unlike during stratified flow, the churn-annular flow was found to deposit a significant amount of fluid in the form of droplets on the membrane surface that would then be pushed along the membrane surface. The amount of pressure required to push non-wetting droplets on the membrane surface is smaller than that required to move wetting films. Since our model does not capture this complex behavior it under-predicts the pressure drop improvement as mass fluxes increase. This also explains the reduction in pressured drop at the higher mass-flux measured in the non-venting membrane device. Other sources of pressure-drop improvement that were considered but found to be ultimately insignificant include:

i) Membrane deformation: Membrane deformation leads to an increase in the hydraulic diameter of the liquid channel and thus a decrease in the pressure drop. Since the channel length is much longer than the width we can estimate the maximum membrane deflection using the doubly-supported beam bending equation, Eq. (4.10).

$$\Delta y_{\max} = \frac{F' \cdot w^4}{384 \cdot E \cdot I} = \frac{\Delta P_{mem} \cdot L}{32 \cdot E_{mem}} \cdot \left(\frac{w}{t_{mem}} \right)^3 \qquad (4.10)$$

Ko *et al.* determined the Young's Modulus for a 24μm thick, 80% porous PTFE membrane to be 30 MPa [95]. Using this value for E_{mem} in Eq. (4.10), we estimate the maximum membrane deflection to be approximately 50nm and not a significant contributor to the pressure drop improvement. Single-phase runs at the beginning of every experiment also found negligible variation over time, indicating little plastic deformation.

ii) Axial vapor flow: Vapor flow along the length of the membrane could lead to a reduced pressure drop. However estimates of the hydraulic resistance ratio using Eq. (4.11) finds that the resistance for vapor flow along the length of the membrane is five orders of magnitude larger than for vapor flow through the channel itself and thus this mechanism would not be a significant source of pressure improvement.

$$\frac{R_{h,mem}}{R_{h,chan}} = \left(\frac{L}{\kappa} \cdot \frac{\mu_g}{\rho_g} \cdot \frac{1}{w \cdot t_{mem}} \right) \Bigg/ \left(\frac{128}{\pi} \cdot \frac{\mu_g}{\rho_g} \cdot \frac{L}{D_{h,chan}} \right) = \frac{\pi}{128} \cdot \frac{D_h^4}{\kappa \cdot w \cdot t_{mem}} \approx 2 \times 10^5 \qquad (4.11)$$

iii) Vapor slip at the channel-membrane interface: Kaviany presents the slip length, δ, in the membrane, at the channel-membrane interface by Eq. (4.12) [96] where μ and μ' is the standard fluid viscosity and modified viscosity for flow in the membrane respectively, d the channel diameter and κ the membrane intrinsic permeability. If we assume (μ'/μ) to be 1, this slip length is 0.65μm (approximately 3 pore diameters), and thus slip is not expected to significantly contribute to the pressure drop improvement either.

$$\delta = \kappa^{0.5} \cdot \left(\frac{\mu'}{\mu}\right)^{0.5} \cdot \ln\left[\frac{50 \cdot \left(\frac{d^2}{\kappa} - 2\right)}{1 + \left(\frac{d}{\kappa^{0.5}}\right) \cdot \left(\frac{\mu'}{\mu}\right)^{0.5}}\right] \approx 650 \times 10^{-9}\,\mathrm{m} \tag{4.12}$$

4.5.1.2 Impact of trans-membrane pressure on pressure drop improvement

We also investigated the impact of varying the trans-membrane pressure on the pressure drop improvement in the venting devices. The vent side pressure was reduced by increasing the mass suspended on the syringe plunger as shown in the setup in Figure 4.7. The results are summarized in Figure 4.9 with the normalized pressure drop compared to the normalized trans-membrane pressure with the non-venting limit included for comparison. The normalized pressure drop reduces almost linearly as the trans-membrane pressure is increased and the results and trend are well characterized by the model. In the self-venting case, the vent side outlets were left open to the atmosphere such that vapor venting is solely driven by liquid-side pressure with no additional assistance. This is practically important since the application of vacuum on the vent side may not always be feasible. For best hydraulic performance however a high vacuum on the vent side is necessary.

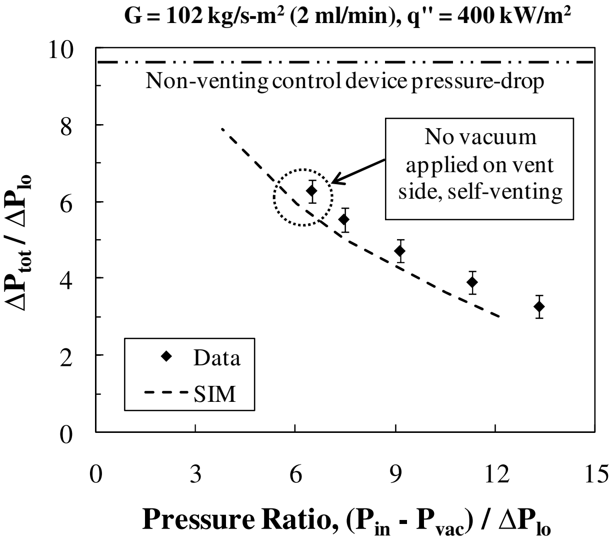

Figure 4.9 Simulation and data for the normalized pressure drop as the pressure ratio is increased. Increasing the trans-membrane pressure by reducing the vacuum pressure results in increased venting and improved device pressure drop. When no vacuum is applied, the vapor self-vents due to the pressure in the liquid-side channel, and the improvement in the pressure drop is ~30%.

A calculation of pumping power efficiency, q_{in} / q_{pump}, as the trans-membrane pressure is increased finds that the efficiency is always better than the non-venting control device due to the improvement in the pressure drop, though this improvement is not monotonic as shown in Figure 4.10. There is initially an increase in the efficiency when the normalized trans-membrane pressure is increased from 6 to 9, as the reduction in the pump power on the liquid side is greater than the increasing work done on the venting side of the device. However, beyond this point, the efficiency begins to reduce as the work done on the vent side increases compared to the reduction in work by the liquid side pump. Thus the improvement in hydraulic (and thermal) performance needs to be weighed against overall efficiency when considering the amount of trans-membrane pressure to apply using a vacuum pump.

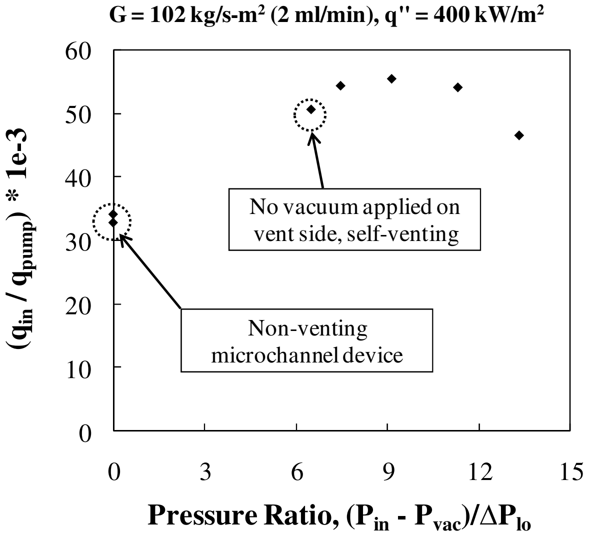

Figure 4.10 Experimental data of the power efficiency vs. the normalized trans-membrane ratio. Increasing the trans-membrane pressure by reducing the vacuum pressure, increases venting and results in smaller liquid side pressures. This reduces the required pumping power on the liquid side. As the vacuum level is increased beyond a certain extent however, the energy savings on the liquid side is offset by the pump power required on the vent side to maintain the given vacuum level resulting in a reduction in the efficiency.

4.5.1.3. Single channel and Static Ledinegg instability

Fang *et al.* [97] carried out 3D FLUENT simulations on vapor venting in a single microchannel and found that despite a reduction in the overall pressure amplitude, high frequency pressure fluctuations due to bubble nucleation and growth existed in both non-venting and venting microchannels. These pressure fluctuations have been experimentally observed by Hetstroni *et al.* [72] in triangular parallel silicon channels. Additionally, Fang *et al.* also found large pressure variations of several thousand Pascals at a lower frequency of 1 kHz in the venting channel due to venting of the vapor bubbles. Due to the use of a low-noise DAQ system with a cutoff frequency of 2Hz, variations in the pressure could not be experimentally measured in the diabatic experiments carried out in the copper channels. However, adiabatic venting of air slugs in the silicon channels, which occur at a much lower frequency, display large changes in pressure and flow-rate in time during the venting process. Pressure dips and flow acceleration for an air injection rate of 0.6 ml/min is shown in

Figure 4.11. As a bubble downstream reaches and then vents through the membrane the hydraulic resistance of the system suddenly drops, akin to an electrical short circuit, resulting in a sudden increase in the flow-rate and a decrease in the pressure drop. These periodic pressure dips were detected at all tested flow-rates but accurately correlating them with the velocity is complicated by the pump feedback system that attempts to maintain constant flow. Under most low air-injection rates tested, pressure change and flow acceleration were found to be negatively correlated in the range of –0.6 to –0.8. Instantaneous velocity data at the highest air-injection rate of 2ml/min were not considered due to the large size of the air-slugs resulting in fewer interfaces to make velocity measurements off of.

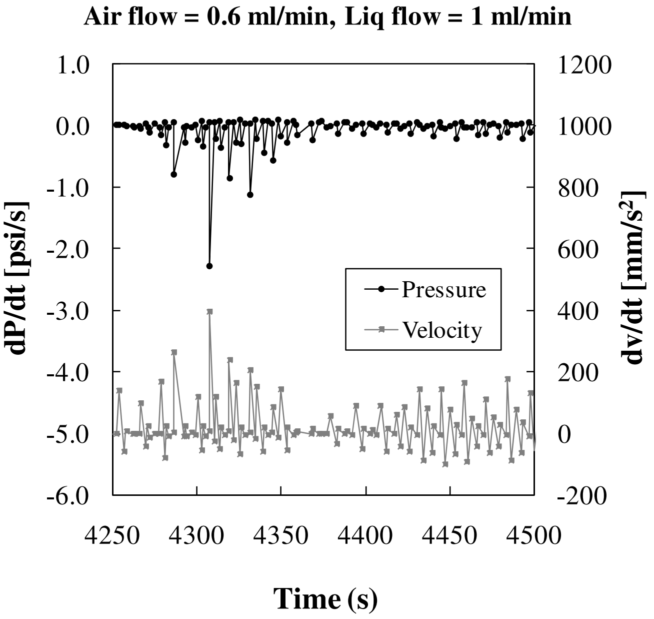

Figure 4.11 Pressure and velocity changes during adiabatic air venting in the silicon venting microchannel device. As an air slug encounters the venting membrane, it begins to vent, causing the system pressure to drop and the flow to accelerate. For this particular experiment the correlation was found to be –0.7. This type of instability is not expected to be significant in two-phase diabatic microchannel devices operating at typical flow-rates and heat fluxes where stratified flows are expected to be dominant.

Though the simulation and experimental evidence suggest additional high amplitude pressure fluctuation can exist during periodic bubble or slug venting, the existence of these flow regimes is typically only observed in larger channels or at low heat fluxes in microchannels with annular, wispy and churn type flows being more common in microchannel flow boiling [73]. Flow visualization in the single microchannel, carried out and discussed in detail in Chapter 2, found that at mass-fluxes and flow qualities similar to those used in the two-phase copper microchannel study presented here, stratified and churning flows are the dominant flow regimes. Vapor venting thus occurs from larger stable gas structures and the large pressure variations observed in the simulations and the adiabatic silicon channel study are not expected to be significant.

More critically, the improvement in pressure drop is expected to reduce the occurrence of static Ledinegg instability that can have highly detrimental effects on the operation of two-phase heat exchangers by starving hotter channels experiencing boiling flows of coolant. Tong and Tang provide background [32] and Zhang *et al.* [31] experimental and numerical treatment of Ledinegg instability during two-phase flow in microchannels. Ledinegg instability occurs when the magnitude of the negative slope in the two-phase demand curve is greater than that of the supply curve for the pump, shown algebraically in Eq. (4.13), causing the system to become unstable.

$$\left(\frac{\partial(\Delta P)}{\partial G}\right)_{channel} \leq \left(\frac{\partial(\Delta P)}{\partial G}\right)_{pump} \quad \text{(criterion for unstable case)} \qquad (4.13)$$

Tong and Tang and Zhang *et al.* suggest the use of inlet constrictors to increase the pressure and reduce the negative slope of the demand curve such that Ledinegg instability is not possible. However, this increases the pressure drop of the system significantly. In our current work the occurrence of Ledinegg instability is reduced due to the smaller change in pressure that occurs on boiling, resulting in a smaller negative slope in the two-phase demand curve. Additionally, unlike the use of constrictors, the overall pressure drop of the system is also lowered. The impact of vapor venting is highlighted in Figure 4.12, which shows the simulated demand curves of the non-venting control and vapor venting devices along with an example supply curve. The simulation results suggest that vapor venting could potentially be very useful in mitigating this instability mechanism.

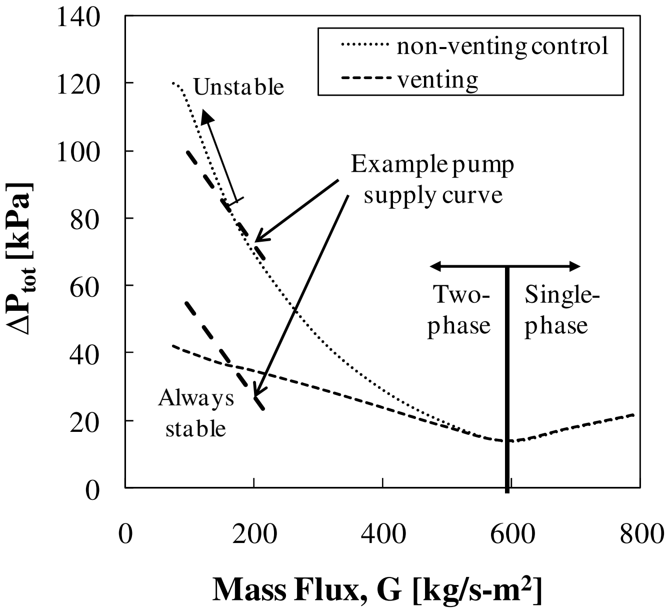

Figure 4.12 Simulated demand curves of pressure drop vs. mass flux for the non-venting and vapor venting devices discussed in this study and based on the model discussed in Chapter 3. Comparison with an example pump supply curve shows that the negative slope -δ(ΔP)/δG for the non-venting devices is greater than that for the pump resulting in static Ledinegg instability. However, the negative slope is smaller for the venting devices making it more stable.

4.5.2 Thermal Characteristics

4.5.2.1 Temperature

With the reduction in pressure drop, the saturation temperature in the copper venting device also drops, resulting in an improvement in the copper device temperatures. Figure 4.13 shows the mean device temperatures as a function of the input power for the lowest and highest tested mass fluxes. Figure 4.13.A also includes temperature data from the non-venting membrane device. The device temperature is improved in all the venting cases with improvements as high as 4.4°C at a mass flux of 208 kg/s-m^2 and heat flux of 730 kW/m^2. This improvement is primarily due to an improvement in the saturation temperatures as seen comparing the average saturation temperature in the control and venting devices. Figure 4.13.A also indicates that the non-venting membrane device suffers from poorer thermal performance with device temperatures larger than the difference in the saturation temperatures between the non-venting membrane device and the control device. The saturation temperature in the non-venting membrane device is higher due to a slightly smaller channel hydraulic diameter leading to larger absolute inlet pressure and saturation temperature and also due to poorer heat transfer coefficients as discussed in the next section.

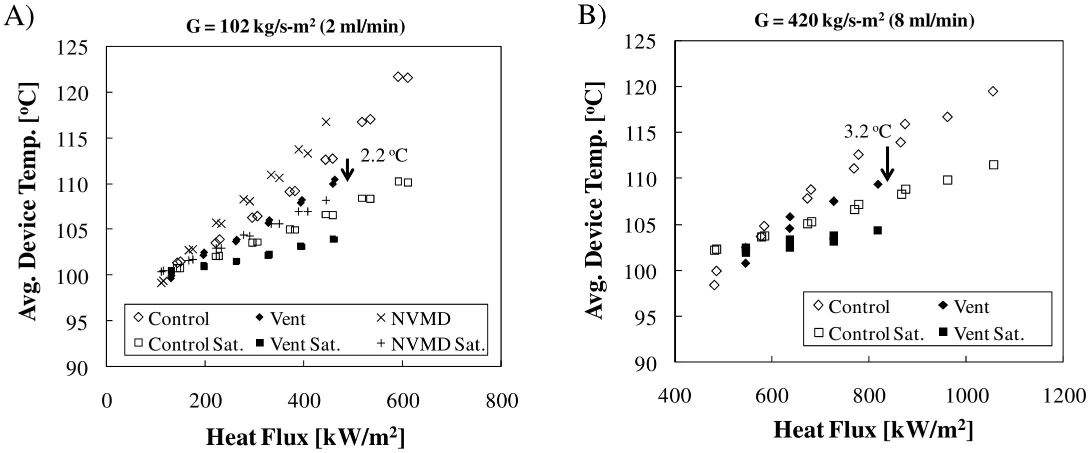

Figure 4.13 Average device temperatures in the control, non-venting membrane (NVMD) and venting devices at two of the four mass fluxes tested. Improvements in device temperatures in the venting devices are found to be mostly due to the improvement in saturation temperatures. Non-venting membrane devices had higher device temperatures than the control due to slightly higher saturation temperature and poorer heat transfer coefficient.

Figure 4.14 shows the improvement in the temperature in the venting device run at 102 kg/s-m^2 and heat flux of 400 kW/m^2 as the trans-membrane pressure is increased by application of vacuum leading to a reduction in the pressure-drop and saturation temperature.

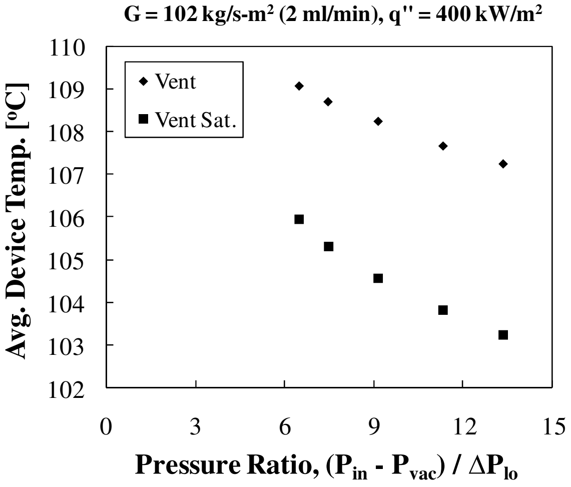

Figure 4.14 Device temperatures improve almost linearly with increasing trans-membrane pressures as saturation temperature reduces.

4.5.2.2 Heat Transfer Coefficient

Figure 4.15 show the measured and simulated heat transfer coefficient at all four mass fluxes tested. The experimental data at the three higher mass fluxes found that the heat transfer coefficient in the venting devices is comparable or higher than the control for a given input power with significant variability in the venting data. The venting data occasionally matches the predicted venting heat transfer coefficients as seen in Figure 4.15.B and C and the difference between control and venting predictions are similar to the predicted difference. The picture presented by the data obtained at 420 kg/s-m^2 is less clear with greater variability also existing in the control data. In the case of the lowest mass flux of 102 kg/s-m^2, the two-phase heat transfer coefficient in the venting device and non-venting membrane devices are found to be consistently lower than the control device and that predicted by the simulation. Varying the trans-membrane pressure at a mass flux of 102 kg/s-m^2 and heat flux of 400 kW/m^2 had negligible impact on the two-phase heat transfer coefficient which was found to be approximately 42 ± 3 kW/m^2-K.

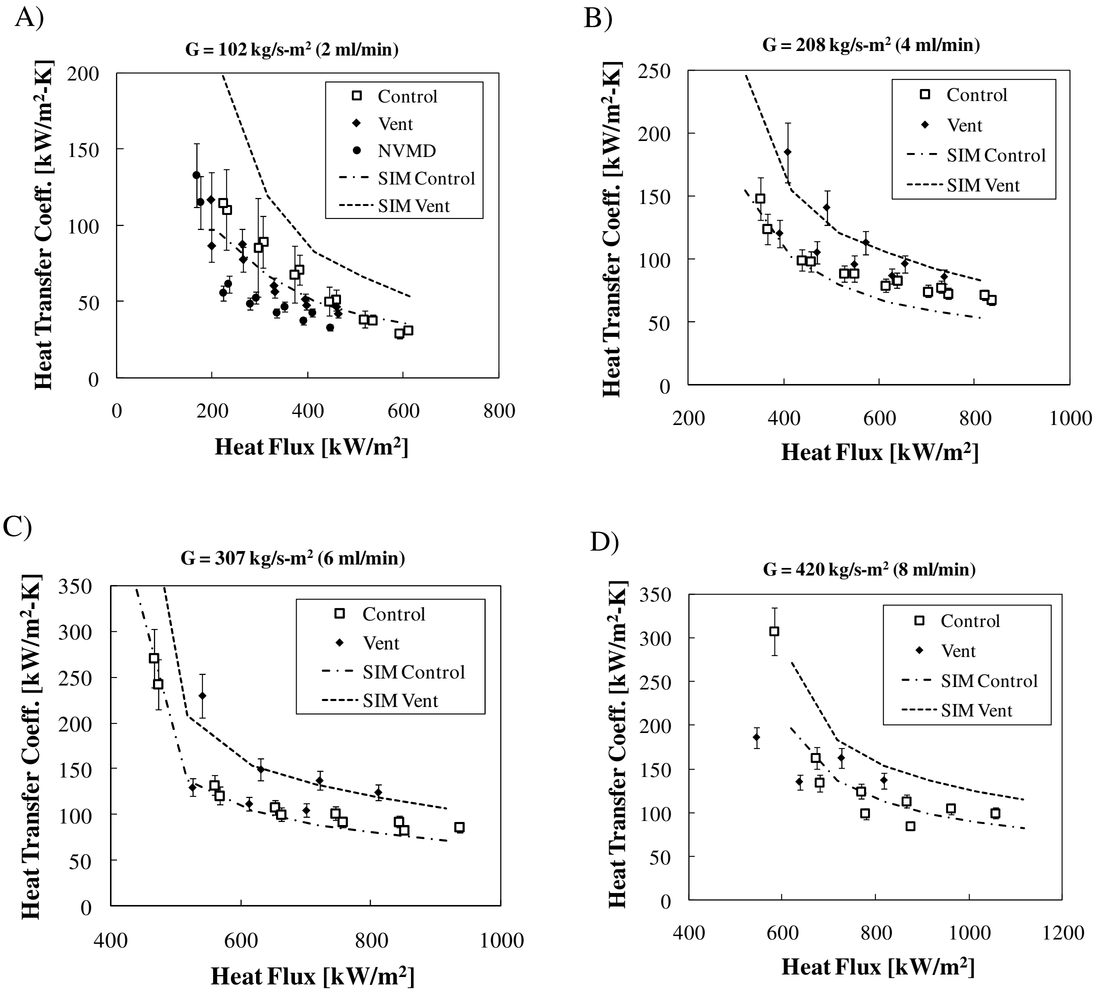

Figure 4.15 Two-phase heat transfer coefficients in the control, non-venting membrane and venting devices at the four tested mass fluxes. The heat transfer coefficients in the venting device are found to be equivalent or slightly higher for the three higher mass fluxes but lower for the lowest mass flux. This is believed to be due to changes in flow regime between the control and venting devices. Improvements in the heat transfer coefficient in the venting device due to lower quality flows is also potentially being offset by the negative impact of reducing saturation pressures.

Due to vapor removal in the venting devices, the quality, mass flux and saturation pressure all reduce. These factors and the change in flow regimes in the venting devices can potentially impact the heat transfer coefficient. The heat transfer coefficient correlation developed in this work, and used in the model, and three of the leading models in the literature given by Kandlikar and Balasubramanian [89], Lee and Mudawar [90] and Thome *et al.* [71] all predict higher heat transfer coefficients at lower vapor quality. Experimentally, we only occasionally find this enhancement in the venting devices at the mass fluxes of 208 and 307 kg/s-m^2 and not at all at the lowest mass flux, even when the trans-membrane pressure, and thus vapor removal rate, increased. These results can be explained by considering the impact of saturation pressure and flow regime changes on the heat transfer coefficient. The model developed by Thome *et al.* [71] and confirmed with experimental data by Dupont *et al.* [98], suggests that the heat transfer coefficient should decrease with reducing saturation pressures. They explain this to be due to reduced frequency in the liquid-annular-vapor cycle. Thus the improvement in the heat transfer coefficient due to reducing quality is potentially being negatively offset by this pressure effect. More significant we believe is the change in flow regime that occurs when a hydrophobic membrane replaces one of the channel walls. As discussed in Chapter 2, stratified flow is observed at low mass flux and churn-annular flow at higher mass flux, with liquid-annular-vapor cyclical flow found to be dominant during visual observations of two-phase flow in the control device used in this work. Stratified flow is thermally less beneficial as compared to annular flow due to the replacement of four thin evaporating films with one thicker film. This explains the poorer heat transfer coefficients in the venting and non-venting membrane devices at the lowest tested mass flux. As mass flux increases churn-annular flow replaces stratified flow in the venting device and this flow regime is expected to have thermal characteristics similar to the annular flow experienced in the control device, thus explaining the similarity in the measured heat transfer coefficients.

The complexity of heat transfer during two-phase flow makes it difficult to predict the expected heat transfer in a vapor venting device using the simple correlation presented here or others available in the literature. However, the picture presented by the experimental data is encouraging with the two-phase heat transfer coefficient in the venting devices either equivalent or slightly higher than the control devices except at the lowest mass flux. The current study and the separate visualization work indicate that churn-annular type flow regimes, dominant at higher mass fluxes in the venting devices, is preferable to maintain and even exceed the high heat transfer coefficients obtained in traditional non-venting microchannel heat exchangers.

4.5.2.3 Thermal Resistance

Figure 4.16 shows the thermal resistance for the control, venting and non-venting membrane copper devices at 102 kg/s-m^2 and 420 kg/s-m^2 mass fluxes. Due to the small changes in temperature between the three different types of devices and the high input power, the thermal resistance for the three different types of devices is not appreciably different. The two-phase segment of the data can be approximated by Eq. (4.14) where the average saturation temperature of 110 °C is used. Better agreement can be obtained by using the exact temperature difference. The single-phase thermal resistance is well approximated by Eq. (4.15).

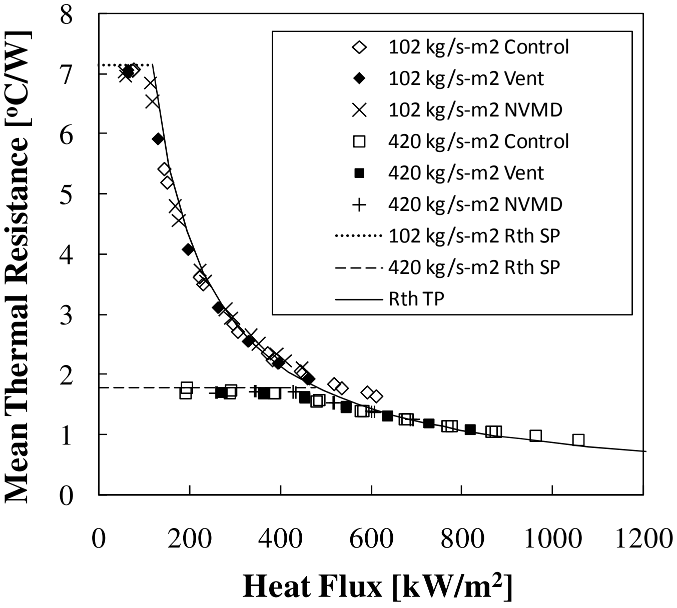

Figure 4.16 Thermal resistance of the three different types of heat exchangers at flow-rates of 2ml/min and 8ml/min. Given the high input powers, there is little difference in the thermal resistance between the devices. The two-phase and single phase regions are well described by Eqs. (4.14) and (4.15) respectively.

The thermal resistances presented here are quite high for an actual heat exchanger and larger than the desired value of 0.1 °C/W or lower. However, increasing the flowrate, reducing saturation temperature, and operating at high qualities can improve the thermal resistance beyond that presented in this work.

$$R_{th,tp} = \frac{T_{sat,avg} - T_{in}}{q_{heat}} \tag{4.14}$$

$$R_{th,sp} = \frac{1}{\dot{m} \cdot C_p} \tag{4.15}$$

4.5.3 Adiabatic and Diabatic Venting Characteristics

4.5.3.1 Adiabatic Venting of Air from Silicon Device

To measure the air-venting rate in the silicon device we injected air into a liquid stream upstream of the device such that a mixture of air and liquid slugs enter the device. The air slugs then vent through the membrane resulting in less air exiting the device. As described in

Table 4.2, almost all the air vents through the membrane for the various flow conditions tested. Precise measurement of inlet air mass at air flow-rates of 2 ml/min is challenging using the setup described by Figure 4.6. When an air slug vents in the device, the flow resistance in the fluidic circuit drops, causing a sudden acceleration in the flow. This non-constant velocity between interface velocity measurements results in a much larger uncertainty in the inlet air mass. Downstream measurements are accurate as the flow is unaffected by the upstream venting and flow rate is approximately constant. Using visual estimates of the average size of an air slug when pumped at 2 ml/min, we conservatively estimate the air mass venting efficiency in these cases to 95%. Venting isn’t perfect at the higher air flow-rate of 2 ml/min because the higher flow velocity during venting results in insufficient time for the larger air slug to completely vent.

Table 4.2 Adiabatic air venting efficiency from an air-water mixture flowing in the silicon microchannel device

Air Flow Rate (ml/min)	Liquid Flow Rate (ml/min)	Venting Eff. %
0.4	0.5	100
1.0	1.0	100
2.0	2.0	> 95
2.0	1.0	> 95
2.0	0.5	> 95
0.8	1.0	100
0.6	1.0	100
2.0	0.7	> 95

4.5.3.2 Diabatic Venting of Vapor from Copper Device

Vapor venting during phase change was measured using the copper device. Figure 4.17 summarizes the experimental and simulated venting rates against the heat flux showing that as the heat flux is increased the venting rate increases due to the larger amount of vapor generated and the increasing pressure on the liquid side. We find good agreement between the experiment and simulation for all the mass fluxes though the predicted change in venting rate with heat flux is lower than measured for the highest mass flux of 420 kg/s-m^2.

The venting rate and venting fraction (vapor vented / vapor generated) as a function of trans-membrane pressure is shown in Figure 4.18. We find that both the venting rate and fraction increase almost linearly with the trans-membrane pressure and use this data to determine the intrinsic permeability of the membrane, κ = 8e-15 m^2, which is an input for the numerical model.

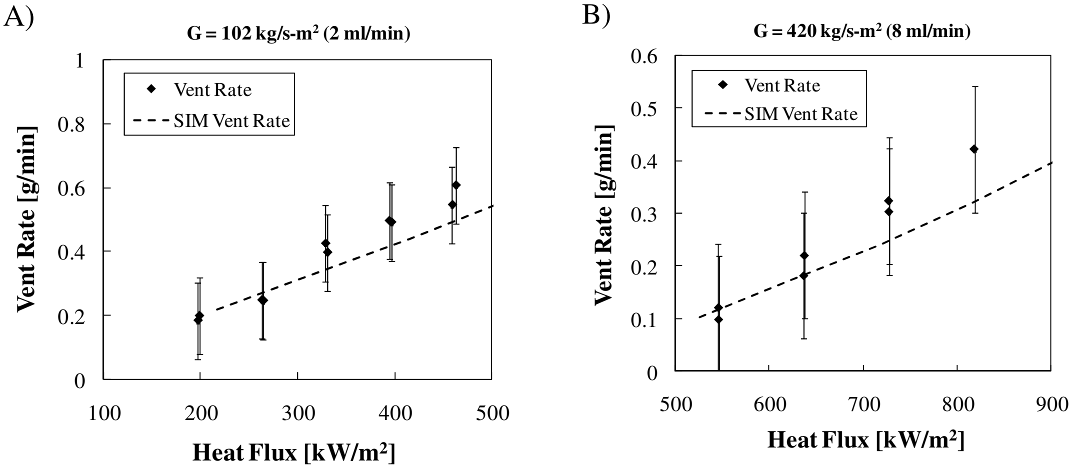

Figure 4.17 Experimental and numerical results of venting rates at two of the four tested mass fluxes. Venting rates increase as more vapor is being generated and because of the rising pressure on the liquid side of the device.

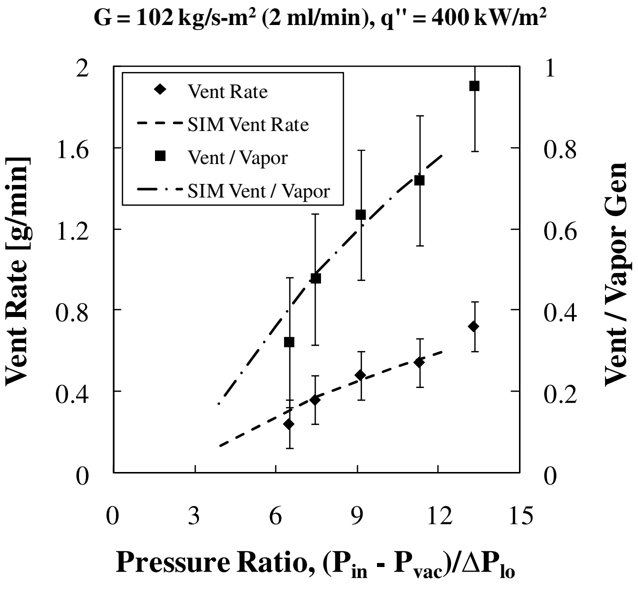

Figure 4.18 Venting rates and venting fractions increase as the trans-membrane pressure increases. The increased vapor removal leads to improved pressure drops and device temperatures.

As briefly mentioned in Chapter 3, to better understand the factors that influence the venting fraction such that it can be maximized to improve the pressure drop and device temperatures, we can compare the hydraulic resistance (or conductance) of the channel with those in the membrane and vent channel. For simplicity we model the two-phase hydraulic resistance in the liquid channel using the homogenous description of two-phase flow. The ratio of the resistances is shown in Eq. (4.16), where B_1 and B_2 are property constants and B_x is a quality dependent property constant that increases with quality and is maximized when flow in the liquid-side channel is vapor only. The third term in the denominator captures the effect of unequal outlet pressures on the liquid and vent side of the device.

$$\frac{R_{h,chan}}{R_{h,mem}+R_{h,vent}+R_{h,press}}=\frac{\left(B_x\cdot\frac{L_{chan}}{D_{h,chan}^4}\right)}{\left(B_1\cdot\frac{t_{mem}}{\kappa}\cdot\frac{1}{w\cdot L_{chan}}\right)+\left(B_2\cdot\frac{L_{vent}}{D_{h,vent}^4}\right)+\left(\frac{P_{out,vent}-P_{out,chan}}{\dot{m}}\right)} \tag{4.16}$$

To improve the venting fraction this resistance ratio must be maximized, and from the relation given, can be achieved through:

i) Thin, highly permeable membranes.

ii) Long, small hydraulic diameter liquid-side channels. This is also thermally beneficial as reducing the hydraulic diameter improves the heat transfer coefficient.

iii) Low aspect ratio liquid channels, where width >> depth, to maximize the venting area. However this also leads to a loss in heat transfer area.

iv) Short, large hydraulic diameter, vent channels.

v) Increasing the static trans-membrane pressure through addition of an outlet choke or vent side vacuum, the latter's effect is shown experimentally in Figure 4.9 and Figure 4.14. However, the trans-membrane pressure is limited by the leakage pressure limit for the given membrane.

4.5.4 Condensation and Membrane Wear/Fouling

Two practical issues that need to be considered in the use of vapor venting membranes in two-phase heat exchangers is vapor condensation within the membrane and membrane wear and fouling over time.

4.5.4.1 Condensation

Condensation occurs when the temperature of the membrane drops below the local saturation temperature of the vapor. If the rate of condensation in the membrane is higher than the rate of evaporation the membrane becomes saturated with liquid over time and impedes vapor transport. The impact of condensation has been studied numerically by Fang *et al.* [34] and experimentally by David *et al.* [99] and it was found that a small amount of condensation effectively stops vapor from venting.

Condensation occurring on the surface of the PTFE membrane and within the membrane was observed during diabatic operation of the silicon venting device and is shown in Figure 4.19.A-C. The liquid channels are below the opaque membrane surface. The vent side of the device is cooled by room-temp air that is pumped into the vent side to remove the condensed liquid. Dark splotches, shown in Figure 4.19.A, is condensation that is occurring within the membrane on low heating of the fluid underneath. As the power is increased the liquid heats up further and evaporation and condensation increase, leading to droplet formation on the surface of the membrane as shown in Figure 4.19.B. As power is increased further, vaporization of the liquid occurs and the vapor vents through the membrane into the vent channel. The process of venting and the increased temperature of the membrane reduce condensation and leads to large dried-out regions as shown in Figure 4.19.C. In the silicon work, the use of the thin, highly hydrophobic PTFE membrane enables the condensate to be removed easily without the need for additional guard heating.

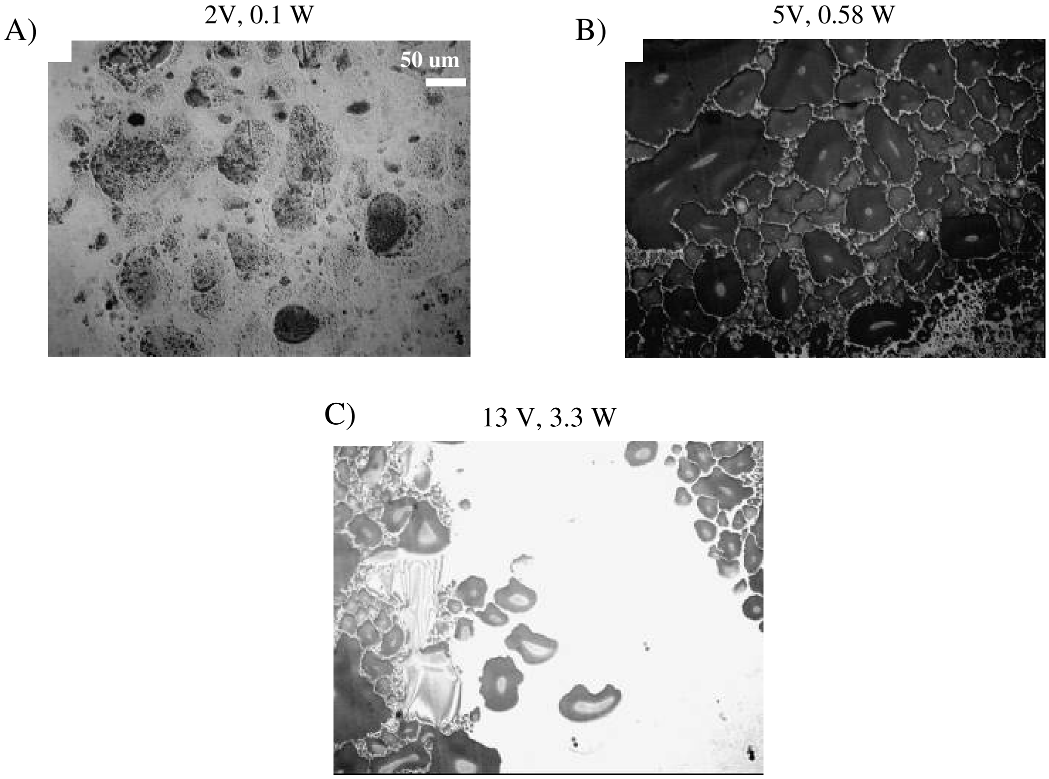

Figure 4.19 View of the top surface of the PTFE membrane during diabatic operation of the silicon heat exchanger shows the impact of condensation and evaporation. A) As the fluid is being heated, some of the liquid evaporates and condenses within and on the surface of the membrane, creating dark 'splotches.' B) As the heating is increased the amount of evaporation and condensation also increases resulting in the formation of large drops on the surface of the membrane. C) Once phase change occurs in the channels below the venting vapor pushes out the condensed fluid and clears the membrane as evidenced by the white open regions. The membrane is also sufficiently hot that further condensation is reduced.

Condensation is also believed to have impacted our previous experimental work into a vapor venting heat exchanger as discussed in detail in Ref. [99]. In that study our first generation copper microchannel device incorporated two membranes, a 65μm thick hydrophobic PTFE membrane and a 170μm thick hydrophilic carbon paper membrane that provided mechanical support in lieu of the vent channels in the work reported here. Venting of vapor occurred through the two membranes directly to the atmosphere. Due to the lack of thermal insulation on the vent side the carbon paper membrane would have been at a lower temperature than the saturation temperature of 100°C for the venting vapor, resulting in condensation within this membrane. This condensation begins during sensible heating of the fluid such that by the time phase-change occurs in the channels the carbon membrane is mostly saturated with fluid and venting is minimal. Pressure drop measurements taken using the first generation venting device found no improvement over the control device.

Condensation did not play a measurable role in the 2nd generation devices, discussed in detail in this Chapter. Surface insulation and a large contact area between the heated substrate and the capping substrate helped maintain a high temperature in the vent channels and membrane during operation. Maintaining the temperature of the membrane over that of the saturation temperature as well as enabling easy removal of condensate from the membrane, are key to maintaining device performance.

4.5.4.1 Membrane Wear and Fouling

Membrane wear and fouling over time is an important issue to consider as the membrane properties could be changed to a degree that render the heat exchanger ineffective. Changes in the hydrophobicity [100], porosity, pore diameter or pore structure can change the permeability and leakage prevention of the membrane as well as flow-regime and heat transfer characteristics. Membrane fouling by particulates would result in eventual pore blockage and the loss of venting ability. As a preliminary study of this issue we carried out SEM imaging of the membranes before and after approximately 30 hours of cyclical operation. Figure 4.20.A shows an unused PTFE membrane and Figure 4.20.B and Figure 4.20.C shows the membrane removed from the device used in this study, where Figure 4.20.B was imaged in the venting region and Figure 4.20.C in the non-venting region sandwiched between the mating copper walls. The brighter regions in the images are artifacts due to charging of the non-electrically conductive membrane by the electron beam. From observation it appears that the membrane has not appreciably changed after 30 hours of operation. Thermal cycling however has had significant impact in the non-venting part of the membrane, with pores appearing to have closed and an overall reduction in porosity. Due to this microscopic change, the membrane in these regions has turned translucent and lost its normal opacity. No fouling was observed in any region of the membrane.

The preliminary SEM study shows that the membrane deforms only when in intimate contact with the heated substrates but remains visibly unchanged and clean in the venting regions. Repeatability in venting and pressure drop data between runs confirm that wear and fouling is not significant in our work though much longer term studies of device performance are required.

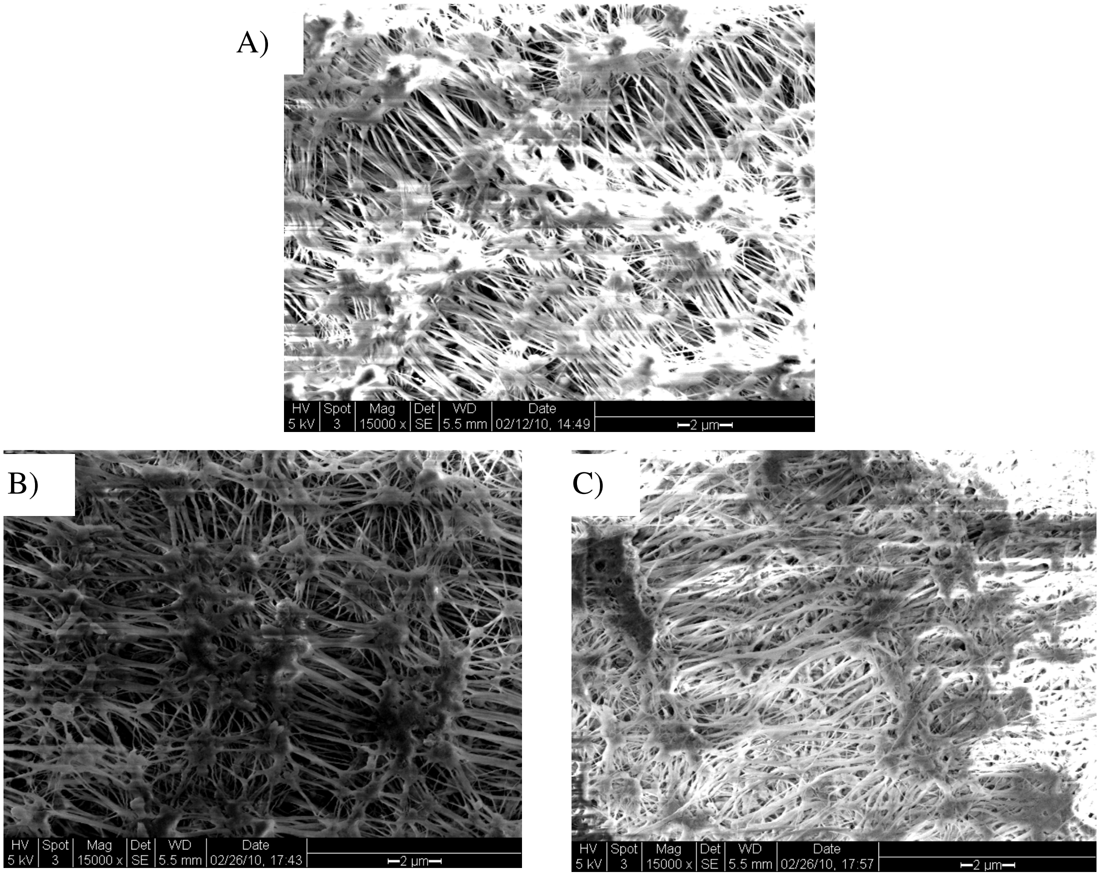
A)
HV Spot Mag Det WD Date
5 kV 3 15000 x SE 5.5 mm 02/12/10, 14:49
2 µm
B)
HV Spot Mag Det WD Date
5 kV 3 15000 x SE 5.5 mm 02/26/10, 17:43
2 µm
C)
HV Spot Mag Det WD Date
5 kV 3 15000 x SE 5.5 mm 02/26/10, 17:57
2 µm

Figure 4.20 SEM of the 220nm PTFE membrane before and after 30+ hours of cyclical use in the copper vapor venting device. A) SEM of unused membrane. B) SEM of membrane from venting region of the copper device after use. Comparison with (A) shows little wear or fouling on the membrane surface. C) SEM of membrane from non-venting region sandwiched between copper substrate and cap show that compression combined with thermal cycling results in a significant loss of porosity. The membrane also turned translucent in this region.

4.6 Summary of Findings and Conclusion

Our experimental and numerical work on the vapor separation and venting from a two-phase flow led to several findings that are summarized below.

i) Silicon and copper heat exchangers were designed and fabricated to carry out a broad set of experiments. We identified a successful silicon fabrication process-flow to build silicon gas venting devices.

ii) Pressure drop in the venting devices were experimentally found to be ~60% lower than for the non-venting control devices with the model showing excellent agreement at the lowest mass flux of 102 kg/s-m^2. Additional pressure drop improvement, believed to be due to changes in the flow regime from stratified to churning-annular, was found as the mass flux was increased to 420 kg/s-m^2. This additional pressure drop is found to be as much as 50% when using the non-venting membrane device at the highest mass flux.

iii) Single-channel pressure instability was studied using adiabatic venting of air from an air-water flow in the silicon device. We measured sharp pressure dips and flow acceleration during venting of the air slugs. The impact of these instabilities is expected to be significant only in bubbly or slug type flow regimes where the vapor vents in discrete quantities.

iv) Reduction in the pressure drop is predicted to mitigate the occurrence of detrimental static Ledinegg instabilities. Simulation of demand curves of non-venting and venting devices find that the negative slope, $-\delta(\Delta P)/\delta G$, for the venting devices is reduced and could potentially be lowered below that of the supply curve.

v) Temperatures in the copper venting devices were improved by an amount equivalent to the reduction in the saturation temperature and as much as 4.4°C at 208 kg/s-m^2 mass flux and 730 kW/m^2 total input heat flux. Temperatures in the non-venting membrane devices were found to be worse than in the non-venting control.

vi) Two-phase heat transfer coefficients in the venting devices were found to be approximately the same or higher as that in the control devices for mass fluxes of 208, 307 and 420 kg/s-m^2 but lower at a mass flux of 102 kg/s-m^2. Though reduction in quality is expected to improve heat transfer rates during venting, reduction in saturation pressure and changes in flow regime could negatively impact it. Churn-annular type flows at higher mass fluxes is preferred due to similar thermal characteristics as typical annular flows.

vii) Condensation can reduce and eliminate vapor venting by saturating the membrane with liquid. Condensation was observed in the silicon devices during diabatic experiments, and condensation within carbon paper membranes installed in the first generation copper devices resulted in no improvement in pressure drop during operation. Condensation can be reduced by heating the membrane, reducing saturation temperatures using vacuum on the vent side of the membrane, and by using thin, highly permeable membranes that don’t trap condensed liquid.

viii) Changes in membrane structure and properties over time can result in changes in the way the device operates by altering the leakage pressure, permeability and flow regime. Membrane wear and fouling by particulates was studied by comparing SEMs of the membrane before and after 30 hours of cyclical use. Little change in the structure or fouling was observed in the venting portions of the membrane.

The work in this chapter shows that an operating vapor venting heat exchanger does exhibit improved hydraulic and thermal characteristics under thermal loads typical of a mid-range microprocessor. The work presented here also shows the usefulness of the results from the visualization work, carried out in Chapter 2, in generating potential explanations for the divergence between the vapor venting model and experiment. The results also highlight the need for greater understanding of flow regimes and transition criteria to better predict the vapor venting heat exchanger pressure drop and heat transfer coefficient.

It is encouraging that as we move to higher mass fluxes, and encounter churn type flows, the venting device performs hydraulically better than expected and the heat transfer coefficient approaches the values predicted by the model. Though churning-annular flows may potentially reduce the vapor removal rate by wetting the membrane and blocking pores the advantage gained in reduced pressure drop and higher heat transfer coefficients make it a desirable operating flow regime for vapor venting heat exchangers. Further design work, as suggested by the experiments and simulation results, is necessary to optimize the heat exchanger and obtain the best performance.

CHAPTER 5 | CONCLUSION

5.1 Summary of Results and Contributions to the Field

This dissertation documents the approaches that were used to study phase separation in a two-phase microchannel heat exchanger. At the time this work was started no previous work on the use of vapor removal during phase change to improve two-phase heat exchanger performance was found in the literature. The closest analogue was membrane distillation at the macroscale, with most microscale phase separation work focused on adiabatic degassing from chemical and biological microfluidic devices and gas removal from micro fuel-cells. The state of the field represented a unique opportunity to study and characterize the vapor separation process at the microscale and determine its potential for two-phase heat exchangers.

The overall study of phase separation consists of three major approaches that were carried out concurrently: i) fundamental visualization study of air and vapor separating flow phenomena, ii) development of a vapor separating two-phase flow model and subsequent numerical study of a vapor venting heat exchanger and, iii) fabrication and experimental characterization of air and vapor separating silicon and copper microchannel devices, the latter of which was used to cool an AMD thermal test chip.

The first approach discussed in this dissertation is a fundamental study of the flow phenomena in a single 110μm diameter copper microchannel during air and vapor separation through a 220nm pore, 65μm thick, porous hydrophobic PTFE membrane. A high speed visualization study was initially carried out by injecting air into a water flow and then recording the two-phase flow structures that form in the microchannel as the injected air escapes through the membrane. The flow structures observed were then summarized in a flow regime map. Multiple types of structures develop with stratified flows on the hydrophobic surface found to be dominant at $We < 0.2 \sim 0.6$ and annular flows at higher *We* numbers. Through image analysis and reported air and liquid pressure drops and flow rates, air removal was found to be improved by increasing surface area, increasing trans-membrane pressure and reducing the *We* number. Higher *We* number flows leads to the formation of annular flows that impede air removal due to the formation of thin liquid films that flow on the membrane surface. Though adiabatic air-water flows can be studied in a more precise and controlled manner it was critical to also consider the flow phenomena during vaporization, relevant for heat exchanger operation. Visualization found that stratified flows are once again dominant at low mass fluxes but annular and churning annular flows dominant at higher mass fluxes. However, unlike adiabatic two-phase flows, diabatic flows show cyclical wet/two-phase/dry behavior reminiscent of previously reported studies of phase change in microchannels. Additionally, high *We* number flows are desirable due to the potential for improved pressure drop and heat transfer due to droplet flow on the hydrophobic membrane surface and formation of comparatively thinner evaporating films respectively. The high speed visualization of phase separation at high velocities, pressures and air/vapor qualities, development of adiabatic and diabatic flow regime maps, and analysis of factors impacting phase separation are a first in the field and assist in the design of gas and vapor venting devices operating under more aggressive conditions than have been documented in previous work.

Concurrent to the study of adiabatic and diabatic phase separating flow phenomena, both numerical and experimental work was carried out to predict and characterize the performance of a multichannel phase separating heat exchanger. A conjugate heat transfer two-phase flow model with local vapor removal was developed using momentum and heat transfer correlations developed from experimental data of two-phase flow in a non-venting microchannel device. The model was then used to study the impact of various factors on vapor venting heat exchanger performance. Factors considered include substrate material and thickness, membrane permeability and thickness, channel density, liquid and vent channel diameter and vent-to-liquid channel diameter ratio. Under all simulated conditions it was found that a vapor venting heat exchanger performs better than a heat exchanger that has the same channel hydraulic diameter as the channel on the liquid side of the venting heat exchanger. However, the venting device performs better than a volumetrically equivalent heat exchanger only under limited conditions. Reducing membrane thickness and increasing permeability is the most effective method of improving venting device performance, with more realistic membranes requiring smaller liquid side channels. A 50µm diameter liquid and vent channel device with a 65µm thick, 1.1µm pore diameter membrane is predicted to offer hydraulic and thermal performance equivalent or better than that provided by a volumetrically equivalent heat exchanger. This work contributes to the field by being the first numerical model developed for vapor separating two-phase flows. The application of this model enabled a study of the various factors impacting venting heat exchanger performance and identified its advantages and shortcomings, findings not previously reported in the literature.

Experimental results are necessary to verify and cement the analytical predictions of venting heat exchanger performance enhancements as compared to a standard two-phase heat exchanger. This led to the third major study which considered the design, fabrication and experimental characterization of silicon and copper multichannel devices. A new silicon process flow for the fabrication of a vapor separation device was developed that enables researchers in the field to design and build vapor or gas venting silicon devices. A copper vapor venting device with nineteen 19mm long, 132µm square channels and a 65µm thick, 220nm pore PTFE membrane was also fabricated and tested at a variety of mass fluxes ranging from 102 to 420 kg/s-m^2 and heat fluxes up to a maximum of 840 kW/m^2. The tested heat fluxes are typical for CPUs and were generated by an AMD thermal test chip. Results showed significant improvements in pressure drop (max. ~60%) and pumping power and a reduction in heat exchanger temperatures (max. 4.4^{o}C) when using the vapor separating heat exchanger. The experiment was found to agree with vapor removal predictions from the two-phase venting model. Pressure drops were found to agree well at the lowest mass flux but under-predicted the improvement as mass fluxes increased. The model also over-predicted heat transfer coefficients at lower mass fluxes. These results were explained using observations from the flow phenomena study with thermally poorer stratified flows dominant at low mass fluxes and thermally and hydraulically beneficial churning-annular flows at higher mass fluxes. This work is the first of its kind to experimentally characterize the hydraulic, thermal and venting performance of a vapor venting heat exchanger operating under a real world thermal load and highlights the importance of the knowledge of two-phase flow structures in predicting the pressure drop and heat transfer coefficients.

The next section highlights some of the key challenges and limitations in the presented work and directions for future work.

5.2 Challenges and Directions for Future Work

Flow phenomenon visualization work provides critical information needed for the proper understanding of the factors that affect gas/vapor removal and the role of flow regimes in pressure drop and heat transfer in a microchannel. One of the key limitations in this work was the inability to accurately measure liquid film thicknesses and film temperatures, the combination of which would have enhanced our understanding of the local two phase heat transfer coefficient and helped verify the hypothesis that churning annular flows offer higher heat transfer coefficients than stratified flows. One possible approach to capture film temperature, together with void fraction, is the use of two-dye fluorescence thermometry. The high speeds required to capture the boiling and venting behavior, combined with the typically small fluorescing liquid volume during two-phase flow make fluorescence techniques challenging using cameras but viable using photon multipliers or high gain photodiodes [101,102]. Photodiode or PMT based techniques provide temperature and void fraction information for the probed region but offer no structure information thus requiring that film thickness measurements be made using a high sensitivity camera, though this method is only reasonable for fairly steady flows. Another interesting aspect to study is the impact of contact angle on the flow structures formed. In this work we only considered the contact angle when determining the leakage pressure but do not consider the impact of varying degrees of hydrophobicity on the types of flow structures formed, which impact vapor removal, pressure drop and the heat transfer coefficient. To study the impact of different contact angles on gas and vapor removal, different membranes or membranes with different hydrophobic coatings could be tested using the described visualization device. This topic has not been previously explored in the literature, and the results would be valuable to the gas/vapor venting device designer. A final aspect for future research involves the development of a new visualization platform. A silicon/glass visualization device with an in-situ membrane allows for a much cleaner and elegant structure to study vapor separation at the expense of the experimental flexibility afforded by the current device. The in-situ porous region, as shown in Figure 5.1, could be fabricated by forming porous silicon regions or by selectively growing nanowire/nanotube forests. Carbon nanotube (CNT) and ZnO nanostructures possess superhydrophobicity with contact angles in excess of 140° [103-106], though CNT nanostructures require additional surface treatment for stable superhydrophobicity [104].

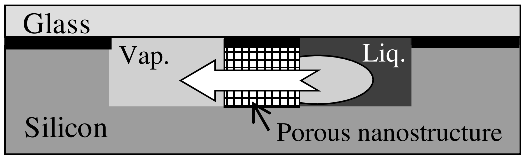

Figure 5.1 Schematic of a silicon device with an in-situ porous structure (center) that vents the vapor formed in the liquid channel on the right to the vent channel on the left.

The modeling work has significant potential for future development. The model presented in this dissertation is based on bulk correlations, which though useful, does not capture the flow regime specific behavior. This limitation was captured in Chapter 4, where the model overestimated the two-phase pressure drop as the flow became increasingly chaotic and annular in nature and over estimated the heat transfer coefficient at low mass fluxes where stratified flow is dominant. Physics based momentum and heat transfer models need to be developed to more accurately capture device performance. This in turn requires further studies on phase separating flow regimes and regime transitions. It is also beneficial to relax certain assumptions of the flow in the membrane. Two key assumptions currently in place are 1D transverse flow in the membrane and adiabatic single phase vapor flow in the membrane. Though 1D flow is a reasonable assumption when using thin single membranes, it is less valid when using thick membranes, membrane stacks or when using membranes with anisotropic permeability such as carbon paper. Incorporating this modification helps determine the best combination of membranes for phase separation and vapor transport. Previous experimental work suggested that condensation within the membrane could result in loss of venting [99], which highlights the importance of incorporating non-adiabatic two-phase flow in the membrane in the current model. Though modeling of two-phase flow and heat conduction in a porous material is complex, several methods such as Percolation and Lattice-Boltzmann now exist in the literature and could potentially be incorporated in the current model [68,107-110].

The silicon multichannel devices were fabricated with a variety of different geometries. However, the fragility of the silicon devices resulted in poor yield, particularly after the contact print process. Complex channel shapes, superior channel depth control through dry etching techniques and smaller feature sizes than what is capable by traditional machining make silicon based phase separation devices a key requirement for future work in a variety of directions. Silicon devices feature less spreading and possess a smaller thermal mass as compared to copper devices which makes them ideal to explore the high-frequency cyclical flow instabilities as well as static Ledinegg instabilities. The presented work only features simulated predictions of instability mitigation and further work is necessary to quantify the stability improvement and silicon devices are key for this study. As such, a better process flow needs to be developed to reliably fabricate the required instrumented silicon devices. Instrumented silicon venting devices thus enable a more detailed study of the impact of cross-sectional geometry and non-uniform heating on the venting, hydraulic, thermal and stability improvements. Another limitation in the multichannel device studies is the inability to visualize the phase separation process and the dominant flow regimes, due to the opacity of the membrane. This could be solved by using transparent hydrophobic membranes such as polypropylene or surface treated porous polycarbonate. However, both these membranes possess poorer thermal properties and must be used with caution in the venting heat exchanger device. Further studies using the current platform include testing the performance of the devices using different membranes. Apart from the two membranes mentioned, treated porous glass, treated porous alumina and hydrophobic porous nylon are all viable membrane materials for use in a venting heat exchanger, with each possessing specific advantages and disadvantages.

From an industrial application standpoint it is also necessary to repeat the current study for dielectric fluids and refrigerants, which are more commonly used in electronics cooling applications. However, this study will also require the evaluation of alternate porous membranes as the currently studied PTFE membrane may no longer be appropriate for use. It is also critical to carry out a careful review of all the available materials and coatings for use as separation surfaces as both modeling and experiments have shown that the performance improvements of the venting heat exchanger are closely related to the membrane properties.

5.3 Concluding Remarks

The work presented in this dissertation is hoped to provide a rounded view on the fundamental and practical aspects of a vapor separating microfluidic heat exchanger. Using single- and multi- microchannel devices, different aspects of air and vapor separation from a two-phase flow was studied. Flow phenomena in a single channel phase separating device was observed, categorized and summarized in new flow regime maps while the multichannel vapor separating heat exchanger was used to quantify the pressure drop and device temperature improvements under realistic CPU heat fluxes. The experimental and modeling results show improvements in the pressure drop and device temperature over a standard two-phase heat exchanger. With currently available materials, simulations also highlight the venting heat exchanger's shortcomings compared to a volumetrically equivalent heat exchanger. However, superior performance is predicted if high conductance membranes were used together with smaller microchannels. The work highlights the myriad of exciting opportunities that exist for further research work in device and flow characterization, device fabrication, membrane material development and characterization and two-phase flow modeling. This work emphasizes the potential of fabricating a two-phase microfluidic vapor separating heat exchanger that solves many of the issues inherent to traditional two-phase heat exchangers, and in doing so enables the implementation of two-phase microfluidic heat exchangers for effective and efficient cooling of high power electronic and computing systems.

REFERENCES

[1] International Technology Roadmap for Semiconductors 2007, (2007).

[2] J. Koo, S. Im, L. Jiang, K.E. Goodson, Integrated Microchannel Cooling for Three-Dimensional Electronic Circuit Architectures, J. Heat Transfer. 127 (2005) 49-58.

[3] K. Bernstein, R. Puri, A. Young, P. Andry, J. Cann, P. Emma, et al., Interconnects in the third dimension, in: Proceedings of the 44th Annual Conference on Design Automation - DAC '07, San Diego, California, 2007: p. 562.

[4] R. Schmidt, M.K. Iyengar, Thermodynamics of Information Technology Data Centers, IBM J. Res. & Dev. 53 (2009) 9:1-15.

[5] S. Kandlikar, M. Shoji, V.K. Dhir, Handbook of phase change : boiling and condensation, Taylor & Francis, Philadelphia PA, 1999.

[6] R.E. Simons, M.J. Ellsworth, R.C. Chu, An Assessment of Module Cooling Enhancement With Thermoelectric Coolers, J. Heat Transfer. 127 (2005) 76.

[7] G. Chen, A. Shakouri, Heat Transfer in Nanostructures for Solid-State Energy Conversion, J. Heat Transfer. 124 (2002) 242.

[8] J. Cancheevaram, R. Alley, E. Siivola, R. Venkatasubramanian, Performance of Integrated Thin-film Thermoelectrics in cooling “hot-spots” on Microprocessors – Experimental setup and Results, MRS Proceedings. 793 (2003) S8.18.

[9] P. Phelan, V. Chiriac, T. Lee, Current and future miniature refrigeration cooling technologies for high power microelectronics, IEEE Trans. Comp. Packag. Technol. 25 (2002) 356-365.

[10] S. Trutassanawin, E. Groll, S. Garimella, L. Cremaschi, Experimental Investigation of a Miniature-Scale Refrigeration System for Electronics Cooling, IEEE Trans. Comp. Packag. Technol. 29 (2006) 678-687.

[11] A. Heydari, Miniature vapor compression refrigeration systems for active cooling of high performance computers, in: ITherm 2002. Eighth Intersociety Conference on Thermal and Thermomechanical Phenomena in Electronic

Systems (Cat. No.02CH37258), San Diego, CA, USA, n.d.: pp. 371-378.

[12] T. Brunschwiler, H. Rothuizen, M. Fabbri, U. Kloter, B. Michel, R.J. Bezama, et al., Direct liquid jet impingement cooling with micron sized nozzle array and distributed return architecture, in: The Tenth Intersociety Conference on Thermal and Thermomechanical Phenomena in Electronics Systems, San Diego, California, USA, 2006: pp. 196-203.

[13] D. Kercher, Jeong-Bong Lee, O. Brand, M. Allen, A. Glezer, Microjet cooling devices for thermal management of electronics, IEEE Trans. Comp. Packag. Technol. 26 (2003) 359-366.

[14] E. Wang, L. Zhang, L. Jiang, J. Koo, J. Maveety, E. Sanchez, et al., Micromachined Jets for Liquid Impingement Cooling of VLSI Chips, J. Microelectromech. Syst. 13 (2004) 833-842.

[15] M.K. Sung, I. Mudawar, Single-Phase and Two-Phase Hybrid Cooling Schemes for High-Heat-Flux Thermal Management of Defense Electronics, J. Electron. Packag. 131 (2009) 021013.

[16] D. Tuckerman, R. Pease, High-performance heat sinking for VLSI, IEEE Electron Device Lett. 2 (1981) 126-129.

[17] M. Ellsworth, L. Campbell, R. Simons, M. Iyengar, R. Schmidt, R. Chu, The evolution of water cooling for IBM large server systems: Back to the future, in: 2008 11th Intersociety Conference on Thermal and Thermomechanical Phenomena in Electronic Systems, Orlando, FL, USA, 2008: pp. 266-274.

[18] S. Kandlikar, W. Grande, Evaluation of Single Phase Flow in Microchannels for High Heat Flux Chip Cooling - Thermohydraulic Performance Enhancement and Fabrication Technology, Heat Transfer Engineering. 25 (2004) 5-16.

[19] W. Qu, I. Mudawar, Experimental and numerical study of pressure drop and heat transfer in a single-phase micro-channel heat sink, International Journal of Heat and Mass Transfer. 45 (2002) 2549-2565.

[20] S. Garimella, V. Singhal, Single-Phase Flow and Heat Transport and Pumping Considerations in Microchannel Heat Sinks, Heat Transfer Engineering. 25 (2004) 15-25.

[21] W. Qu, I. Mudawar, Flow boiling heat transfer in two-phase micro-channel heat sinks—I. Experimental investigation and assessment of correlation methods, International Journal of Heat and Mass Transfer. 46 (2003) 2755-2771.

[22] L. Jiang, M. Wong, Forced Convection Boiling in a Microchannel Heat Sink, Journal of Microelectromechanical Systems. 10 (2001) 80-88.

[23] G. Hetsroni, A. Mosyak, Z. Segel, G. Ziskind, A uniform temperature heat sink for cooling of electronic devices, International Journal of Heat and Mass Transfer. 45 (2002) 3275-3286.

[24] L. Zhang, E. Wang, K. Goodson, T. Kenny, Phase change phenomena in silicon microchannels, International Journal of Heat and Mass Transfer. 48 (2005) 1572-1582.

[25] V. Carey, Chapter Ten: Introduction to Two-Phase Flow, in: Liquid-Vapor Phase-Change Phenomena : An Introduction to the Thermophysics of Vaporization and Condensation Processes in Heat Transfer Equipment, Hemisphere Pub. Corp., Washington D.C., 1992: pp. 399-452.

[26] L.S. Tong, Y.S. Tang, Boiling heat transfer and two-phase flow, 2nd ed., Taylor & Francis, Washington D.C., 1997.

[27] S. Garimella, J.D. Killion, J.W. Coleman, An Experimentally Validated Model for Two-Phase Pressure Drop in the Intermittent Flow Regime for Circular Microchannels, J. Fluids Eng. 124 (2002) 205.

[28] H. Wu, P. Cheng, Boiling instability in parallel silicon microchannels at different heat flux, International Journal of Heat and Mass Transfer. 47 (2004) 3631-3641.

[29] C. Kuo, Y. Peles, Pressure effects on flow boiling instabilities in parallel microchannels, International Journal of Heat and Mass Transfer. 52 (2009) 271-280.

[30] R.D. Flynn, Flow Boiling Instabilities in Microchannels, (2008).

[31] T. Zhang, T. Tong, J. Chang, Y. Peles, R. Prasher, M.K. Jensen, et al., Ledinegg instability in microchannels, International Journal of Heat and Mass Transfer. 52 (2009) 5661-5674.

[32] L.S. Tong, Y.S. Tang, Chapter 6: Instability of Two-Phase Flow, in: Boiling Heat Transfer and Two-Phase Flow, 2nd ed., Taylor & Francis, Washington D.C., 1997: pp. 457-480.

[33] P. Zhou, K. Goodson, J. Santiago, Vapor Escape Microchannel Heat Exchanger, U.S. Patent 6994151, 2006.

[34] C. Fang, M. David, A. Rogacs, K. Goodson, Volume of Fluid Simulation of Boiling Two-Phase Flow in a Vapor-Venting Microchannel, Frontiers in Heat and Mass Transfer. 1 (2010).

[35] K. Lawson, D. Lloyd, Membrane distillation, Journal of Membrane Science. 124 (1997) 1-25.

[36] M. Elbourawi, Z. Ding, R. Ma, M. Khayet, A framework for better understanding membrane distillation separation process, Journal of Membrane Science. 285 (2006) 4-29.

[37] A. Alklaibi, N. Lior, Membrane-distillation desalination: Status and potential, Desalination. 171 (2005) 111-131.

[38] S. Nagdewe, J.K. Kwoon, H.D. Kim, D.S. Kim, K.M. Kwak, T. Setoguchi, A parametric study for high-efficiency gas-liquid separator design, J. Therm. Sci. 17 (2008) 238-242.

[39] G.P. Willems, J.P. Kroes, M. Golombok, B.P.M. van Esch, H.P. van Kemenade, J.J.H. Brouwers, Performance of a Novel Rotating Gas-Liquid Separator, J. Fluids Eng. 132 (2010) 031301.

[40] G. Baker, W. Clark, B. Azzopardi, J. Wilson, Transient effects in gas–liquid phase separation at a pair of T-junctions, Chemical Engineering Science. 63 (2008) 968-976.

[41] H. Xu, Q. Han, T. Meek, Effects of ultrasonic vibration on degassing of aluminum alloys, Materials Science and Engineering: A. 473 (2008) 96-104.

[42] Z. Yang, S. Matsumoto, R. Maeda, A prototype of ultrasonic micro-degassing device for portable dialysis system, Sensors and Actuators A: Physical. 95 (2002) 274-280.

[43] D. Cheng, H. Jiang, A debubbler for microfluidics utilizing air-liquid interfaces,

Appl. Phys. Lett. 95 (2009) 214103.

[44] E. Kang, D.H. Lee, C. Kim, S.J. Yoo, S. Lee, A hemispherical microfluidic channel for the trapping and passive dissipation of microbubbles, J. Micromech. Microeng. 20 (2010) 045009.

[45] J. Kohnle, G. Waibel, R. Cernosa, M. Storz, H. Ernst, H. Sandmaier, et al., A unique solution for preventing clogging of flow channels by gas bubbles, in: Technical Digest. MEMS 2002 IEEE International Conference. Fifteenth IEEE International Conference on Micro Electro Mechanical Systems (Cat. No.02CH37266), Las Vegas, NV, USA, pp. 77-80.

[46] A.M. Skelley, J. Voldman, An active bubble trap and debubbler for microfluidic systems, Lab Chip. 8 (2008) 1733.

[47] J.H. Kang, Y.C. Kim, J. Park, Analysis of pressure-driven air bubble elimination in a microfluidic device, Lab Chip. 8 (2008) 176.

[48] M. Johnson, G. Liddiard, M. Eddings, B. Gale, Bubble inclusion and removal using PDMS membrane-based gas permeation for applications in pumping, valving and mixing in microfluidic devices, J. Micromech. Microeng. 19 (2009) 095011.

[49] X. Zhu, Micro/nanoporous membrane based gas–water separation in microchannel, Microsyst Technol. 15 (2009) 1459-1465.

[50] J.H. Sung, M.L. Shuler, Prevention of air bubble formation in a microfluidic perfusion cell culture system using a microscale bubble trap, Biomed Microdevices. 11 (2009) 731-738.

[51] C. Chen, Y. Su, An autonomous CO2 discharge and electrolyte agitation scheme for portable microbial fuel cells, J. Micromech. Microeng. 17 (2007) S265-S273.

[52] D.D. Meng, J. Kim, C. Kim, A degassing plate with hydrophobic bubble capture and distributed venting for microfluidic devices, J. Micromech. Microeng. 16 (2006) 419-424.

[53] D.D. Meng, T. Cubaud, C. Ho, C. Kim, A Methanol-Tolerant Gas-Venting Microchannel for a Microdirect Methanol Fuel Cell, J. Microelectromech. Syst.

16 (2007) 1403-1410.

[54] Y. Chuang, C. Chieng, C. Pan, S. Luo, F. Tseng, A spontaneous and passive waste-management device (PWMD) for a micro direct methanol fuel cell, J. Micromech. Microeng. 17 (2007) 915-922.

[55] D.D. Meng, C. Kim, An active micro-direct methanol fuel cell with self-circulation of fuel and built-in removal of CO_2 bubbles, Journal of Power Sources. 194 (2009) 445-450.

[56] N. Paust, C. Litterst, T. Metz, R. Zengerle, P. Koltay, Fully passive degassing and fuel supply in direct methanol fuel cells, in: 2008 IEEE 21st International Conference on Micro Electro Mechanical Systems, Tucson, AZ, USA, 2008: pp. 34-37.

[57] D.D. Meng, C.J. Kim, Micropumping of liquid by directional growth and selective venting of gas bubbles, Lab Chip. 8 (2008) 958.

[58] C. Litterst, S. Eccarius, C. Hebling, R. Zengerle, P. Koltay, Novel Structure for Passive CO2 Degassing in μDMFC, in: 19th IEEE International Conference on Micro Electro Mechanical Systems, Istanbul, Turkey, n.d.: pp. 102-105.

[59] B. Alexander, E. Wang, Design of a Microbreather for Two-Phase Microchannel Heat Sinks, Nanoscale & Microscale Thermophysical Eng. 13 (2009) 151-164.

[60] M. García-Payo, M.A. Izquierdo-Gil, C. Fernandez-Pineda, Wetting Study of Hydrophobic Membranes via Liquid Entry Pressure Measurements with Aqueous Alcohol Solutions, Journal of Colloid and Interface Science. 230 (2000) 420-431.

[61] Y. Taitel, A.E. Dukler, A model for predicting flow regime transitions in horizontal and near horizontal gas-liquid flow, AIChE J. 22 (1976) 47-55.

[62] L. Cheng, G. Ribatski, J.R. Thome, Two-Phase Flow Patterns and Flow-Pattern Maps: Fundamentals and Applications, Appl. Mech. Rev. 61 (2008) 050802.

[63] P. Chung, M. Kawaji, The effect of channel diameter on adiabatic two-phase flow characteristics in microchannels, International Journal of Multiphase Flow. 30 (2004) 735-761.

[64] T. Cubaud, C. Ho, Transport of bubbles in square microchannels, Phys. Fluids. 16 (2004) 4575.

[65] P. Garstecki, M.J. Fuerstman, H.A. Stone, G.M. Whitesides, Formation of droplets and bubbles in a microfluidic T-junction—scaling and mechanism of break-up, Lab Chip. 6 (2006) 437.

[66] M. De Menech, P. Garstecki, F. Jousse, H.A. Stone, Transition from squeezing to dripping in a microfluidic T-shaped junction, J. Fluid Mech. 595 (2008) 141-161.

[67] A.M. Marconnet, M.P. David, A. Rogacs, R.D. Flynn, K.E. Goodson, Temperature-Dependent Permeability of Microporous Membranes for Vapor Venting Heat Exchangers, in: Volume 10: Heat Transfer, Fluid Flows, and Thermal Systems, Parts A, B, and C - ASME 2008 IMECE, Boston, Massachusetts, USA, 2008: pp. 1005-1012.

[68] U. Pasaogullari, P.P. Mukherjee, C. Wang, K.S. Chen, Anisotropic Heat and Water Transport in a PEFC Cathode Gas Diffusion Layer, J. Electrochem. Soc. 154 (2007) B823.

[69] P.K. Sinha, P.P. Mukherjee, C. Wang, Impact of GDL structure and wettability on water management in polymer electrolyte fuel cells, J. Mater. Chem. 17 (2007) 3089.

[70] S.G. Kandlikar, Heat Transfer Mechanisms During Flow Boiling in Microchannels, J. Heat Transfer. 126 (2004) 8-16.

[71] J. Thome, V. Dupont, A.M. Jacobi, Heat transfer model for evaporation in microchannels. Part I: presentation of the model, International Journal of Heat and Mass Transfer. 47 (2004) 3375-3385.

[72] G. Hetsroni, A. Mosyak, E. Pogrebnyak, Z. Segal, Explosive boiling of water in parallel micro-channels, International Journal of Multiphase Flow. 31 (2005) 371-392.

[73] T. Harirchian, S.V. Garimella, Effects of channel dimension, heat flux, and mass flux on flow boiling regimes in microchannels, International Journal of Multiphase Flow. 35 (2009) 349-362.

[74] T. Harirchian, S.V. Garimella, A comprehensive flow regime map for microchannel flow boiling with quantitative transition criteria, International Journal of Heat and Mass Transfer. 53 (2010) 2694-2702.

[75] R. Revellin, J.R. Thome, A new type of diabatic flow pattern map for boiling heat transfer in microchannels, J. Micromech. Microeng. 17 (2007) 788-796.

[76] V. Carey, Liquid-vapor phase-change phenomena : an introduction to the thermophysics of vaporization and condensation processes in heat transfer equipment, Hemisphere Pub. Corp., Washington D.C., 1992.

[77] F. Brissette, MatLab Steam Tables, Montreal, Canada, 2005.

[78] F.M. White, Chp 3: Solutions oif the Newtonian Viscous Flow Equations, in: Viscous Fluid Flow, 2nd ed., McGraw-Hill, n.d.: pp. 104-217.

[79] M. Kaviany, Principles of heat transfer in porous media, 2nd ed., Springer-Verlag, New York, 1995.

[80] S. Kakac, R.K. Shah, W. Aung, Handbook of single-phase convective heat transfer, Wiley, New York, 1987.

[81] L. Zhang, J. Koo, L. Jiang, M. Asheghi, K.E. Goodson, J.G. Santiago, et al., Measurements and modeling of two-phase flow in microchannels with nearly constant heat flux boundary conditions, J. Microelectromech. Syst. 11 (2002) 12-19.

[82] S.M. Zivi, Estimation of steady-state steam void fraction by means of the principle of minimum entropy production, Journal of Heat Transfer. 86 (1964) 247-252.

[83] H.J. Lee, D.Y. Liu, Y. Alyousef, S. Yao, Generalised Two-Phase Pressure Drop and Heat Transfer Correlations in Evaporative Micro/Minichannels, Journal of Heat Transfer. 132 (2010) 041004-1 - 041004-9.

[84] L. Sun, K. Mishima, Evaluation analysis of prediction methods for two-phase flow pressure drop in mini-channels, International Journal of Multiphase Flow. 35 (2009) 47-54.

[85] P. Lee, S. Garimella, Saturated flow boiling heat transfer and pressure drop in silicon microchannel arrays, International Journal of Heat and Mass Transfer.

51 (2008) 789-806.

[86] K. Mishima, T. Hibiki, Some characteristics of air-water two-phase flow in small diameter vertical tubes, International Journal of Multiphase Flow. 22 (1996) 703-712.

[87] W. Qu, I. Mudawar, Measurement and prediction of pressure drop in two-phase micro-channel heat sinks, International Journal of Heat and Mass Transfer. 46 (2003) 2737-2753.

[88] W. Kays, M.E. Crawford, Convective heat and mass transfer, 3rd ed., McGraw-Hill, New York, 1993.

[89] S. Kandlikar, P. Balasubramanian, An Extension of the Flow Boiling Correlation to Transition, Laminar, and Deep Laminar Flows in Minichannels and Microchannels, Heat Transfer Engineering. 25 (2004) 86-93.

[90] J. Lee, I. Mudawar, Two-phase flow in high-heat-flux micro-channel heat sink for refrigeration cooling applications: Part II - heat transfer characteristics, International Journal of Heat and Mass Transfer. 48 (2005) 941-955.

[91] B. Agostini, R. Revellin, J. Thome, Elongated bubbles in microchannels. Part I: Experimental study and modeling of elongated bubble velocity, International Journal of Multiphase Flow. 34 (2008) 590-601.

[92] M.E. Steinke, S.G. Kandlikar, Flow Boiling and Pressure Drop in Parallel Flow Microchannels, in: 1st International Conference on Microchannels and Minichannels - ICNMM 2003, Rochester, New York, USA, 2003: pp. 567-579.

[93] J.E. Steinbrenner, Two-phase flow regimes in fuel cell microchannels, (2010).

[94] R.W. Lockhart, R.C. Martinelli, Proposed Correlation of Data for Isothermal Two-Phase, Two-component flow in pipes, Chem. Eng. Prog. 45 (1949) 39-48.

[95] W. Ko, C. Tseng, W. Wu, C. Lee, Charge storage and mechanical properties of porous PTFE and composite PTFE/COC electrets, E-Polymers. (2010) 1-10.

[96] M. Kaviany, Chp 2: Fluid Mechanics, in: Principles of Heat Transfer in Porous Media, 2nd ed., Springer-Verlag, New York, 1995: pp. 17-118.

[97] C. Fang, M.P. David, A. Rogacs, K.E. Goodson, Volume of Fluid Simulation of Boiling Two-Phase Flow in a Vapor-Venting Microchannel, Frontiers in Heat

and Mass Transfer 1 (2010) 1.

[98] V. Dupont, J. Thome, A.M. Jacobi, Heat transfer model for evaporation in microchannels. Part II: comparison with the database, International Journal of Heat and Mass Transfer. 47 (2004) 3387-3401.

[99] M.P. David, A.M. Marconnet, K.E. Goodson, Hydrodynamic and thermal performance of a vapor-venting microchannel copper heat exchanger, in: Sixth International ASME Conference on Nanochannels, Microchannels and Minichannels - ICNMM 2008, Darmstadt, Germany, 2008: pp. ICNMM2008-62269.

[100] H.Z. Syed, R. Hackam, Effects of water salinity, electric stress and temperature on the hydrophobicity of polytetrafluoroethane, in: IEEE Conference on Electrical Insulation and Dielectric Phenomena, Atlanta, GA, USA, 1998: pp. 100-103.

[101] M.P. David, D. Fogg, C. Hidrovo, R. Flynn, K. Goodson, Development and Calibration of a Two-Dye Fluorescence System for Use in Two-Phase Micro Flow Thermometry, in: Thermal and Thermomechanical Proceedings 10th Intersociety Conference on Phenomena in Electronics Systems, 2006. ITHERM 2006., San Diego, CA, n.d.: pp. 79-86.

[102] D. Fogg, M. P. David, K. E. Goodson, Non-invasive measurement of void fraction and liquid temperature in microchannel flow boiling, Exp Fluids. 46 (2008) 725-736.

[103] L. Feng, Z. Yang, J. Zhai, Y. Song, B. Liu, Y. Ma, et al., Superhydrophobicity of Nanostructured Carbon Films in a Wide Range of pH Values, Angew. Chem. Int. Ed. 42 (2003) 4217-4220.

[104] K.K.S. Lau, J. Bico, K.B.K. Teo, M. Chhowalla, G.A.J. Amaratunga, W.I. Milne, et al., Superhydrophobic Carbon Nanotube Forests, Nano Lett. 3 (2003) 1701-1705.

[105] Y.H. Yang, Z.Y. Li, B. Wang, C.X. Wang, D.H. Chen, G.W. Yang, Self-assembled ZnO agave-like nanowires and anomalous superhydrophobicity, J. Phys.: Condens. Matter. 17 (2005) 5441-5446.

[106] X. Feng, L. Feng, M. Jin, J. Zhai, L. Jiang, D. Zhu, Reversible Super-hydrophobicity to Super-hydrophilicity Transition of Aligned ZnO Nanorod Films, J. Am. Chem. Soc. 126 (2004) 62-63.

[107] J. Nam, M. Kaviany, Effective diffusivity and water-saturation distribution in single- and two-layer PEMFC diffusion medium, International Journal of Heat and Mass Transfer. 46 (2003) 4595-4611.

[108] D.G. Avraam, A.C. Payatakes, Flow regimes and relative permeabilities during steady-state two-phase flow in porous media, J. Fluid Mech. 293 (2006) 207.

[109] C. Pan, M. Hilpert, C.T. Miller, Lattice-Boltzmann simulation of two-phase flow in porous media, Water Resour. Res. 40 (2004).

[110] R. Larson, L. Scriven, H. Davis, Percolation theory of two phase flow in porous media, Chemical Engineering Science. 36 (1981) 57-73.